Nonlinear Frequency Conversion in Lithium Niobate Nanophotonic Circuits for Quantum Spectroscopy

Thesis by
Emily Yoonju Hwang

In Partial Fulfillment of the Requirements for the
Degree of
Doctor of Philosophy

CALIFORNIA INSTITUTE OF TECHNOLOGY
Pasadena, California

2025
Defended June 3, 2025

Emily Yoonju Hwang
ORCID: 0000-0002-9541-5887

ACKNOWLEDGEMENTS

First, this thesis would not have been possible without my advisor, Professor Scott Cushing. Scott, thank you for your mentorship, constant encouragement, and endless positivity throughout the years. I am truly grateful to you for trusting me with this project and for always believing in me.

To the members of my thesis committee, Professors Joe Falson, Alireza Marandi, and Kerry Vahala, thank you for your invaluable guidance and feedback.

I am grateful for the past and present members of the Cushing group. To the entangled photon subgroup — Nathan Harper, Dr. Manni He, Dr. Bryce Hickam, Dr. Szilard Szoke, Ayantika Sengupta, and Ric Tolentino — thank you for the discussions and camaraderie. I'd like to especially thank Nathan Harper, who co-developed the work in this thesis, and Ayantika Sengupta, who will be taking over the project. I'd also like to give a shout out to Nathan Harper, Wonseok Lee, and Levi Palmer, who joined the lab with me during the pandemic.

I sincerely thank the Marandi group, especially Dr. Ryoto Sekine, Dr. Luis Ledezma, Ben Gutierrez, and Juanis Valles. To Ryoto and Luis, thank you for training me and for your endless patience and understanding. I would like to thank Ryoto in particular, whose mentorship and work ethic has been truly invaluable and inspiring.

The work in this thesis would not have been possible without the staff members of the KNI and the Beckman Biological Imaging Facility. To the staff of the KNI: Dr. Guy DeRose, Bert Mendoza, Alex Wertheim, Kelly McKenzie, Alireza Ghaffari, and Nathan Lee, thank you for your tireless efforts in maintaining the cleanroom. I'd also like to thank the staff of the BIF, Dr. Andres Collazo, Dr. Giada Spigolon, and Dr. Ying Wang, for their helpful support and feedback when it comes to microscopy.

I also thank the administrators and staff of the APhMS and CCE departments, especially Elisha Okawa and Joe Drew for ensuring that the Cushing group and Noyes, respectively, run smoothly every day.

To my past mentors at Harvey Mudd College, thank you for launching my scientific career. I would like to thank the chemistry department for inspiring my love of science and for their thorough instruction and support. To Professor Lori Bassman, thank you for starting my research journey and for shaping me into the scientist I am today. I never would have become a Caltech PhD student without your advice and guidance.

Thank you to Dr. Farzaneh Afshinmanesh and everyone at PINC Technologies for the invaluable opportunity to do an internship during my PhD. I'm excited to work together moving forward.

I am truly grateful for the friends I met through Caltech: Dr. Thomas Tran, Jocelyn Dao, Sahil Patel, Ami Sheth, Lily Shiau, and Kevin Yu. Your friendship has kept me sane during this PhD, and I appreciate all of our unhinged chats.

Last but not least, I would like to thank my family. To my parents, thank you for all the sacrifices you have made for me. Without your endless love and support, I could have never gotten this far. I hope I have made you proud, and I will forever be grateful to be your daughter.

ABSTRACT

Quantum light sources are becoming an increasingly popular alternative to pulsed lasers for spectroscopy, microscopy, and sensing. The inherent quantum correlations of entangled photons present unique advantages in spectroscopy, enabling high signal-to-noise ratios, low excitation fluxes, and time-resolved measurements without requiring a pulsed laser. Entangled photon sources for spectroscopic measurements typically consist of bulk crystals or ion-diffused waveguides. Integrated platforms such as thin-film lithium niobate have potential for highly efficient, tailored, and compact entangled photon sources through periodically poled nanophotonic waveguides. The advantageous nonlinear optical properties of lithium niobate coupled with the nanophotonic thin film platform allows for frequency conversion, quantum state generation, state manipulation, and sample interaction all on a single compact chip, demonstrating thin-film lithium niobate's potential for compact and portable integrated spectrometers.

Here, we present our work in frequency conversion and sample interactions in thin-film lithium niobate. Most of the previous demonstrations of nanophotonic lithium niobate waveguides have focused on infrared wavelengths for applications in quantum communication and computing, leaving the shorter wavelengths that are of interest for spectroscopy still a largely unexplored space. In this work, frequency conversion in thin-film lithium niobate is investigated from ultraviolet through telecom wavelengths. Periodically poled lithium niobate nanophotonic waveguides are fabricated for second harmonic generation in the ultraviolet-A region and entangled photon generation at visible and near-infrared wavelengths. Using a violet continuous wave laser, a waveguide with a fluorescent dye-doped polymer cladding layer is investigated for sample interactions. Finally, preliminary work in entangled photon triplet generation down to telecom wavelengths is explored. This work represents a step towards compact, on-chip spectrometers and sensors through lithium niobate photonic integrated circuits.

PUBLISHED CONTENT AND CONTRIBUTIONS

[1] N. A. Harper*, E. Y. Hwang*, P. A. Kocheril, T. K. Lam, S. K. Cushing, *Optics Express* **2024**, *32*, 27931,
E.Y.H. participated in the conception of the project, designed and fabricated the device, participated in device characterization and data analysis, and wrote a significant portion of the manuscript.
* denotes equal contributions.

[2] N. A. Harper*, E. Y. Hwang*, R. Sekine, L. Ledezma, C. Perez, A. Marandi, S. K. Cushing, *Optica Quantum* **2024**, *2*, 103,
E.Y.H. participated in the conception of the project, designed and fabricated the device, participated in device characterization and data analysis, and wrote a significant portion of the manuscript.
* denotes equal contributions.

[3] E. Hwang*, N. Harper*, R. Sekine, L. Ledezma, A. Marandi, S. Cushing, *Optics Letters* **2023**, *48*, 3917,
E.H. participated in the conception of the project, designed and fabricated the device, participated in device characterization and data analysis, and lead the writing of the manuscript.
* denotes equal contributions.

TABLE OF CONTENTS

LIST OF ILLUSTRATIONS

LIST OF TABLES

NOMENCLATURE

BPM. Birefringent phase matching.

C153. Coumarin-153.

CSPDC. Cascaded spontaneous parametric downconversion.

CW. Continuous wave.

FDE. Finite difference eigenmode.

GVD. Group velocity dispersion.

GVM. Group velocity mismatch.

IR. Infrared.

LN. Lithium niobate, $LiNbO_3$.

LNOI. Lithium-niobate-on-insulator.

LT. Lithium tantalate, $LiTaO_3$.

MZI. Mach-Zehnder interferometer.

PIC. Photonic integrated circuit.

PMMA. Poly(methyl methacrylate).

QPM. Quasi-phase matching.

SFG. Sum frequency generation.

SHG. Second harmonic generation.

SOI. Silicon-on-insulator.

SPAD. Single photon avalanche detector.

SPDC. Spontaneous parametric downconversion.

TE. Transverse electric.

TFLN. Thin-film lithium niobate.

TM. Transverse magnetic.

UV. Ultraviolet.

Chapter 1

INTRODUCTION

Spectroscopy and microscopy are powerful tools to investigate the properties of atoms, molecules, and materials. Nonlinear spectroscopy and multiphoton microscopy in particular are capable of high spatial resolution, deep tissue imaging, ultrafast dynamics, and excitation of transitions that are inaccessible in linear analogs [1–4]. However, these techniques are often limited to academic laboratory settings due to the large size, cost, and maintenance of the high power ultrafast pulsed lasers required for measurements.

Entangled photons (Figure 1.1) have been an important resource in quantum optical applications for decades and are a promising alternative to pulsed lasers in spectroscopy, microscopy, and sensing. Entanglement can be generated through spontaneous parametric downconversion (SPDC) in various degrees of freedom, including energy-time, polarization, and path entanglement [6]. In the SPDC process, a pump photon can spontaneously split into two lower energy entangled photons as the pump propagates through a nonlinear optical crystal. The inherent quantum correlations between the entangled photon pair are of great interest for applications

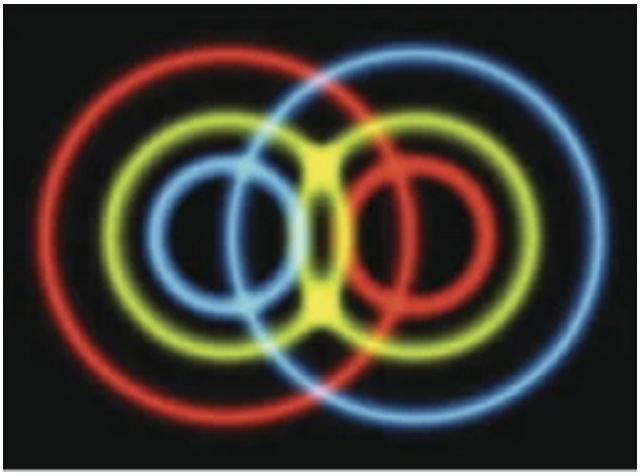

Figure 1.1: Photograph of entangled photons generated from a bulk nonlinear crystal. Three false-color images are superposed. Due to nature of the energy and momentum matching, each frequency is emitted in an emission cone. Reproduced from Ref. [5] with permission from Springer Nature.

such as quantum cryptography [7], communication [8], and computation [9]. In spectroscopy and microscopy, these correlations have been demonstrated to enable high signal-to-noise ratios [10–13], decreased diffraction limits [14], low excitation fluxes for sensitive biological samples [15], linearization of nonlinear optical processes [16], and time-resolved measurements without a pulsed laser [17]. In particular, the linearization and time-resolved measurements using entangled photons are of interest for both new and established techniques in single-molecule sensing and biological imaging.

The single photon-like behavior of the photon pairs, imparted by the entangled photon generation process, enables the linearization of classically nonlinear processes such as harmonic generation [19], sum frequency generation [20], and two photon absorption [21]. In particular, the linear behavior of entangled two photon absorption (ETPA) [22–24] has potential applications in sensing and spectroscopy in the low-flux regime, where the linear response of entangled photons enhances the two photon absorption rate compared to the quadratic scaling of classical light (Figure 1.2) [16, 25]. Despite the theoretical enhancements using entangled photons, ETPA has been difficult to experimentally observe due to difficulties in eliminating single photon processes that can dominate the light-matter interaction, such as residual pump excitation, scattering [26], or hot band absorption [27]. Even when linear processes are eliminated, the low efficiencies of existing SPDC sources, which are typically around one entangled photon pair generated for every million pump

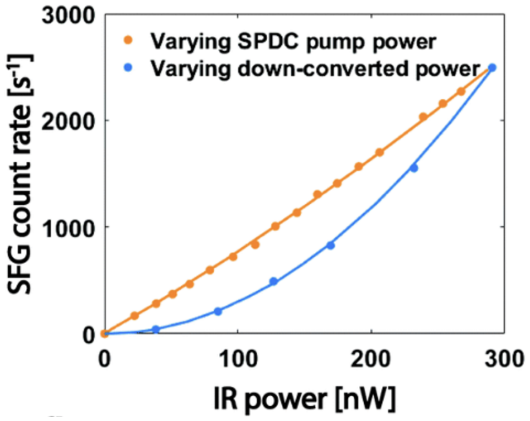

Figure 1.2: Demonstration of the linearization of classically nonlinear processes using entangled photons. Sum frequency generation (SFG) classically scales quadratically with the pump power (blue), but scales linearly when pumped with entangled photons (orange). Used with permission from Ref. [18]; permission conveyed through Copyright Clearance Center, Inc.

photons, coupled with the the low ETPA cross sections limit the current applications of ETPA even in the low flux regime [28–30].

The inherent quantum correlations of the photon pairs similarly enable time-resolved measurements using a continuous wave laser to generate entangled photons. Through energy-time entanglement, the photon pairs are deterministically correlated in time [31] and can thus act as a pulse with ultrafast correlation times ranging from tens to hundreds of femtoseconds [32, 33]. Utilizing these correlations for time-resolved fluorescence measurements (Figure 1.3), which are of interest for medical imaging [34, 35] and wearable devices [36, 37], entangled photons have the potential to replicate pulsed measurements at lower fluxes with greater wavelength tunability for sample multiplexing and without requiring external phase modulation [17]. However, the size and footprint of current SPDC sources as well as the associated collection optics limit miniaturization, adding complexity and cost for applications in portable spectrometers.

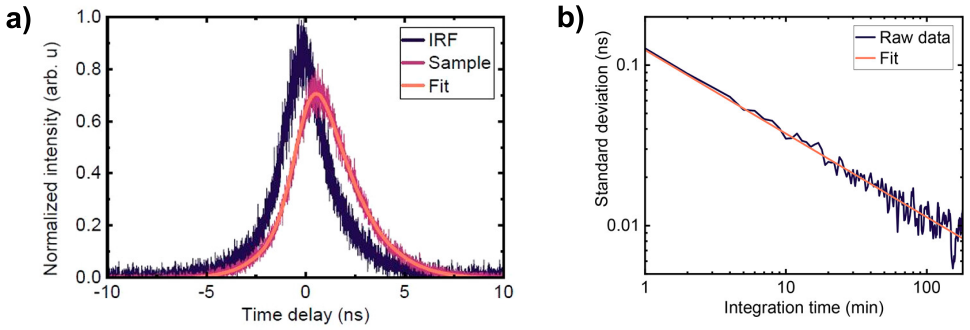

Figure 1.3: Fluorescence lifetime measurements for indocyanine green in dimethylsulfoxide using entangled photons. a) The base instrument response function (IRF, blue), measured indocyanine green sample response histogram (pink), and fitted histogram (orange). b) Standard deviation of the fluorescence lifetime fit with respect to integration time, demonstrating $N^{-1/2}$ scaling of the noise, where N is the number of detection events. Reprinted with permission from Ref. [17]. Copyright 2023 American Chemical Society.

Previous work in spectroscopy and sensing-focused applications of entangled photons such as ETPA and time-resolved fluorescence have utilized bulk crystal or large-area waveguide entangled photon sources (Figure 1.4a-b) that operate at visible and near-infrared wavelengths. These sources consist of bulk nonlinear optical crystals such as β-barium borate (BBO), periodically poled potassium titanyl phosphate (PPKTP), and periodically poled lithium niobate (PPLN), or ion-diffused waveguides fabricated through proton exchange or titanium diffusion. However,

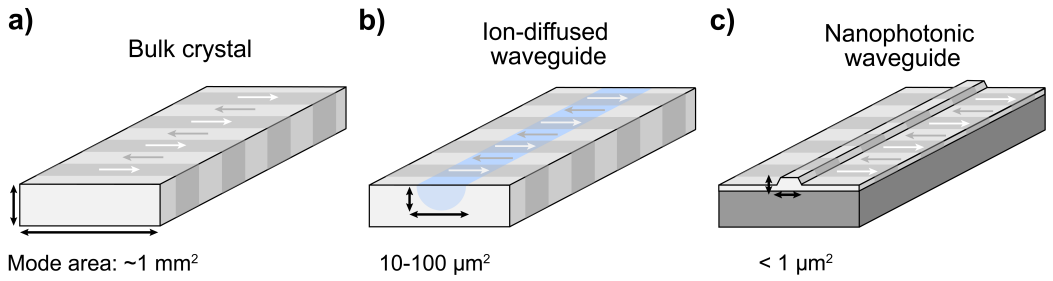

Figure 1.4: Illustration of the different types of SPDC sources in periodically poled lithium niobate. a) Bulk crystals, b) ion-diffused waveguides, and c) nanophotonic or TFLN waveguides.

the large mode area of bulk crystal sources limits the entangled photon generation efficiency, and the low index contrast of ion-diffused waveguides restricts the device bend radius, limiting dense photonic integration for compact devices.

Integrated optical platforms such as thin-film lithium niobate (TFLN) have seen rapid growth over the past few decades. Lithium niobate ($LiNbO_3$, LN) is a nonlinear optical crystal that can be described as the "silicon of photonics" due to its many advantageous material properties, including high electro-optic, piezoelectric, and nonlinear optical coefficients, wide transparency range, stability, and commercial availability [38]. Further leveraging these advantageous properties, the sub-μm^2 modal confinement of nanophotonic waveguides fabricated on the thin film platform (Figure 1.4c) enables highly efficient frequency conversion and quantum state generation as well as the small bend radii desired for dense photonic integration. Waveguide fabrication on TFLN through typical nanofabrication techniques also increases the degrees of freedom available for device design, enabling dispersion engineering through the waveguide geometry and allowing for modular integration of photonic components. Thus, photonic integrated circuits on TFLN have the potential to produce tailored, compact, and portable spectrometers with efficient frequency conversion, quantum state generation, state manipulation, and sample interaction all on a single compact chip.

Much of the previous work in TFLN waveguides has focused on infrared wavelengths for applications in quantum communication and computing, leaving the shorter wavelengths that are of interest for spectroscopy still a largely unexplored space. This thesis presents progress in lithium niobate nanophotonic waveguides in the ultraviolet through telecom wavelengths. Chapter 2 provides relevant back-

ground and theory of nonlinear optics and crystals. The derivation of the second harmonic generation (SHG) and SPDC efficiencies used in Chapters 3, 4, and 6 is reviewed. Chapter 3 presents a periodically poled TFLN waveguide fabricated for ultraviolet second harmonic generation. This device demonstrates SHG down to 355 nm, the shortest wavelength demonstrated in TFLN to date. Chapter 4 demonstrates spontaneous parametric downconversion from visible to near-infrared wavelengths in a periodically poled TFLN waveguide from a near-ultraviolet pump. The brightness and efficiency of this nanophotonic entangled photon source is orders of magnitude higher than that of the highest performing bulk crystal or diffused waveguide sources at these wavelengths, and the entangled photons from this source are the shortest wavelength photon pairs generated in TFLN by nearly an octave. Chapter 5 explores a fluorescent dye-doped polymer film cladded on a rib waveguide as a model system for evanescent wave sensing. The fundamental waveguide modes are compared in terms of scattering and fluorescence losses as criteria for a lithium niobate-based sensor. Chapter 6 expands upon the entangled photon pair generation in Chapter 4 to present preliminary work in entangled photon triplet generation through cascaded spontaneous parametric downconversion (CSPDC) from a near-ultraviolet pump to photon triplets at near-infrared and telecom wavelengths. This device is the first demonstration of CSPDC in TFLN waveguides to date, and the expected entangled photon triplet efficiency is orders of magnitude higher than previous demonstrations of CSPDC. Finally, Chapter 7 summarizes the results of this thesis and identifies several future research directions to improve device performance and incorporate downstream photonic elements towards a fully realized on-chip spectrometer.

References

[1] C. Xu, W. Zipfel, J. B. Shear, R. M. Williams, W. W. Webb, *Proceedings of the National Academy of Sciences* **1996**, *93*, 10763–10768.

[2] K. König, *Journal of Microscopy* **2000**, *200*, 83–104.

[3] S. Mukamel, *Principles of Nonlinear Optical Spectroscopy*, Oxford Univ. Press, New York, **2009**, 543 pp.

[4] P. Hamm, M. Zanni, *Concepts and Methods of 2D Infrared Spectroscopy*, 1st ed., Cambridge University Press, **2011**.

[5] M. Erhard, M. Krenn, A. Zeilinger, *Nature Reviews Physics* **2020**, *2*, 365–381.

[6] R. Horodecki, P. Horodecki, M. Horodecki, K. Horodecki, *Reviews of Modern Physics* **2009**, *81*, 865–942.

[7] S. Pirandola, U. L. Andersen, L. Banchi, M. Berta, D. Bunandar, R. Colbeck, D. Englund, T. Gehring, C. Lupo, C. Ottaviani, J. L. Pereira, M. Razavi, J. Shamsul Shaari, M. Tomamichel, V. C. Usenko, G. Vallone, P. Villoresi, P. Wallden, *Advances in Optics and Photonics* **2020**, *12*, 1012.

[8] N. Gisin, R. Thew, *Nature Photonics* **2007**, *1*, 165–171.

[9] J. L. O'Brien, *Science* **2007**, *318*, 1567–1570.

[10] L. Xiao, G. Lu Long, F.-G. Deng, J.-W. Pan, *Physical Review A* **2004**, *69*, 052307.

[11] T. Ono, R. Okamoto, S. Takeuchi, *Nature Communications* **2013**, *4*, 2426.

[12] O. Jedrkiewicz, Y.-K. Jiang, E. Brambilla, A. Gatti, M. Bache, L. A. Lugiato, P. Di Trapani, *Physical Review Letters* **2004**, *93*, 243601.

[13] G. Brida, M. Genovese, I. Ruo Berchera, *Nature Photonics* **2010**, *4*, Publisher: Springer Science and Business Media LLC, 227–230.

[14] A. N. Boto, P. Kok, D. S. Abrams, S. L. Braunstein, C. P. Williams, J. P. Dowling, *Physical Review Letters* **2000**, *85*, 2733–2736.

[15] C. A. Casacio, L. S. Madsen, A. Terrasson, M. Waleed, K. Barnscheidt, B. Hage, M. A. Taylor, W. P. Bowen, *Nature* **2021**, *594*, 201–206.

[16] D. Tabakaev, M. Montagnese, G. Haack, L. Bonacina, J.-P. Wolf, H. Zbinden, R. T. Thew, *Physical Review A* **2021**, *103*, 033701.

[17] N. Harper, B. P. Hickam, M. He, S. K. Cushing, *The Journal of Physical Chemistry Letters* **2023**, *14*, 5805–5811.

[18] S. Szoke, H. Liu, B. P. Hickam, M. He, S. K. Cushing, *Journal of Materials Chemistry C* **2020**, *8*, 10732–10741.

[19] K. Y. Spasibko, D. A. Kopylov, V. L. Krutyanskiy, T. V. Murzina, G. Leuchs, M. V. Chekhova, *Physical Review Letters* **2017**, *119*, 223603.

[20] T. Landes, M. Allgaier, S. Merkouche, B. J. Smith, A. H. Marcus, M. G. Raymer, *Physical Review Research* **2021**, *3*, 033154.

[21] D. Tabakaev, A. Djorović, L. La Volpe, G. Gaulier, S. Ghosh, L. Bonacina, J.-P. Wolf, H. Zbinden, R. T. Thew, *Physical Review Letters* **2022**, *129*, 183601.

[22] Z. Y. Ou, X. Y. Zou, L. J. Wang, L. Mandel, *Physical Review Letters* **1990**, *65*, 321–324.

[23] J. Gea-Banacloche, *Physical Review Letters* **1989**, *62*, 1603–1606.

[24] J. Javanainen, P. L. Gould, *Physical Review A* **1990**, *41*, 5088–5091.

[25] F. Schlawin, K. E. Dorfman, S. Mukamel, *Accounts of Chemical Research* **2018**, *51*, 2207–2214.

[26] B. P. Hickam, M. He, N. Harper, S. Szoke, S. K. Cushing, *The Journal of Physical Chemistry Letters* **2022**, *13*, 4934–4940.

[27] A. Mikhaylov, R. N. Wilson, K. M. Parzuchowski, M. D. Mazurek, C. H. Camp, M. J. Stevens, R. Jimenez, *The Journal of Physical Chemistry Letters* **2022**, *13*, 1489–1493.

[28] F. Schlawin, A. Buchleitner, *New Journal of Physics* **2017**, *19*, 013009.

[29] T. Landes, M. G. Raymer, M. Allgaier, S. Merkouche, B. J. Smith, A. H. Marcus, *Optics Express* **2021**, *29*, 20022.

[30] M. He, B. P. Hickam, N. Harper, S. K. Cushing, *The Journal of Chemical Physics* **2024**, *160*, 094305.

[31] J.-P. W. MacLean, J. M. Donohue, K. J. Resch, *Physical Review Letters* **2018**, *120*, 053601.

[32] N. A. Harper, E. Y. Hwang, R. Sekine, L. Ledezma, C. Perez, A. Marandi, S. K. Cushing, *Optica Quantum* **2024**, *2*, 103.

[33] M. B. Nasr, S. Carrasco, B. E. A. Saleh, A. V. Sergienko, M. C. Teich, J. P. Torres, L. Torner, D. S. Hum, M. M. Fejer, *Physical Review Letters* **2008**, *100*, 183601.

[34] Z. Wang, Y. Zheng, D. Zhao, Z. Zhao, L. Liu, A. Pliss, F. Zhu, J. Liu, J. Qu, P. Luan, *Journal of Innovative Optical Health Sciences* **2018**, *11*, 1830001.

[35] Y. Ouyang, Y. Liu, Z. M. Wang, Z. Liu, M. Wu, *Nano-Micro Letters* **2021**, *13*, 133.

[36] A. S. Paterson, B. Raja, V. Mandadi, B. Townsend, M. Lee, A. Buell, B. Vu, J. Brgoch, R. C. Willson, *Lab on a Chip* **2017**, *17*, 1051–1059.

[37] D. S. Elson, J. A. Jo, L. Marcu, *New Journal of Physics* **2007**, *9*, 127–127.

[38] A. Boes, L. Chang, C. Langrock, M. Yu, M. Zhang, Q. Lin, M. Lončar, M. Fejer, J. Bowers, A. Mitchell, *Science* **2023**, *379*, eabj4396.

Chapter 2

NONLINEAR OPTICAL PROCESSES

This chapter covers the fundamentals of nonlinear optics and the relevant equations for the frequency conversion processes described in Chapters 3, 4, and 6. The coupled wave equations for second order nonlinear processes are revisited to derive the efficiencies for sum frequency generation and second harmonic generation. The theory of spontaneous parametric downconversion in waveguides is described. The different types of phase matching in nonlinear crystals, including perfect, birefringent, and quasi-phase matching, are discussed. Finally, the properties of nonlinear crystals, particularly lithium niobate, are reviewed. Appendix A serves as a supplement to review the wave equations and other pertinent equations for electromagnetic propagation.

2.1 Nonlinear optics

Nonlinear optics is the study of the nonlinear change in optical properties in response to a strong electromagnetic field, such as a laser. To understand the source of nonlinear optics, we can first revisit the fundamental equations of electromagnetism.

The constitutive relation between the electric displacement $\mathbf{D}$ and the electric field $\mathbf{E}$ is used to define the polarization density $\mathbf{P}$ and the permittivity ε of a material [1]:

$$\begin{aligned} \mathbf{D} &= \varepsilon \mathbf{E} \\ &= \varepsilon_0 \mathbf{E} + \mathbf{P} \end{aligned} \tag{2.1}$$

where ε_0 is the vacuum permittivity. A review of Maxwell's equations and the derivation of the wave equations for electromagnetic fields a can be found in Appendix A.1.

In linear materials, the induced polarization is directly proportional to the electric field:

$$\mathbf{P} = \varepsilon_0 \chi^{(1)} \mathbf{E} \tag{2.2}$$

where $\chi^{(1)}$ is a constant known as the linear susceptibility. However, this linear relation between $\mathbf{P}$ and $\mathbf{E}$ does not hold for many real systems. To account for nonlinear effects, the polarization can be separated into its linear and nonlinear

components, which can be represented with a Taylor expansion [2, 3]:

$$\begin{aligned}\mathbf{P} &= \mathbf{P}_L + \mathbf{P}_{NL} \\ &= \mathbf{P}^{(1)} + \mathbf{P}^{(2)} + \mathbf{P}^{(3)} + ... \\ &= \varepsilon_0 \chi^{(1)} \mathbf{E}_1 + \varepsilon_0 \chi^{(2)} \mathbf{E}_1 \mathbf{E}_2 + \varepsilon_0 \chi^{(3)} \mathbf{E}_1 \mathbf{E}_2 \mathbf{E}_3 + ...\end{aligned} \tag{2.3}$$

where the linear polarization $\mathbf{P}_L$ is defined analogously to Equation 2.2 for linear crystals:

$$\mathbf{P}_L = \mathbf{P}^{(1)} = \varepsilon_0 \chi^{(1)} \mathbf{E}_1 \tag{2.4}$$

while the nonlinear polarization $\mathbf{P}_{NL}$ is defined as:

$$\begin{aligned}\mathbf{P}_{NL} &= \mathbf{P}^{(2)} + \mathbf{P}^{(3)} + ... \\ &= \varepsilon_0 \chi^{(2)} \mathbf{E}_1 \mathbf{E}_2 + \varepsilon_0 \chi^{(3)} \mathbf{E}_1 \mathbf{E}_2 \mathbf{E}_3 + ...\end{aligned} \tag{2.5}$$

Second order nonlinear processes, such as the frequency conversion processes described in this thesis, involve the mixing of three waves and utilize the $\mathbf{P}^{(2)}$ term of the nonlinear polarization. The d tensor for the second order nonlinear coefficient is often used to denote the nonlinear susceptibility in place of $\chi^{(2)}$, with the relation:

$$d_{ijk} = \frac{1}{2} \chi^{(2)}_{ijk} \tag{2.6}$$

where $i, j, k = x, y, z$. The second order polarization can then be generally represented with a summation:

$$\mathbf{P}^{(2)} = \sum_{i=x,y,z} P_i = \sum_{i,j,k=x,y,z} 2\varepsilon_0 d_{ijk} E_j E_k. \tag{2.7}$$

2.2 Coupled wave equations

Using the expression for the nonlinear polarization, the efficiencies of commonly used second order nonlinear processes such as sum frequency and second harmonic generation can be derived. Consider an electric field at two frequencies ω_1 and ω_2 with the form:

$$\mathbf{E} = \frac{1}{2}(E_1 e^{-i\omega_1 t} + E_2 e^{-i\omega_2 t} + \text{c.c.}) \tag{2.8}$$

where c.c. stands for the complex conjugate and E_1 and E_2 are the magnitudes of the electric fields at frequencies ω_1 and ω_2. Using this form for $\mathbf{E}$ in the general form of the second order polarization $\mathbf{P}^{(2)}$ in Equation 2.5 and expanding out the

terms, the following expression can be obtained:

$$\begin{aligned}\mathbf{P}^{(2)} &= \varepsilon_0 \chi^{(2)} \mathbf{E}^2 \\ &= \varepsilon_0 \chi^{(2)} \left(\frac{1}{2}(E_1 e^{-i\omega_1 t} + E_2 e^{-i\omega_2 t} + \text{c.c.}) \right)^2 \\ &= \frac{\varepsilon_0 \chi^{(2)}}{4} \Big(E_1^2 e^{-2i\omega_1 t} + E_2^2 e^{-2i\omega_2 t} + 2E_1 E_2 e^{-i(\omega_1+\omega_2)t} + 2E_1 E_2^* e^{-i(\omega_1-\omega_2)t} \\ &\quad + 2|E_1|^2 + 2|E_2|^2 + \text{c.c.} \Big).\end{aligned} \tag{2.9}$$

The polarization can also be expressed using the notation:

$$\mathbf{P} = \frac{1}{2} \sum_n (P_{\omega_n} e^{-i\omega_n t} + \text{c.c.}). \tag{2.10}$$

Using the equality between Equations 2.9 and 2.10, we can see that each of the terms in Equation 2.9 corresponds to a particular physical process. Considering sum frequency generation (SFG), which involves the generation of an electric field at frequency $\omega_3 = \omega_1 + \omega_2$, the amplitude of the second order polarization can be assigned as:

$$\begin{aligned}P_{\omega_3} &= \varepsilon_0 \chi^{(2)} E_1 E_2 \\ &= 2\varepsilon_0 d_{\text{eff}} E_1 E_2.\end{aligned} \tag{2.11}$$

Note that d_{ijk} from Equation 2.7 has been replaced with d_{eff} to generalize for the polarizations of the fields. Now consider plane waves with z propagation of the form:

$$\mathbf{E}_i = \frac{1}{2}(A_i e^{i(k_i z - \omega_i t)} + \text{c.c}) \tag{2.12}$$

where $k_i = \frac{n_i \omega_i}{c}$ is the propagation constant and the amplitude A_i is a constant. By setting $E_i = A_i e^{ik_i z}$, this representation of the electric field is consistent with Equation 2.8. Using the amplitudes A_i in Equation 2.11 and changing the subscripts so that $P_{\omega_3} = P_3$:

$$\begin{aligned}P_{\omega_3} = P_3 &= 2\varepsilon_0 d_{\text{eff}} A_1 e^{ik_1 z} A_2 e^{ik_2 z} \\ &= 2\varepsilon_0 d_{\text{eff}} A_1 A_2 e^{i(k_1+k_2)z}.\end{aligned} \tag{2.13}$$

Using this expression, we can now revisit the nonlinear wave equation (Equation A.29). The derivations for the linear and nonlinear wave equations can be found in Appendix A.

$$\nabla^2 \mathbf{E}_3 - \mu\varepsilon \frac{\partial^2 \mathbf{E}_3}{\partial t^2} - \mu \frac{\partial^2 \mathbf{P}_{NL}}{\partial t^2} = 0 \tag{2.14}$$

For the field $\mathbf{E}_3 = \frac{1}{2}(A_3 e^{i(k_3 z - \omega_3 t)} + \text{c.c.})$ and nonlinear polarization $\mathbf{P}_{NL} = \mathbf{P}_3 = \frac{1}{2}(P_3 e^{-i\omega_3 t} + \text{c.c.})$, the wave equation becomes:

$$\nabla^2\Big(\frac{1}{2}(A_3 e^{i(k_3 z - \omega_3 t)} + \text{c.c.})\Big) - \mu\varepsilon\frac{\partial^2}{\partial t^2}\Big(\frac{1}{2}(A_3 e^{i(k_3 z - \omega_3 t)} + \text{c.c.})\Big) = \mu\frac{\partial^2}{\partial t^2}\Big(\frac{1}{2}(2\varepsilon_0 d_{\text{eff}} A_1 A_2 e^{i((k_1+k_2)z - \omega_3 t)} + \text{c.c.})\Big). \quad (2.15)$$

Cancelling out the $\frac{1}{2}e^{-i\omega_3 t}$ factor from all terms and noting that the Laplacian ∇^2 can be reduced to $\frac{\partial^2}{\partial z^2}$ for plane waves simplifies this expression to:

$$\frac{\partial^2 A_3}{\partial z^2}e^{ik_3 z} + 2ik_3\frac{\partial A_3}{\partial z}e^{ik_3 z} + \text{c.c.} = -2\varepsilon_0\mu A_1 A_2\omega_3^2 e^{i(k_1+k_2)z} + \text{c.c.} \quad (2.16)$$

Note that the complex conjugate terms can be dropped, and this expression will still maintain equality. The momentum or wavevector mismatch Δk can also be defined as

$$\Delta k = k_3 - k_1 - k_2 \quad (2.17)$$

to get the expression:

$$\frac{\partial^2 A_3}{\partial z^2} + 2ik_3\frac{\partial A_3}{\partial z} = -2\varepsilon_0\mu A_1 A_2\omega_3^2 e^{-i\Delta k z}. \quad (2.18)$$

Using the slowly varying amplitude approximation, the $\frac{\partial^2 A_3}{\partial z^2}$ term can be neglected:

$$\left|\frac{\partial^2 A_3}{\partial z^2}\right| << \left|k_3\frac{\partial A_3}{\partial z}\right|. \quad (2.19)$$

Isolating the derivative term and using $k_3 = \frac{n_3\omega_3}{c}$ produces the coupled wave equation for SFG:

$$\frac{\partial A_3}{\partial z} = i\frac{\mu\varepsilon_0 c d_{\text{eff}}\omega_3}{n_3}A_1 A_2 e^{-i\Delta k z} \quad (2.20)$$

where the spatial derivative of the sum frequency field $\frac{\partial A_3}{\partial z}$ is coupled with the fields A_1 and A_2. Integrating $\frac{\partial A_3}{\partial z}$ from 0 to L, an expression for A_3 can be obtained:

$$\begin{aligned} A_3 &= \int_0^L \frac{\partial A_3}{\partial z}dz \\ &= \int_0^L i\frac{\mu\varepsilon_0 c d_{\text{eff}}\omega_3}{n_3}A_1 A_2 e^{-i\Delta k z} \\ &= -\frac{\mu\varepsilon_0 c d_{\text{eff}}\omega_3}{n_3}A_1 A_2\frac{e^{-i\Delta k L} - 1}{\Delta k}. \end{aligned} \quad (2.21)$$

We can now consider the intensity, which is given by the time-averaged Poynting vector:

$$I_i = \frac{1}{2}n_i\varepsilon_0 c|A_i|^2 \quad (2.22)$$

so the intensity of the field at ω_3 is:

$$\begin{aligned} I_3 &= \frac{1}{2} n_3 \varepsilon_0 c |A_3|^2 \\ &= \frac{1}{2} n_3 \varepsilon_0 c \left| -\frac{\mu \varepsilon_0 c d_{\text{eff}} \omega_3}{n_3} A_1 A_2 \frac{e^{-i\Delta k L} - 1}{\Delta k} \right|^2 \\ &= \frac{\mu^2 \varepsilon_0^3 c^3 d_{\text{eff}}^2 \omega_3^2}{2 n_3} |A_1|^2 |A_2|^2 \frac{2(1 - \cos(\Delta k L))}{\Delta k^2}. \end{aligned} \tag{2.23}$$

Using the cosine double angle identity and the definition $\text{sinc}(x) = \frac{\sin(x)}{x}$, the following expression can be obtained:

$$I_3 = \frac{\mu^2 \varepsilon_0^3 c^3 d_{\text{eff}}^2 \omega_3^2 L^2}{2 n_3} |A_1|^2 |A_2|^2 \text{sinc}^2 \left(\frac{\Delta k L}{2} \right). \tag{2.24}$$

Finally, $|A_1|^2$ and $|A_2|^2$ can also be replaced with their respective intensities:

$$\begin{aligned} I_3 &= \frac{\mu^2 \varepsilon_0^3 c^3 d_{\text{eff}}^2 \omega_3^2 L^2}{2 n_3} \frac{2 I_1}{n_1 \varepsilon_0 c} \frac{2 I_2}{n_2 \varepsilon_0 c} \text{sinc}^2 \left(\frac{\Delta k L}{2} \right) \\ &= \frac{2 d_{\text{eff}}^2 \omega_3^2 L^2}{n_1 n_2 n_3 \varepsilon_0 c^3} I_1 I_2 \text{sinc}^2 \left(\frac{\Delta k L}{2} \right). \end{aligned} \tag{2.25}$$

In terms of optical powers P_i instead of intensities, a similar expression can be obtained for the generated power at ω_3 [4, 5]:

$$\text{P}_3 = \frac{2 d_{\text{eff}}^2 \omega_3^2 L^2}{n_1 n_2 n_3 \varepsilon_0 c^3 A_{\text{eff}}} \text{P}_1 \text{P}_2 \text{sinc}^2 \left(\frac{\Delta k L}{2} \right) \tag{2.26}$$

where A_{eff} is the effective mode interaction area. So we find that:

$$\frac{P_3}{P_1 P_2} = \eta_{0,\text{SFG}} L^2 \text{sinc}^2 \left(\frac{\Delta k L}{2} \right) \tag{2.27}$$

where the normalized conversion efficiency η_0 for SFG is defined as:

$$\eta_{0,\text{SFG}} = \frac{2 d_{\text{eff}}^2 \omega_3^2}{n_1 n_2 n_3 \varepsilon_0 c^3 A_{\text{eff}}}. \tag{2.28}$$

Second harmonic generation

Although the equations presented so far were specified for SFG, a similar and related second order process is second harmonic generation (SHG). In SHG, a field at frequency $\omega_3 = 2\omega_1$ is generated, where ω_3 is known as the second harmonic signal of the first harmonic ω_1. In this way, SHG can be thought of as a special case of SFG when $\omega_1 = \omega_2$ and $n_1 = n_2$. The normalized SHG conversion efficiency is therefore given by:

$$\eta_{0,\text{SHG}} = \frac{2 d_{\text{eff}}^2 \omega_3^2}{n_1^2 n_3 \varepsilon_0 c^3 A_{\text{eff}}}. \tag{2.29}$$

2.3 Spontaneous parametric downconversion

SFG and SHG are commonly used second order processes for classical frequency conversion. Spontaneous parametric downconversion (SPDC) is a related process that has been used for decades to produce quantum entanglement. SPDC can be thought of as the time-reversed process of SHG or SFG. In SFG and SHG, two lower energy photons interact to produce a higher energy photon at the sum of their frequencies (Figure 2.1a-b); however, in SPDC, a higher energy photon interacts with the vacuum state to downconvert into an entangled pair of photons (Figure 2.1c-d). No interaction or frequency downconversion would be predicted to occur classically without the presence of another field, so SPDC cannot be described with a fully classical treatment.

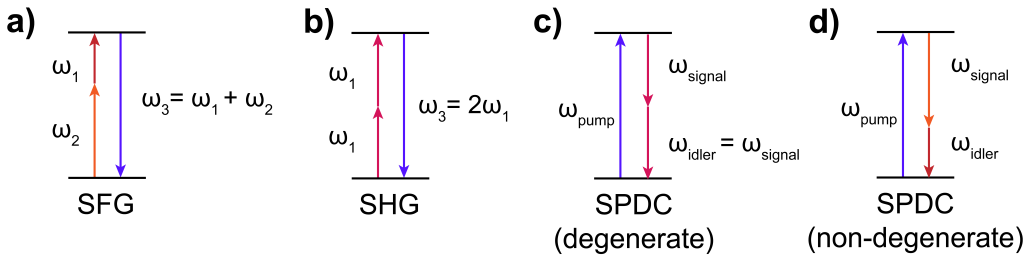

Figure 2.1: Photon energy picture of a) SFG, b) SHG, c) degenerate SPDC, and d) non-degenerate SPDC.

To derive the SPDC efficiency in waveguides following Ref. [6], a semiclassical approach can be used by quantizing the signal and idler fields but utilizing a classical pump beam. The quantized electric field is given by [7]:

$$\mathbf{E}_{s,i}(\mathbf{r},t) = i\left(\sum_k c^{(k)}u^{(k)}(\mathbf{r})e^{-i\omega^{(k)}t} + \text{c.c}\right) \tag{2.30}$$

where $c^{(k)}$ are Fourier coefficients, and $u^{(k)}(\mathbf{r})$ are the mode vector functions corresponding to frequencies $\omega^{(k)}$, and the summation is over the number of modes k. The modes satisfy the following conditions:

$$\left(\nabla^2 + \frac{(\omega^{(k)})^2}{n^2c^2}\right)u^{(k)} = 0 \tag{2.31}$$

$$\nabla \cdot u^{(k)} = 0 \tag{2.32}$$

$$\int_V (u^{(k)})^* u^{(k')} = \delta_{kk'}. \tag{2.33}$$

In waveguides, the solutions $u_k(\mathbf{r})$ can be assumed to be separable. With propagation along the z direction, they can be represented as:

$$u^{(k)}(\mathbf{r}) = \frac{1}{\sqrt{L}} U^{(k)}(x, y) e^{i\beta_k z} \tag{2.34}$$

where L is the length of the quantization volume along the propagation axis, β_k is the propagation constant, and the mode profile $U^{(k)}$ is normalized so that $\int_A |U^{(k)}(x, y)|^2 dxdy = 1$ over the cross-sectional quantization area A.

The electric field operator for the signal and idler photons $\hat{\mathbf{E}}_{s,i}$ can be defined as:

$$\begin{aligned} \hat{\mathbf{E}}_{s,i} &= \frac{1}{2}\left(\hat{\mathrm{E}}_{s,i}(\mathbf{r}, t) + \hat{\mathrm{E}}^{\dagger}_{s,i}(\mathbf{r}, t\right) \\ &= \frac{1}{2}\left(i \sum_k c^{(k)} u^{(k)}(\mathbf{r}) e^{-i\omega^{(k)}_{s,i} t} \hat{a}^{(k)}_{s,i} + \mathrm{h.c}\right) \\ &= \frac{i}{2} \sum_k \left(\sqrt{\frac{2\hbar\omega^{(k)}_{s,i}}{L n^2_{s,i} \varepsilon_0}} U^{(k)}_{s,i} e^{i(\beta^{(k)}_{s,i} z - \omega^{(k)}_{s,i} t)} \hat{a}^{(k)}_{s,i} + \mathrm{h.c.}\right) \end{aligned} \tag{2.35}$$

where the constant $c^{(k)}$ is chosen to maintain the commutation rules for the creation and annihilation operators $\hat{a}^{\dagger}$ and $\hat{a}$, and h.c. represents the Hermitian conjugate. The pump field $\mathbf{E}_p$ can be defined classically:

$$\begin{aligned} \mathbf{E}_p &= \frac{1}{2}\left(E_p(\mathbf{r}, t) + \mathrm{c.c.}\right) \\ &= \frac{1}{2}\left(\sqrt{\frac{2\mathrm{P}_p}{n_p \varepsilon_0 c}} U_p e^{i(\beta_p z - \omega_p t)} + \mathrm{c.c.}\right) \end{aligned} \tag{2.36}$$

where the mode profile U_p is normalized so that $\int_A |U_p(x, y)|^2 dxdy = 1$, and the pump power P_p is obtained from integrating the time-averaged Poynting vector over the area, or $\mathrm{P}_p = \int_A \frac{1}{2} n_p \varepsilon_0 c |E_p|^2 dxdy$.

The interaction Hamiltonian can be represented as [8]:

$$\hat{H}_I = -\frac{\varepsilon_0 d_{\mathrm{eff}}}{2} \int_C \left(E_p \hat{E}^{\dagger}_s \hat{E}^{\dagger}_i + \mathrm{h.c.}\right) \tag{2.37}$$

where $C = LA$ is the crystal volume. Using the expressions from Equations 2.35

and 2.36 in the expression for the Hamiltonian produces the expression:

$$\hat{H}_I = -\frac{\varepsilon_0 d_{\text{eff}}}{2}\left(\int_C \left(\sqrt{\frac{2\text{P}_p}{n_p\varepsilon_0 c}}U_p e^{i(\beta_p z-\omega_p t)}\right)\right.$$
$$\left(-i\sum_j \sqrt{\frac{2\hbar\omega_s^{(j)}}{Ln_s^2\varepsilon_0}}\left(U_s^{(j)}\right)^* e^{-i(\beta_s^{(j)}z-\omega_s^{(j)}t)}\left(\hat{a}_s^{(j)}\right)^\dagger\right)$$
$$\left.\left(-i\sum_k \sqrt{\frac{2\hbar\omega_i^{(k)}}{Ln_i^2\varepsilon_0}}\left(U_i^{(k)}\right)^* e^{-i(\beta_i^{(k)}z-\omega_i^{(k)}t)}\left(\hat{a}_i^{(k)}\right)^\dagger\right)+\text{h.c.}\right). \quad (2.38)$$

Simplifying and collecting terms:

$$\hat{H}_I = \frac{\hbar d_{\text{eff}}}{L}\sqrt{\frac{2\text{P}_p}{n_p n_s^2 n_i^2\varepsilon_0 c}}\left(\int_C \sum_{j,k}\sqrt{\omega_s^{(j)}\omega_i^{(k)}}U_p(U_s^{(j)})^*(U_i^{(k)})^*\right.$$
$$\left.e^{i((\beta_p-\beta_s^{(j)}-\beta_i^{(k)})z-(\omega_p-\omega_s^{(j)}-\omega_i^{(k)})t)}\left(\hat{a}_s^{(j)}\right)^\dagger\left(\hat{a}_i^{(k)}\right)^\dagger+\text{h.c.}\right). \quad (2.39)$$

Now Fermi's golden rule can be used to calculate the transition rate between the initial state $|i\rangle$ and the final state $|f\rangle$:

$$W = \frac{2\pi}{\hbar}\left|\langle f|\hat{H}_I|i\rangle\right|^2\rho \quad (2.40)$$

where ρ is the density of states. For SPDC, the initial state $|i\rangle$ is the vacuum state, or no photons in either the signal or idler modes ($|i\rangle = |\text{vac}\rangle = |00\rangle$). The final state is the state with one photon in each of the signal and idler modes. We can denote the signal and idler modes as modes l and m and represent the final state with creation and annihilation operators as $|f\rangle = |11\rangle = \left(\hat{a}_s^{(l)}\right)^\dagger\left(\hat{a}_i^{(m)}\right)^\dagger|00\rangle$.

So now we can find an expression for $\langle f|\hat{H}_I|i\rangle$:

$$\langle f|\hat{H}_I|i\rangle = \langle 00|\hat{a}_s^{(l)}\hat{a}_i^{(m)}\frac{\hbar d_{\text{eff}}}{L}\sqrt{\frac{2\text{P}_p}{n_p n_s^2 n_i^2\varepsilon_0 c}}\left(\int_C \sum_{j,k}\sqrt{\omega_s^{(j)}\omega_i^{(k)}}U_p(U_s^{(j)})^*(U_i^{(k)})^*\right.$$
$$\left.e^{i((\beta_p-\beta_s^{(j)}-\beta_i^{(k)})z-(\omega_p-\omega_s^{(j)}-\omega_i^{(k)})t)}\left(\hat{a}_s^{(j)}\right)^\dagger\left(\hat{a}_i^{(k)}\right)^\dagger+\text{h.c.}\right)|00\rangle. \quad (2.41)$$

This expression can be simplified by using the l and m modes to reduce the summation over j and k, where $l \in j$ and $m \in k$:

$$\langle f|\hat{H}_I|i\rangle = \frac{\hbar d_{\text{eff}}}{L}\sqrt{\frac{2\text{P}_p}{n_p n_s^2 n_i^2 \varepsilon_0 c}}\left(\int_C \sqrt{\omega_s^{(l)}\omega_i^{(m)}}U_p (U_s^{(l)})^* (U_i^{(k)})^* \right.$$
$$\left. e^{i((\beta_p-\beta_s^{(l)}-\beta_i^{(m)})z-(\omega_p-\omega_s^{(j)}-\omega_i^{(m)})t)}\right)\langle 00|\hat{a}_s^{(l)}\hat{a}_i^{(m)}\left(\hat{a}_s^{(l)}\right)^\dagger\left(\hat{a}_i^{(m)}\right)^\dagger|00\rangle. \quad (2.42)$$

For simplicity, the mode superscripts can be dropped so that the signal variables are represented as $\omega_s = \omega_s^{(l)}$, $\beta_s = \beta_s^{(l)}$, $U_s = U_s^{(l)}$, $\hat{a}_s = \hat{a}_s^{(l)}$, and so on for the idler. Imposing the condition for energy conservation ($\omega_p = \omega_s + \omega_i$) and utilizing a similar expression for the momentum mismatch as in Equation 2.17 ($\Delta\beta = \beta_p - \beta_s - \beta_i$) produces the following expression:

$$\langle f|\hat{H}_I|i\rangle = \frac{\hbar d_{\text{eff}}}{L}\sqrt{\frac{2\text{P}_p\omega_s\omega_i}{n_p n_s^2 n_i^2 \varepsilon_0 c}}\int_C U_p U_s^* U_i^* e^{i\Delta\beta z}\langle 00|\hat{a}_s\hat{a}_i\hat{a}_s^\dagger\hat{a}_i^\dagger|00\rangle. \quad (2.43)$$

Recalling the commutation relation for the creation and annihilation operators $[\hat{a}_i, \hat{a}_j^\dagger] = \delta_{ij}$, we can simplify $\langle 00|\hat{a}_s\hat{a}_i\hat{a}_s^\dagger\hat{a}_i^\dagger|00\rangle = \langle 00|00\rangle = 1$. Finally, we can integrate over the crystal volume $C = LA$ and take the magnitude to get the final expression for $\left|\langle f|\hat{H}_I|i\rangle\right|^2$:

$$\begin{aligned}
\left|\langle f|\hat{H}_I|i\rangle\right|^2 &= \left|\frac{\hbar d_{\text{eff}}}{L}\sqrt{\frac{2\text{P}_p\omega_s\omega_i}{n_p n_s^2 n_i^2 \varepsilon_0 c}}\int_A\int_L U_p U_s^* U_i^* e^{i\Delta\beta z}\right|^2 \\
&= \left|\frac{\hbar d_{\text{eff}}}{L}\sqrt{\frac{2\text{P}_p\omega_s\omega_i}{n_p n_s^2 n_i^2 \varepsilon_0 c}}\int_A U_p U_s^* U_i^* dxdy\int_L e^{i\Delta\beta z}dz\right|^2 \\
&= \left(\frac{\hbar d_{\text{eff}}}{L}\sqrt{\frac{2\text{P}_p\omega_s\omega_i}{n_p n_s^2 n_i^2 \varepsilon_0 c A_{\text{eff}}}}\right)^2\left|\frac{e^{i\Delta\beta L}-1}{i\Delta\beta}\right|^2 \\
&= \frac{2\hbar^2 d_{\text{eff}}^2 \text{P}_p\omega_s\omega_i}{n_p n_s^2 n_i^2 \varepsilon_0 c A_{\text{eff}}}\text{sinc}^2\left(\frac{\Delta\beta L}{2}\right)
\end{aligned} \quad (2.44)$$

where the interaction area A_{eff} can be defined as $A_{\text{eff}} = \sqrt{\int_A U_p U_s^* U_i^* dxdy}$. For Fermi's golden rule (Equation 2.40), an expression for the density of states $\rho = \frac{dN}{dE}$ can also be found, where N is the number of states and E is the energy. In one dimensional state space:

$$dN = \frac{L}{2\pi}dk \quad (2.45)$$

For photons, the energy is given by $E = \hbar\omega$, so $k = \frac{\omega n}{c} = \frac{En}{\hbar c}$. Therefore $dk = \frac{n}{\hbar c} dE$, and plugging dk into the expression for dN:

$$dN = \frac{L}{2\pi}\frac{n}{\hbar c} dE. \tag{2.46}$$

So considering the change in the number of states for both the signal and the idler modes:

$$dN = dN_s dN_i = \left(\frac{L}{2\pi}\frac{n_s}{\hbar c} dE_s\right)\left(\frac{L}{2\pi}\frac{n_i}{\hbar c} dE_i\right) \tag{2.47}$$

and from energy conservation, we know $dE = dE_s = dE_i = \hbar d\omega_s$:

$$dN = \left(\frac{L}{2\pi}\right)^2 \frac{n_s n_i}{\hbar c^2} dE\, d\omega_s. \tag{2.48}$$

Therefore, the density of states is:

$$\rho = \frac{dN}{dE} = \left(\frac{L}{2\pi}\right)^2 \frac{n_s n_i}{\hbar c^2} d\omega_s. \tag{2.49}$$

The expressions for $\left|\langle f|\hat{H}_I|i\rangle\right|^2$ (Equation 2.44) and ρ (Equation 2.49) can now be plugged into Fermi's golden rule (Equation 2.40) to obtain the transition rate:

$$\begin{aligned} W &= \frac{2\pi}{\hbar}\left|\langle f|\hat{H}_I|i\rangle\right|^2 \rho \\ &= \frac{2\pi}{\hbar}\left(\frac{2\hbar^2 d_{\text{eff}}^2 \mathrm{P}_p \omega_s \omega_i}{n_p n_s^2 n_i^2 \varepsilon_0 c A_{\text{eff}}} \mathrm{sinc}^2\left(\frac{\Delta\beta L}{2}\right)\right)\left(\left(\frac{L}{2\pi}\right)^2 \frac{n_s n_i}{\hbar c^2} d\omega_s\right) \\ &= \frac{d_{\text{eff}}^2 \mathrm{P}_p \omega_s \omega_i L^2}{\pi \varepsilon_0 c^3 n_p n_s n_i A_{\text{eff}}} \mathrm{sinc}^2\left(\frac{\Delta\beta L}{2}\right) d\omega_s. \end{aligned} \tag{2.50}$$

Finally, the downconverted signal power $d\mathrm{P}_s = \hbar\omega_s W$ in the frequency interval $d\omega_s$ is given by:

$$d\mathrm{P}_s = \frac{\hbar d_{\text{eff}}^2 \mathrm{P}_p \omega_s^2 \omega_i L^2}{\pi \varepsilon_0 c^3 n_p n_s n_i A_{\text{eff}}} \mathrm{sinc}^2\left(\frac{\Delta\beta L}{2}\right) d\omega_s. \tag{2.51}$$

To obtain theoretical SPDC spectra, Equation 2.51 can be numerically integrated over all frequencies:

$$\mathrm{P}_s = \int \frac{\hbar d_{\text{eff}}^2 \mathrm{P}_p \omega_s^2 \omega_i L^2}{\pi \varepsilon_0 c^3 n_p n_s n_i A_{\text{eff}}} \mathrm{sinc}^2\left(\frac{\Delta\beta L}{2}\right) d\omega_s. \tag{2.52}$$

2.4 Quasi-phase matching

From the treatment of SFG and SHG in Section 2.2 and SPDC in Section 2.3, it follows that if the momentum mismatch $\Delta\beta$ or $\Delta k = 0$, then $\text{sinc}^2\left(\frac{\Delta kL}{2}\right) = 1$ and the SFG, SHG, or SPDC intensity will increase quadratically with the crystal length L (Figure 2.2). The condition that $\Delta k = 0$ is known as perfect phase matching. In practice, it is difficult or impossible to achieve perfect phase matching due to chromatic dispersion, so most nonlinear processes will have a nonzero Δk. If Δk is nonzero, then the nonlinear signal will eventually be generated out of phase and destructively interfere, resulting in very low efficiencies and generation powers.

In birefringent crystals, the restriction of perfect phase matching can be avoided by tailoring the polarization of the input and output fields, which is known as birefringent phase matching (BPM). In BPM, the difference in refractive index as well as the wavelength dependence of the extraordinary and ordinary polarizations are utilized to achieve phase matching. Although the conditions to achieve birefringent phase matching are not as stringent as perfect phase matching, BPM still requires careful control over the refractive indices at each wavelength of interest, and the generated signal is often controlled through angle tuning or temperature tuning of the crystal. Since BPM depends on the inherent material birefringence and dispersion, BPM can be restrictive in terms of which wavelengths can be phase matched. Furthermore, the use of different polarizations in BPM means that phase matching of all three fields with the same polarization cannot be achieved.

An alternative approach to achieve phase matching is to periodically modulate the properties of the nonlinear crystal to create an additional phase factor. This approach to phase matching is known as quasi-phase matching (QPM) [9]. One way to achieve QPM is through periodic poling, in which the sign of the nonlinear susceptibility is periodically modulated in a ferroelectric crystal through inversion of the crystal structure. To quantify the effects of QPM, the spatially-varying nonlinear coefficient $d(z)$ can be described as a Fourier series:

$$d(z) = d_{\text{eff}} \sum_m c_m e^{im\left(\frac{2\pi}{\Lambda}\right)z} \tag{2.53}$$

where c_m are the Fourier coefficients, m is the order of the interaction, and Λ is the period of the modulation. Replacing d_{eff} with $d(z)$ starting from Equation 2.11, we can obtain an expression equivalent to Equation 2.26:

$$\text{P}_3 = \frac{2(c_m d_{\text{eff}})^2 \omega_3^2 L^2}{n_1 n_2 n_3 \varepsilon_0 c^3 A_{\text{eff}}} \text{P}_1 \text{P}_2 \text{sinc}^2\left(\frac{(\Delta k - \frac{2\pi m}{\Lambda})L}{2}\right) \tag{2.54}$$

where only one term in the summation over m is assumed to significantly contribute to bringing the quantity $(\Delta k - \frac{2\pi m}{\Lambda})$ close to zero. The momentum mismatch for QPM can also be redefined:

$$\Delta k_{\mathrm{QPM}} = k_3 - k_1 - k_2 - \frac{2\pi m}{\Lambda} \tag{2.55}$$

and an equivalent expression for $\Delta\beta_{\mathrm{QPM}}$ in waveguides can be defined. For periodic poling, which is equivalent to a square wave modulation from d_{eff} to $-d_{\mathrm{eff}}$ with a periodicity Λ and modulation duty cycle D, the Fourier coefficients c_m can also be solved. The effective nonlinear coefficient is then modified as:

$$d_{\mathrm{QPM}} = d_{\mathrm{eff}} \frac{2\sin(m\pi D)}{m\pi}. \tag{2.56}$$

We can see that the largest nonlinear coefficient would be for first-order quasi-phase matching ($m = 1$), which would correspond to $d_{\mathrm{QPM}} = \frac{2}{\pi} d_{\mathrm{eff}}$. Therefore, compared to perfect or birefringent phase matching, the nonlinear coefficient for first order QPM is reduced by a factor of $\frac{2}{\pi}$, and the efficiency and generated power is similarly reduced by a factor of $\frac{4}{\pi^2}$ (Figure 2.2). For higher order quasi-phase matching, there is an additional penalty to the effective nonlinearity by a factor of $\frac{1}{m}$.

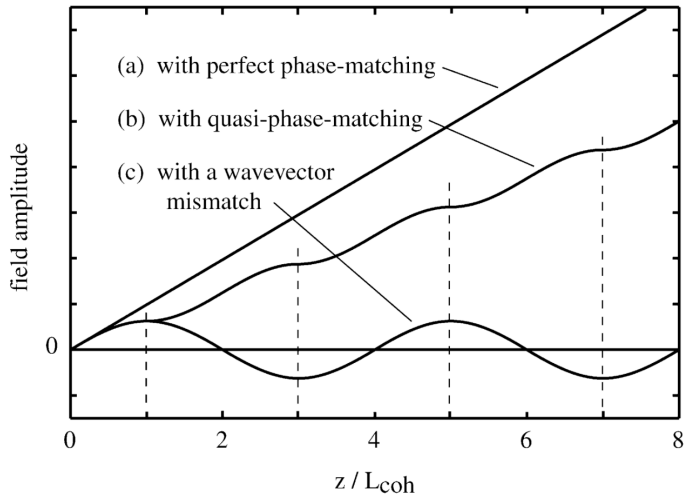

Figure 2.2: Comparison of the field amplitude of second order nonlinear processes with a) perfect phase matching, b) quasi-phase matching, and c) no phase matching with propagation along the z axis, where the coherence length $\mathrm{L_{coh}}$ is defined as half of the poling period Λ. Note that since the axis is amplitude as opposed to power or intensity, the perfect phase matching builds up the field linearly as opposed to quadratically. Reprinted from Ref. [2] with permission from Elsevier.

Despite this reduction in the effective nonlinear coefficient, QPM enables more versatile phase matching compared to perfect or birefringent phase matching, particularly in terms of the wavelength and polarization. Because QPM utilizes the poling period Λ, which is imparted by the fabrication process (Appendix B), the additional momentum factor can be controlled independently of the bulk material properties. The phase matched wavelengths can then be precisely tailored for a particular process of interest by changing the period Λ appropriately. Furthermore, because QPM is not restricted by the polarization of the modes as with BPM, QPM enables phase matching of the three fields with the same polarization. This type of phase matching allows the diagonal elements of the nonlinear coefficient tensor to be utilized, described further in Section 2.5, which often corresponds to the largest nonlinearity and therefore highest nonlinear conversion efficiency in crystals such as lithium niobate.

2.5 Nonlinear crystals

In order for second order processes to occur, the second order nonlinear coefficients d_{ijk} must be nonzero. The elements in d_{ijk} can only be nonzero if the symmetry of the propagation medium lacks an inversion center, so the medium must be a noncentrosymmetric crystal.

To demonstrate why the lack of inversion symmetry is a requirement for second order nonlinear processes, we can consider the second order polarization $\mathbf{P}^{(2)}$ from Equation 2.7. If the sign of the electric field is inverted, then we will obtain an identical expression for the polarization:

$$\begin{aligned} \mathbf{P}^{(2)} &= \sum_{i,j,k=x,y,z} 2\varepsilon_0 d_{ijk}(-E_j)(-E_k) \\ &= \sum_{i,j,k=x,y,z} 2\varepsilon_0 d_{ijk} E_j E_k / \end{aligned} \tag{2.57}$$

Now we can consider a centrosymmetric crystal. From Neumann's principle, the physical properties of a crystal must be invariant to the symmetry elements of the point group of the crystal structure[3]. By definition, centrosymmetric crystals have an inversion center. After an inversion element is applied to the centrosymmetric crystal, the signs of $\mathbf{P}^{(2)}$, E_j, and E_k must all change sign based on the original coordinate system. Therefore:

$$-\mathbf{P}^{(2)} = \sum_{i,j,k=x,y,z} 2\varepsilon_0 d_{ijk}(-E_j)(-E_k). \tag{2.58}$$

However, given the expression from Equation 2.57, the only way that Equation 2.58 can be true is if $d_{ijk} = 0$. Therefore, the second order nonlinear coefficients are all zero for centrosymmetric crystals [1]. It follows that noncentrosymmetry is a requirement for second order optical processes. Lack of an inversion center is also a requirement for a variety of other material properties and effects, including the electro-optic effect, piezoelectricity, pyroelectricity, and ferroelectricity.

In Equation 2.7, the d_{ijk} coefficients are a rank 3 tensor with 27 distinct elements. However, the subscripts j and k were introduced for notation, so swapping j and k should produce the same physical result. Assuming that d_{ijk} is symmetric upon exchange of the j and k indices and that the nonlinear susceptibility does not have significant dispersion, the following contracted notation for the nonlinear coefficient can be introduced:

$$d_{il} = \begin{bmatrix} d_{11} & d_{12} & d_{13} & d_{14} & d_{15} & d_{16} \\ d_{21} & d_{22} & d_{23} & d_{24} & d_{25} & d_{26} \\ d_{31} & d_{32} & d_{33} & d_{34} & d_{35} & d_{36} \end{bmatrix} \tag{2.59}$$

where the jk subscripts have been mapped to a new subscript l:

$$\begin{array}{rcccccc} jk: & 11 & 22 & 33 & 23, 32 & 13, 31 & 12, 21 \\ & xx & yy & zz & yz, zy & xz, zx & xy, yx \\ l: & 1 & 2 & 3 & 4 & 5 & 6 \end{array} \tag{2.60}$$

In terms of second harmonic generation, the polarization, contracted nonlinear coefficients, and electric field contributions from Equation 2.7 can then be written in matrix form as:

$$\begin{bmatrix} P_x^{(2\omega)} \\ P_y^{(2\omega)} \\ P_z^{(2\omega)} \end{bmatrix} = 2\varepsilon_0 \begin{bmatrix} d_{11} & d_{12} & d_{13} & d_{14} & d_{15} & d_{16} \\ d_{21} & d_{22} & d_{23} & d_{24} & d_{25} & d_{26} \\ d_{31} & d_{32} & d_{33} & d_{34} & d_{35} & d_{36} \end{bmatrix} \begin{bmatrix} E_x^{(\omega)} E_x^{(\omega)} \\ E_y^{(\omega)} E_y^{(\omega)} \\ E_z^{(\omega)} E_z^{(\omega)} \\ 2E_y^{(\omega)} E_z^{(\omega)} \\ 2E_x^{(\omega)} E_z^{(\omega)} \\ 2E_x^{(\omega)} E_y^{(\omega)} \end{bmatrix} \tag{2.61}$$

In this way, the original 27 distinct elements of the rank 3 tensor can be reduced to 18 elements. The number of elements can be further reduced depending on the symmetry of the nonlinear crystal.

Commonly used nonlinear crystals for applications in the visible and near-infrared wavelengths include β-barium borate (BBO, BaB_2O_4), potassium titanyl phosphate

(KTP, $KTiOPO_4$), potassium dihydrogen phosphate (KDP, KH_2PO_4), lithium triborate (LBO, LiB_3O_5), tantalum pentoxide (Ta_2O_5), lithium niobate (LN, $LiNbO_3$), and lithium tantalate (LT, $LiTaO_3$). The devices in the following chapters are all fabricated from lithium niobate.

Lithium Niobate

Lithium niobate (LN, $LiNbO_3$) is a nonlinear crystal with a wide range of advantageous properties. It is a negative uniaxial crystal with a trigonal crystal structure (Figure 2.3). Lithium niobate belongs to the $3m$ point group, which reduces the number of elements in the nonlinear coefficient matrix (Equation 2.59) to:

$$d_{il,3m} = \begin{bmatrix} 0 & 0 & 0 & 0 & d_{31} & -d_{22} \\ -d_{22} & d_{22} & 0 & d_{31} & 0 & 0 \\ d_{31} & d_{31} & d_{33} & 0 & 0 & 0 \end{bmatrix} \tag{2.62}$$

where $d_{22} = 2.1$ pm/V, $d_{31} = -4.35$ pm/V, and $d_{33} = -27.2$ pm/V for the congruently melting composition of lithium niobate ([Li]/[Nb] = 0.946, Figure 2.4) measured at 1060 nm [11–13].

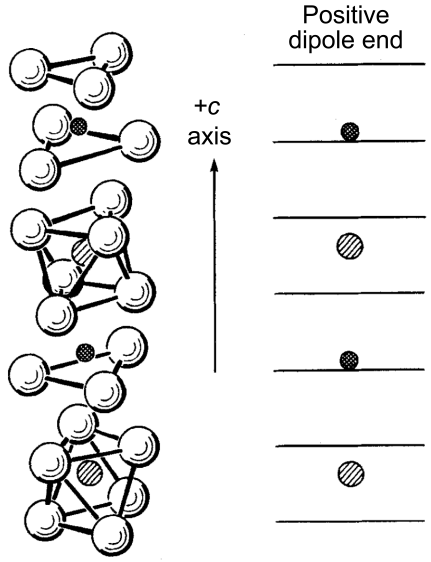

Figure 2.3: Crystal structure of lithium niobate with the polarization direction indicated along the $+c$ axis. Black circles represent the lithium ions, gray circles represent the niobium ions, and white circles represent the oxygen ions. Horizontal lines on the right diagram indicate the oxygen layers. Reproduced from Ref. [10] with permission from SNCSC.

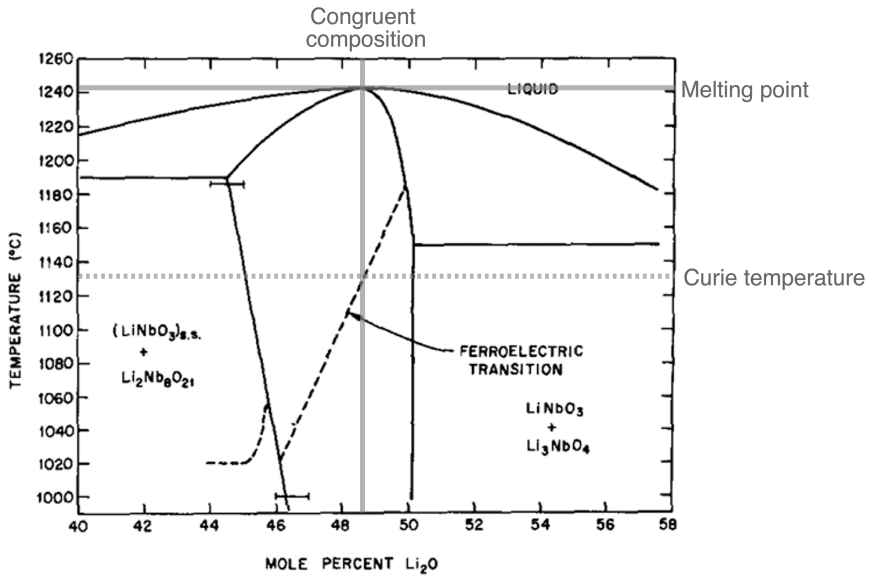

Figure 2.4: Phase diagram of undoped lithium niobate. The congruent composition of lithium niobate (solid, vertical) and associated melting (solid, horizontal) and Curie (dashed, horizontal) temperatures are indicated with gray lines. Reprinted from Ref. [14] with the permission of AIP Publishing.

In addition to its high optical nonlinearity, lithium niobate is also a ferroelectric crystal. Ferroelectric materials have a spontaneous electric polarization that can be reversed upon application of a strong electric field, known as the coercive field. Congruent undoped lithium niobate has a coercive field of approximately 20 kV/mm [15]. The ferroelectric properties of lithium niobate enable quasi-phase matching through periodic poling, discussed in Section 2.4. In ferroelectric crystals, the Curie temperature is the temperature at which the crystal loses its electric polarization, analogous to the Curie temperature in ferromagnetic materials. The Curie temperature of congruent LN is approximately 1130°C [14], which is close to its melting point of 1240°C as shown in Figure 2.4. The high Curie temperature ensures that periodically poled lithium niobate can be utilized at elevated temperatures.

Lithium niobate can also be doped with magnesium oxide (MgO) to reduce optical damage [16], particularly at shorter ultraviolet and visible wavelengths generated in Chapters 3 and 4. MgO doping also reduces the coercive field for ferroelectric poling to approximately 4 kV/mm [15, 17]. The nonlinear coefficients of 5% MgO-doped congruent lithium niobate have been measured as $|d_{31}| = 4.9$ pm/V and $|d_{33}| = 28.4$ pm/V at 852 nm [18].

For nonlinear optical processes, the transparency range and refractive indices of

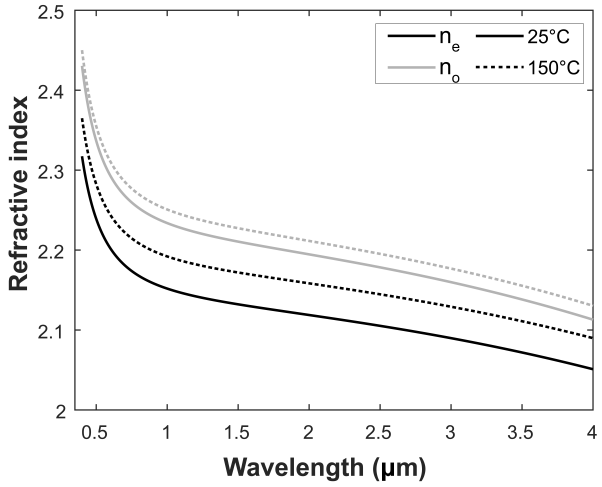

Figure 2.5: Extraordinary (black) and ordinary (gray) refractive indices of bulk 5% MgO-doped lithium niobate at room temperature (solid) and 150°C (dashed) using the Sellmeier equations from Ref. [19].

nonlinear crystals are integral for frequency generation. Lithium niobate has a wide transparency range from the ultraviolet at 326 nm [20] out to the mid-IR around 5 μm [21]. The refractive indices for 5% MgO-doped bulk crystal lithium niobate are plotted in Figure 2.5. LN's refractive indices of ~2.3 for the ordinary index and ~2.1 for the extraordinary index are considerably higher than the indices of air ($n = 1$) or materials such as SiO_2 ($n = 1.44$). This high refractive index of LN relative to these materials provides index contrast and therefore enables waveguiding through total internal reflection. Waveguides increase the efficiency of nonlinear processes through tight modal confinement to increase the effective nonlinear interaction area and also enable dense integration through small bend radii. From bulk LN single crystals, which are typically grown through the Czochralski technique, large-area waveguides can be fabricated through micromachining or ion diffusion. Although these large-area waveguides do enhance the nonlinear conversion efficiency, their cross sections are typically on the order of 10 μm^2, resulting in multimode propagation. Furthermore, with ion diffusion, the index contrast is typically low ($\Delta n \approx 0.1$), producing only weak modal confinement in the waveguide region and prohibiting the tight bend radii needed for dense photonic integration [22].

An alternative approach to fabricating waveguides was implemented through the integration of ion-cut or "smart cut" technology, which previously enabled the

silicon-on-insulator (SOI) platform. Through these ion slicing techniques, sub-μm thin films of lithium niobate can be bonded to a low-index insulator layer, typically SiO_2, with a bulk crystal substrate for stability and ease of handling [23]. This thin film platform is known as thin-film lithium niobate (TFLN) or lithium-niobate-on-insulator (LNOI) as a parallel to SOI. Through dry etching techniques, tightly confining waveguides with sub-μm^2 cross sections can be fabricated [24]. With such small effective areas and high index contrast, these tightly confining or nanophotonic waveguides on TFLN are capable of enhanced nonlinear efficiencies and dense integration, thus realizing the full potential of LN for photonic integrated circuits (PICs).

References

[1] A. Yariv, P. Yeh, *Photonics: Optical Electronics in Modern Communications*, 6. edition, Oxford University Press, New York, NY, **2007**, 836 pp.

[2] R. W. Boyd, *Nonlinear Optics*, 3rd ed, Academic Press, Amsterdam ; Boston, **2008**, 613 pp.

[3] M. Fox, *Optical Properties of Solids*, Second edition, reprinted (with corrections), Oxford University Press, Oxford New York, NY, **2011**, 396 pp.

[4] M. Jankowski, C. Langrock, B. Desiatov, A. Marandi, C. Wang, M. Zhang, C. R. Phillips, M. Lončar, M. M. Fejer, *Optica* **2020**, *7*, 40.

[5] C. Wang, C. Langrock, A. Marandi, M. Jankowski, M. Zhang, B. Desiatov, M. M. Fejer, M. Lončar, *Optica* **2018**, *5*, 1438.

[6] M. Fiorentino, S. M. Spillane, R. G. Beausoleil, T. D. Roberts, P. Battle, M. W. Munro, *Optics Express* **2007**, *15*, 7479.

[7] D. Walls, G. J. Milburn, *Quantum Optics*, Springer Berlin Heidelberg, Berlin, Heidelberg, **2008**.

[8] K. Koch, E. Cheung, G. Moore, S. Chakmakjian, J. Liu, *IEEE Journal of Quantum Electronics* **1995**, *31*, 769–781.

[9] D. S. Hum, M. M. Fejer, *Comptes Rendus Physique* **2006**, *8*, 180–198.

[10] R. S. Weis, T. K. Gaylord, *Applied Physics A* **1985**, *37*, 191–203.

[11] D. Roberts, *IEEE Journal of Quantum Electronics* **1992**, *28*, 2057–2074.

[12] R. C. Miller, W. A. Nordland, P. M. Bridenbaugh, *Journal of Applied Physics* **1971**, *42*, 4145–4147.

[13] V. G. Dmitriev, G. G. Gurzadyan, D. N. Nikogosyan, *Handbook of Nonlinear Optical Crystals*, red. by H. K. V. Lotsch, Springer Berlin Heidelberg, Berlin, Heidelberg, **1997**.

[14] J. R. Carruthers, G. E. Peterson, M. Grasso, P. M. Bridenbaugh, *Journal of Applied Physics* **1971**, *42*, 1846–1851.

[15] A. Kuroda, S. Kurimura, Y. Uesu, *Applied Physics Letters* **1996**, *69*, 1565–1567.

[16] N. Iyi, K. Kitamura, Y. Yajima, S. Kimura, Y. Furukawa, M. Sato, *Journal of Solid State Chemistry* **1995**, *118*, 148–152.

[17] K. Mizuuchi, A. Morikawa, T. Sugita, K. Yamamoto, *Journal of Applied Physics* **2004**, *96*, 6585–6590.

[18] I. Shoji, T. Kondo, A. Kitamoto, M. Shirane, R. Ito, *Journal of the Optical Society of America B* **1997**, *14*, 2268.

[19] O. Gayer, Z. Sacks, E. Galun, A. Arie, *Applied Physics B* **2008**, *91*, 343–348.

[20] A. Zanatta, *Results in Physics* **2022**, *39*, 105736.

[21] D. E. Zelmon, D. L. Small, D. Jundt, *Journal of the Optical Society of America B* **1997**, *14*, 3319.

[22] Y. Jia, L. Wang, F. Chen, *Applied Physics Reviews* **2021**, *8*, 011307.

[23] P. Rabiei, P. Gunter, *Applied Physics Letters* **2004**, *85*, 4603–4605.

[24] H. Hu, R. Ricken, W. Sohler, *Optics Express* **2009**, *17*, 24261–24268.

Chapter 3

ULTRAVIOLET SECOND HARMONIC GENERATION

On-chip ultraviolet (UV) sources are of great interest for building compact and scalable atomic clocks, quantum computers, and spectrometers. However, few material platforms are suitable for integrated UV light generation and manipulation. Of these materials, thin-film lithium niobate offers unique advantages such as submicron modal confinement, strong nonlinearity, and quasi-phase matching. Despite these characteristics, its utilization in the UV has remained elusive because of the substantial sensitivity of standard quasi-phase matching to fabrication imperfections, the photorefractive effect, and relatively large losses in this range. Here, we present efficient (197 ± 5 %/W/cm^2) second harmonic generation of UV-A light in a periodically poled lithium niobate nanophotonic waveguide. We achieve on-chip UV powers of 30 μW and linear wavelength tunability using temperature. These results are enabled with large cross section waveguides, which leads to first-order UV quasi-phase-matching with relatively long poling periods (>1.5 μm). By varying the poling period, we have achieved the shortest reported wavelength (355 nm) generated through frequency doubling in thin-film lithium niobate to date. Our results open up new avenues for UV on-chip sources and chip-scale photonics through compact frequency-doubling of common near-IR laser diodes.

Most of this chapter has been adapted with permission from:
E. Hwang, N. Harper, R. Sekine, L. Ledezma, A. Marandi, S. Cushing, *Optics Letters* **2023**, *48*, 3917

3.1 Introduction

The field of integrated nonlinear optics has grown dramatically during the past decade due to the development and commercial availability of thin-film lithium niobate [1, 2]. In passive nonlinear devices, thin-film lithium niobate (TFLN) excels in efficient frequency conversion and quantum state generation from the visible to the infrared (IR) [3, 4]. The strong mode confinement of single-pass, low-loss [5] nanophotonic waveguides and quasi-phase matched interactions utilizing lithium niobate's largest second-order nonlinear optical tensor element have resulted in record-breaking efficiencies in applications such as second harmonic generation (SHG) [6, 7], supercontinuum generation [8], difference frequency generation [9],

parametric amplification [10], and parametric downconversion [11]. Similarly, TFLN active devices such as modulators [12], electro-optic frequency combs [13], and femtosecond pulse generators [14] show impressive performance in compact form-factors due to lithium niobate's large electro-optic tensor elements. However, there is still significant room for lithium niobate's use in UV photonics [15], with applications such as UV-visible spectroscopy, optogenetics, high-resolution microscopy, security banknote features, laser cooling [16], atomic clocks [17], and quantum computing [18].

Although lithium niobate has been extensively studied in the IR, and comparatively less so in the visible, UV devices have remained rare to date. The few reported lithium niobate devices for UV generation have been limited to metasurfaces [19], nanoparticles [20], and large micromachined or channel waveguides [21, 22], and therefore do not take advantage of the sub-micron mode confinement and efficiency of lithium niobate in a nanophotonic platform. TFLN has yet to be well studied in the UV due to significant quasi-phase matching sensitivity to fabrication errors, the ultra-short poling periods required to overcome the high dispersion in waveguides at short wavelengths, and material and scattering loss. Variations in the thin film thickness of even 1 Å are sufficient to disrupt phase matching in visible SHG, limiting the effective interaction length and chip-to-chip repeatability [1, 23]. UV generation should be possible up to lithium niobate's band gap at ~330 nm (3.8 eV) [24], but an exponentially decaying Urbach absorption tail persists towards the visible due to defects in the crystal structure [25], and impurity ion (Cu^{+}, Fe^{2+}) resonances can cause additional loss [26, 27]. Furthermore, losses at the waveguide sidewalls also increase at shorter wavelengths due to surface imperfection Rayleigh scattering, which scales as λ^{-4} [28]. In spite of these difficulties, there is much to gain by extending the spectral coverage of TFLN frequency conversion to the UV. Notably, near-IR laser diodes, which can be frequency doubled, are considerably more accessible than UV laser diodes and gas lasers [29]. Among other nanophotonic material platforms, only aluminum nitride (AlN) has been significantly investigated for waveguided second harmonic UV generation, despite AlN lacking ferroelectricity and therefore being incapable of periodic poling. The lateral polar structures used to achieve quasi-phase matching in AlN are highly scattering, resulting in much lower conversion efficiencies (<1%) [30] compared to lithium niobate devices. Other potential UV platforms (lithium tantalate [31], BBO [32], LBGO [33]) have yet to be thoroughly explored in a thin film nanophotonic platform. Lithium niobate remains superior to these materials with its combination of low-loss waveguides, high second-order

nonlinear response, ferroelectric poling for quasi-phase matching, and, for the case of thin-film lithium tantalate, commercial accessibility [34].

In this chapter, we produce 30 μW of efficient (197 ± 5 %/W/cm^2) second harmonic generation of UV light (386.5 nm) with periodically poled lithium niobate (PPLN) rib waveguides (Figure 3.1a). The devices exhibit wavelength tunability through temperature and poling period, and are capable of UV SHG at the lowest wavelengths tested (710 nm frequency-doubled to 355 nm).

3.2 Device design and fabrication

The waveguide geometry was designed to reduce sensitivity to the TFLN thickness without compromising the SHG bandwidth at the center wavelength of the laser used in this paper (773 nm). To quantify the phase matching sensitivity, the guided modes were simulated (Lumerical MODE) using the bulk Sellmeier coefficients of lithium niobate [35] and silicon dioxide [36] with the geometric parameters shown in Figure 3.1b and a 60° sidewall, which is consistent with the fabrication process. Only the fundamental quasi-transverse electric (TE) modes of the first harmonic (FH) and second harmonic (SH) (Figure 3.1b) were considered since they access lithium niobate's largest nonlinear tensor element (d_{33} = 28 pm/V)[37]. Thicker waveguides (600 nm film thickness) were analyzed because they allow for reduced sensitivity to thickness errors and longer poling periods with a tradeoff of reduced efficiency and increased susceptibility to slab leakage. The first-order wavelength sensitivity and SHG bandwidth were calculated using a numerical first derivative with respect to film thickness. A 600 nm film demonstrated a significant reduction in thickness sensitivity over a 200 nm film for nearly all waveguide geometry variations (Figure 3.1c). An etch depth of 375 nm and top width of 1.5 μm (Figure 3.1d-e) were targeted to ensure operation within the flat region of the sensitivity plot. For these parameters, the wavelength sensitivity to film thickness is $\frac{d\lambda}{dT}$ = 0.08 nm/nm with a 3.4 pm SHG bandwidth, and the effective refractive indices ($n_{\text{eff,SH}}$ = 2.32, $n_{\text{eff,FH}}$ = 2.10) result in a quasi-phase matching poling period of $\Lambda = \lambda_{\text{SH}}/\Delta n_{\text{eff}}$ = 1.8 μm (Figure 3.1f). The larger cross section of the 600 nm film thickness allows for this relatively long poling period, in comparison to a 1.1 μm period for a 200 nm film with the same aspect ratio and wavelength.

The devices were fabricated from a 5% MgO-doped X-cut thin-film lithium niobate on insulator wafer (NanoLN), which consists of 600 nm of lithium niobate bonded to 2 μm of silicon dioxide on a 0.4 mm silicon substrate. Periodically poled

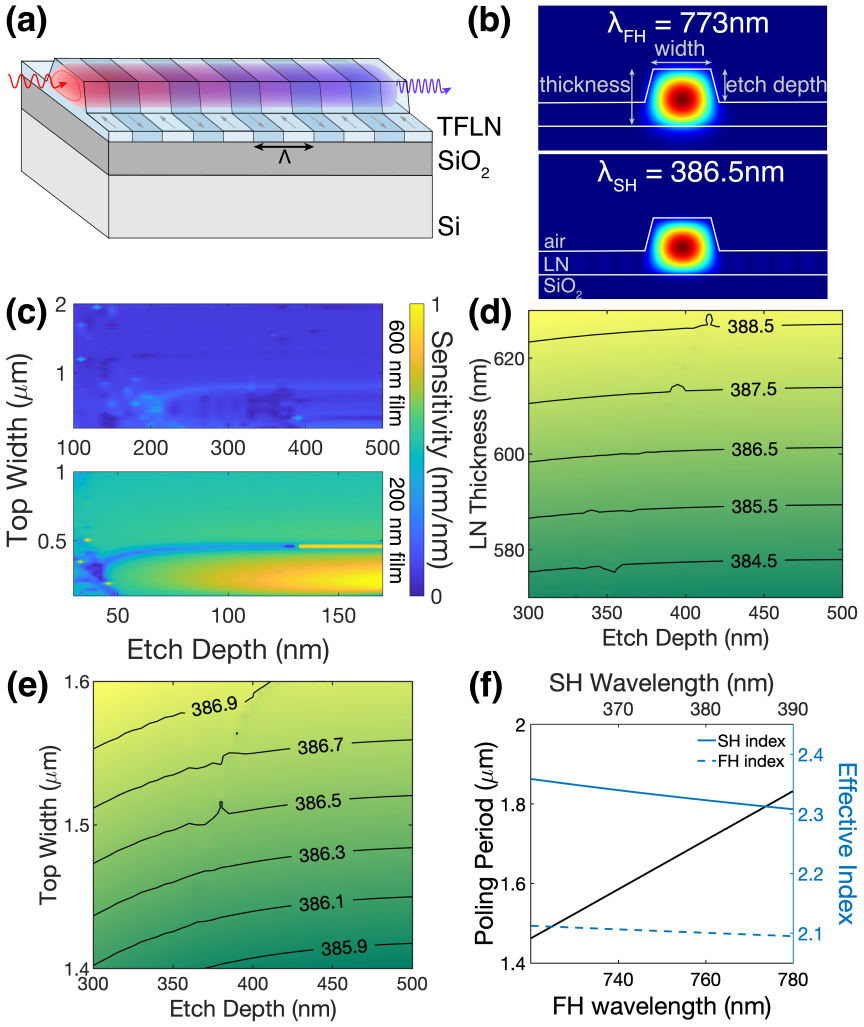

Figure 3.1: Schematic and design of the periodically poled LN waveguide used for ultraviolet SHG. (a) Schematic of the PPLN waveguide. (b) Mode profiles of the fundamental TE mode at the first and second harmonics. (c) Sensitivity of the SHG center wavelength to the thin film thickness as a function of the waveguide geometry for 600 nm (top) and 200 nm (bottom) thin film thicknesses; local areas that minimize the sensitivity also decrease the phase matching bandwidth. Two dimensional sweeps of the (d) film thickness and etch depth and (e) top width and etch depth to vary the SHG center wavelength (contour lines). Note that perturbations in the contour lines are caused by mode crossings. (f) Poling period and effective refractive indices of the first and second harmonic fundamental TE modes as a function of wavelength.

waveguides were fabricated following Ref. [10]. Each waveguide had a 7 mm poled length, with poling periods ranging from 1.35 to 2 μm. The waveguide etch depth and sidewall angle were verified through atomic force microscopy, and the poled domain formation was measured with second harmonic microscopy [38].

3.3 Results

The SHG from the PPLN devices was characterized using an optical setup depicted in Figure 3.2a. The output from a tunable continuous-wave (CW) single-frequency laser (Velocity TLD-6712, 765-781 nm) passed through an optical isolator and a variable neutral density filter to adjust the input power. An achromatic half-wave plate (Thorlabs AHWP10M-980) aligned the input polarization to the optical axis of the chip to maximize SHG power. The first harmonic was coupled to the waveguide using an aspheric lens (Thorlabs C140TMD-B). The waveguide output was collimated by another aspheric lens (Thorlabs C140TMD-A) and collected by a high-OH multimode fiber (Thorlabs M122L01). The device output was monitored using an optical spectrum analyzer (Yokogawa AQ6374) with a passband bandwidth of 5 nm around the second harmonic center wavelength to remove residual first harmonic.

The temperature and poling period dependence of the phase matched wavelength is plotted in Figure 3.2c and 3.2d, respectively. To measure the temperature dependence, a nonlinear crystal oven (HC Photonics TC038-PC) heated the PPLN waveguides from 20 to 100°C. The least squares slope (34 ± 2 pm/°C) matches the theoretically calculated value of 32 pm/°C. By varying the poling period, we also obtained SHG spectra extending down to 355 nm. A tunable CW Ti:Sapphire oscillator (Spectra-Physics Tsunami, 700-1100 nm) was used in a similar scheme to Figure 3.2a to measure the SHG from several PPLN waveguides with poling periods as short as 1.35 μm (Figure 3.2d). The fitted slope of the SHG center wavelength with the poling period (79.6 ± 0.2 nm/μm) is in close agreement with the theoretical slope of 81.1 nm/μm. This agreement in both the temperature and poling period demonstrate that the given Sellmeier coefficients [35] predict the temperature dependence and group velocity mismatch of lithium niobate in the UV relatively well, despite the limited refractive index data at shorter wavelengths. Unlike the initial measurements using the single-frequency laser, accurate efficiency data could not be extracted because the Ti:Sapphire oscillator linewidth (0.3 nm) is orders of magnitude larger than the phase matching bandwidth (3.4 pm). However, these spectra demonstrate that SHG is possible even closer to the 326 nm band gap of lithium

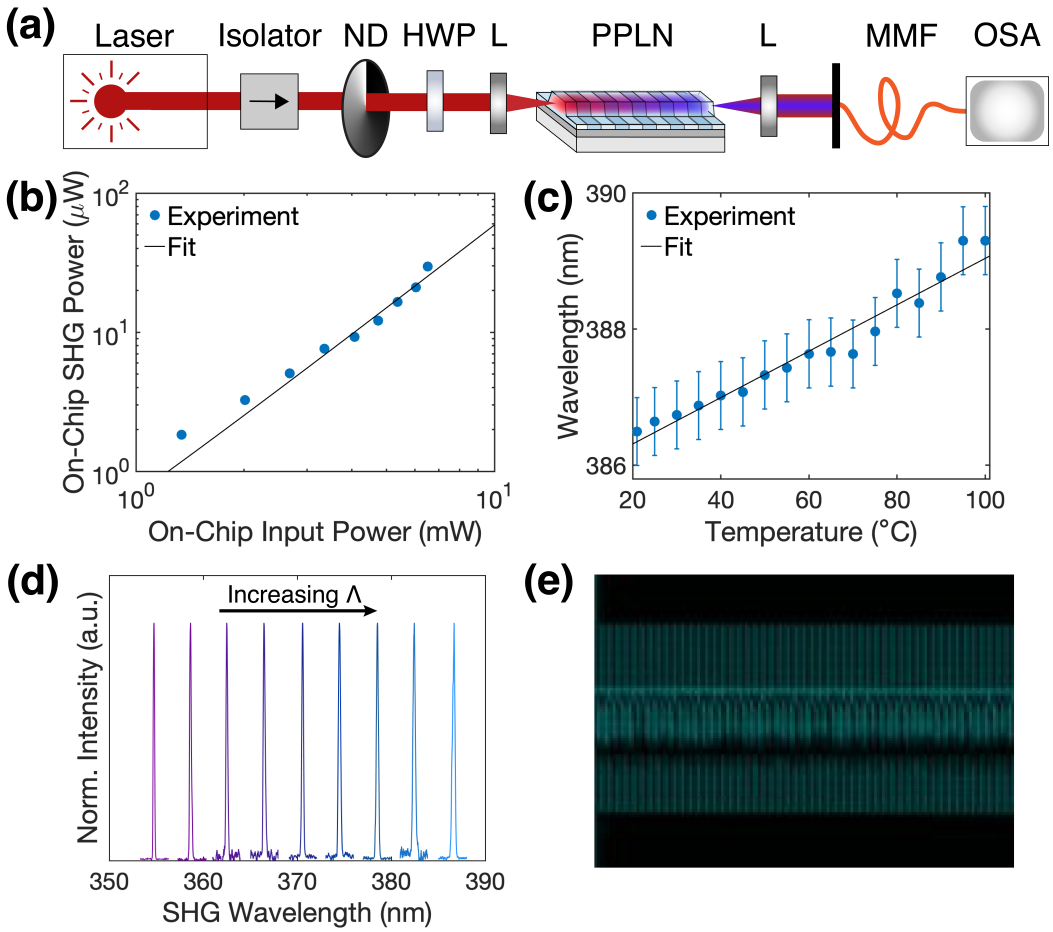

Figure 3.2: Characterization setup and results of the LN waveguide for SHG. (a) Optical setup for on-chip SHG characterization. ND, variable neutral density filter; HWP, half wave plate; L, aspheric lens; MMF, multi-mode fiber; OSA, optical spectrum analyzer. (b) On-chip SHG output power measured as a function of the on-chip input power with experimental fit to calculate the efficiency. (c) Temperature tuning of the SHG center wavelength, measured as the weighted average of the spectrum with standard deviations and experimental fit. (d) Normalized spectra of the poling period swept from 1.35 to 1.75 μm in 50 nm increments. (e) Second harmonic microscopy image of the periodically poled region.

niobate than what has previously been demonstrated, and that the thin film lithium niobate platform is able to phase match the full range of a Ti:Sapphire laser.

Although the SHG wavelength tunability agrees well with theory, the experimental efficiency of 197 ± 5 %/W/cm^2 measured from the single-frequency laser at 773.1 nm is lower than the calculated ideal theoretical efficiency [7] of 18,100 %/W/cm^2. An immediate explanation is the poling quality of this device, which exhibited significant domain widening due to the short poling period. The duty cycle is estimated to

be 90% from second harmonic microscopy images (Figure 3.2e), which lowers the theoretical efficiency to 1810 %/W/cm^2. Additional discrepancies can be explained by lateral leakage from the waveguide mode to the slab mode, second harmonic propagation loss, and asymmetry in the input and output coupling efficiency.

The experimental SHG spectrum (Figure 3.3a) was measured by sweeping the first harmonic wavelength from 771 to 775 nm at a constant 30 mW input power. The spectrum exhibits multiple peaks over a 0.5 nm bandwidth, deviating from the theoretical sinc^2 line shape and 3.4 pm full-width at half maximum bandwidth. The discrepancies in the efficiency, bandwidth, and spectral shape are likely caused by multimode effects, index variations, or poling variations. Although the waveguides in this work support multiple modes due to the large cross sections, the fundamental modes of the first and second harmonic are solely responsible for the phase matching of the UV generation due to large momentum mismatches or poor modal overlap of the higher order modes. Furthermore, collecting the second harmonic with a single-mode fiber (Thorlabs P1-305A-FC-1) does not change the shape of the transfer function, which is expected to occur if higher-order modes were present. Potential sources of index changes are thickness variations, thermal gradients, induced absorption, or photorefraction, while poling defects could be caused by stitching errors in the lithography process. Without a straightforward method of distinguishing these possibilities, we chose to focus on index variations and assume that the poling is uniform. Index variations preserve the integral of the SHG transfer function, which allows us to determine the contribution of the index variations to the experimentally lower efficiency. An integral of the spectral efficiency yields an area of 31.8 %/W/cm^2·nm, and the transfer function with the same area and no index variations has a peak efficiency of 861 %/W/cm^2.

The magnitude and position of the index variations cannot be directly calculated without knowledge of the SHG phase relative to the first harmonic. However, the magnitude of the index variations can be estimated by approximating the phase mismatch error as a cubic polynomial to fit the SHG spectrum, given by the following expression for $\eta(\omega)$[39], which assumes a 50% duty cycle and constant poling period:

$$\eta(\omega) = \left| \int_0^L \exp\left(i \int_0^z (\delta\beta(\xi) + \delta\beta(\omega))\, d\xi \right) dz \right|^2 . \tag{3.1}$$

The coefficients of the phase mismatch error $\delta\beta(z)$ are estimated by minimizing the squared residuals between the predicted and experimental spectra using a particle swarm optimization algorithm followed by a gradient descent[40], which yields the

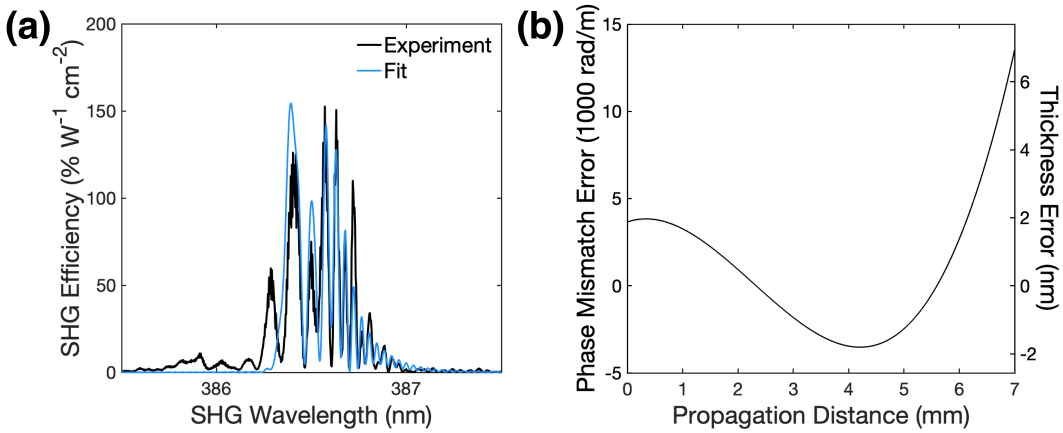

Figure 3.3: SHG spectra and fitted thickness profile of the LN waveguide for UV SHG. (a) Experimental and index variation-fitted (Equation 3.1) SHG spectra. (b) Phase mismatch error represented by Equation 3.2 and corresponding thickness error against propagation distance.

following expression for $\delta\beta(z)$ (Figure 3.3b):

$$\delta\beta(z) = 0.0636z^3 - 0.578z^2 + 0.544z + 3.66 \tag{3.2}$$

where the phase mismatch error $\delta\beta$ is in units of rad/m and the propagation distance z is in µm. A thickness error of ±5 nm throughout the waveguide explains the full spread in the experimental spectrum. A discrepancy of this magnitude is reasonable given commercial film thickness tolerances; however, this error is an upper estimate given that the index variations could be a combination of the thickness, photorefraction, UV-induced infrared absorption, and temperature gradient. Although this thickness variation could be the cause of the lowered experimental efficiency, the same amount of thickness variation in a thinner film could potentially disrupt phase matching entirely.

3.4 Conclusion and outlook

In conclusion, we have demonstrated temperature-tunable UV light generation in an integrated thin-film lithium niobate waveguide. We have measured an SHG efficiency of 197 ± 5 %/W/cm^2, with discrepancies from theory explained by the poling duty cycle and index variations. As of this publication, this is the shortest wavelength (355-386 nm) produced through second harmonic generation with CW-pumped periodically poled thin-film lithium niobate waveguides. Our work opens up opportunities to realize efficient frequency-doubled chip-scale ultraviolet laser

diodes for UV integrated photonics, with applications spanning spectroscopy, atomic physics, and quantum science.

References

[1] A. Boes, L. Chang, C. Langrock, M. Yu, M. Zhang, Q. Lin, M. Lončar, M. Fejer, J. Bowers, A. Mitchell, *Science* **2023**, *379*, eabj4396.

[2] D. Zhu, L. Shao, M. Yu, R. Cheng, B. Desiatov, C. J. Xin, Y. Hu, J. Holzgrafe, S. Ghosh, A. Shams-Ansari, E. Puma, N. Sinclair, C. Reimer, M. Zhang, M. Lončar, *Advances in Optics and Photonics* **2021**, *13*, 242.

[3] R. Nehra, R. Sekine, L. Ledezma, Q. Guo, R. M. Gray, A. Roy, A. Marandi, *Science* **2022**, *377*, 1333–1337.

[4] M. Leidinger, S. Fieberg, N. Waasem, F. Kühnemann, K. Buse, I. Breunig, *Optics Express* **2015**, *23*, 21690.

[5] A. Shams-Ansari, G. Huang, L. He, Z. Li, J. Holzgrafe, M. Jankowski, M. Churaev, P. Kharel, R. Cheng, D. Zhu, N. Sinclair, B. Desiatov, M. Zhang, T. J. Kippenberg, M. Lončar, *APL Photonics* **2022**, *7*, 081301.

[6] T. Park, H. S. Stokowski, V. Ansari, T. P. McKenna, A. Y. Hwang, M. M. Fejer, A. H. Safavi-Naeini, *Optics Letters* **2022**, *47*, 2706.

[7] M. Jankowski, C. Langrock, B. Desiatov, A. Marandi, C. Wang, M. Zhang, C. R. Phillips, M. Lončar, M. M. Fejer, *Optica* **2020**, *7*, 40.

[8] C. Wang, C. Langrock, A. Marandi, M. Jankowski, M. Zhang, B. Desiatov, M. M. Fejer, M. Lončar, *Optica* **2018**, *5*, 1438.

[9] J. Mishra, T. P. McKenna, E. Ng, H. S. Stokowski, M. Jankowski, C. Langrock, D. Heydari, H. Mabuchi, M. M. Fejer, A. H. Safavi-Naeini, *Optica* **2021**, *8*, 921.

[10] L. Ledezma, R. Sekine, Q. Guo, R. Nehra, S. Jahani, A. Marandi, *Optica* **2022**, *9*, 303.

[11] J. Zhao, C. Ma, M. Rüsing, S. Mookherjea, *Physical Review Letters* **2020**, *124*, 163603.

[12] C. Wang, M. Zhang, X. Chen, M. Bertrand, A. Shams-Ansari, S. Chandrasekhar, P. Winzer, M. Lončar, *Nature* **2018**, *562*, 101–104.

[13] M. Zhang, B. Buscaino, C. Wang, A. Shams-Ansari, C. Reimer, R. Zhu, J. M. Kahn, M. Lončar, *Nature* **2019**, *568*, 373–377.

[14] M. Yu, D. Barton III, R. Cheng, C. Reimer, P. Kharel, L. He, L. Shao, D. Zhu, Y. Hu, H. R. Grant, L. Johansson, Y. Okawachi, A. L. Gaeta, M. Zhang, M. Lončar, *Nature* **2022**, *612*, 252–258.

[15] M. Soltani, R. Soref, T. Palacios, D. Englund, *Optics Express* **2016**, *24*, 25415.

[16] K. Toyoda, A. Miura, S. Urabe, K. Hayasaka, M. Watanabe, *Optics Letters* **2001**, *26*, 1897.

[17] A. D. Ludlow, M. M. Boyd, J. Ye, E. Peik, P. O. Schmidt, *Reviews of Modern Physics* **2015**, *87*, 637–701.

[18] M. Saffman, *Journal of Physics B: Atomic Molecular and Optical Physics* **2016**, *49*, 202001.

[19] J. Ma, F. Xie, W. Chen, J. Chen, W. Wu, W. Liu, Y. Chen, W. Cai, M. Ren, J. Xu, *Laser & Photonics Reviews* **2021**, *15*, 2000521.

[20] F. Timpu, J. Sendra, C. Renaut, L. Lang, M. Timofeeva, M. T. Buscaglia, V. Buscaglia, R. Grange, *ACS Photonics* **2019**, *6*, 545–552.

[21] J. Rutledge, A. Catanese, D. D. Hickstein, S. A. Diddams, T. K. Allison, A. S. Kowligy, *Journal of the Optical Society of America B* **2021**, *38*, 2252.

[22] T. Sugita, K. Mizuuchi, Y. Kitaoka, K. Yamamoto, *Japanese Journal of Applied Physics* **2001**, *40*, 1751.

[23] A. A. Sayem, Y. Wang, J. Lu, X. Liu, A. W. Bruch, H. X. Tang, *Applied Physics Letters* **2021**, *119*, 231104.

[24] A. Zanatta, *Results in Physics* **2022**, *39*, 105736.

[25] R. Bhatt, I. Bhaumik, S. Ganesamoorthy, A. K. Karnal, M. K. Swami, H. S. Patel, P. K. Gupta, *Physica Status Solidi (a)* **2012**, *209*, 176–180.

[26] J. R. Schwesyg, M. C. C. Kajiyama, M. Falk, D. H. Jundt, K. Buse, M. M. Fejer, *Applied Physics B* **2010**, *100*, 109–115.

[27] M. V. Ciampolillo, A. Zaltron, M. Bazzan, N. Argiolas, C. Sada, *Applied Spectroscopy* **2011**, *65*, 216–220.

[28] R. Maurer, *Proceedings of the IEEE* **1973**, *61*, 452–462.

[29] S. M. N. Hasan, W. You, M. S. I. Sumon, S. Arafin, *Photonics* **2021**, *8*, 267.

[30] D. Alden, T. Troha, R. Kirste, S. Mita, Q. Guo, A. Hoffmann, M. Zgonik, R. Collazo, Z. Sitar, *Applied Physics Letters* **2019**, *114*, 103504.

[31] J.-P. Meyn, C. Laue, R. Knappe, R. Wallenstein, M. Fejer, *Applied Physics B* **2001**, *73*, 111–114.

[32] K. Devi, S. Parsa, M. Ebrahim-Zadeh, *Optics Express* **2016**, *24*, 8763.

[33] N. Umemura, J. Hirohashi, Y. Nakahara, H. Oda, Y. Furukawa, *Optical Materials Express* **2019**, *9*, 2159.

[34] D. J. Blumenthal, *APL Photonics* **2020**, *5*, 020903.

[35] O. Gayer, Z. Sacks, E. Galun, A. Arie, *Applied Physics B* **2008**, *91*, 343–348.

[36] T. Toyoda, M. Yabe, *Journal of Physics D: Applied Physics* **1983**, *16*, L97–L100.

[37] I. Shoji, T. Kondo, A. Kitamoto, M. Shirane, R. Ito, *Journal of the Optical Society of America B* **1997**, *14*, 2268.

[38] M. Rüsing, J. Zhao, S. Mookherjea, *Journal of Applied Physics* **2019**, *126*, 114105.

[39] S. Helmfrid, G. Arvidsson, *Journal of the Optical Society of America B* **1991**, *8*, 797.

[40] MathWorks, Particle Swarm Optimization, **2014**.

Chapter 4

VISIBLE THROUGH NEAR-INFRARED SPONTANEOUS PARAMETRIC DOWNCONVERSION

Efficient on-chip entangled photon pair generation at telecom wavelengths is an integral aspect of emerging quantum optical technologies, particularly for quantum communication and computing. However, moving to shorter wavelengths enables the use of more accessible silicon detector technology and opens up applications in imaging and spectroscopy. Here, we present high brightness ($(1.6 \pm 0.3) \times 10^9$ pairs/s/mW/nm) visible through near-IR photon pair generation in a periodically poled lithium niobate nanophotonic waveguide. The degenerate spectrum of the photon pairs is centered at 811 nm with a bandwidth of 117 nm when pumped with a spectrally multimode laser diode. The measured on-chip source efficiency of $(2.3 \pm 0.5) \times 10^{11}$ pairs/s/mW is on par with source efficiencies at telecom wavelengths and is also orders of magnitude higher than the efficiencies of other visible sources implemented in bulk crystal or diffused waveguide-based technologies. Further improvements in the brightness and efficiencies are possible by pumping the device with a single-frequency laser, which would also shrink the pair bandwidth. These results represent the shortest wavelength of photon pairs generated in a nanophotonic waveguide reported to date by nearly an octave. Supplemental theory, device characterization, and raw data can be found in Appendix C.

Most of this chapter has been adapted with permission from:
N. A. Harper, E. Y. Hwang, R. Sekine, L. Ledezma, C. Perez, A. Marandi, S. K. Cushing, *Optica Quantum* **2024**, *2*, 103

4.1 Introduction

Spontaneous parametric downconversion (SPDC) has been used for decades to produce quantum entanglement in various photonic degrees of freedom, serving as a workhorse in emerging quantum optical technologies. Compared to most nonlinear processes, SPDC is relatively inefficient, requiring over one million pump photons to produce one pair of entangled photons in even the highest performing crystals. However, recent advances in nanophotonics, particularly in thin-film lithium niobate (TFLN), have enabled significantly more efficient frequency conversion and quantum state generation [1–3] through sub-μm interaction areas, high nonlinearities, and

low material losses [4, 5]. By exploiting this platform, many recent demonstrations of SPDC in TFLN [6–9] have achieved efficiencies three orders of magnitude greater than that of bulk crystal-based sources [10] and one order of magnitude greater than that of large diffused waveguide-based sources [11]. To date, most TFLN-based photon pair sources are designed for SPDC at telecom wavelengths because of the low losses in optical fibers at 1550 nm [12, 13] and back-compatibility for applications such as quantum communication [14], computing [15], and a globally connected quantum network [16].

Although telecom photons are preferred for quantum information applications, visible and near-infrared photons are generally better suited for imaging and spectroscopy. Experiments at these wavelengths can take advantage of multi-pixel detectors such as electron-multiplying charge coupled devices (EM-CCD) and single photon avalanche detector (SPAD) arrays, enabling the measurements needed for imaging [17–19] and characterization of high-dimensional entangled states [20, 21]. Furthermore, the electronic transitions of molecules and atoms become accessible at near-IR wavelengths, allowing for fluorescence lifetime measurements [22–24], compatibility with quantum memories [25], and fundamental studies of few-photon nonlinearities [10, 26, 27]. More generally, near-IR and visible photons can be detected with high quantum efficiency and low dark noise using existing mature silicon technology at room temperature, compared to IR detectors which require cryogenic cooling [28]. Despite these advantages, all demonstrations of nanophotonic pair production have resided in the telecom region, and the best near-IR and visible photon pair sources are still large-area waveguides [29–32] and bulk periodically poled crystals [10, 26, 29, 33–36]. To date, lithium niobate is the only nanophotonic platform that exhibits high transparency at near-UV pump wavelengths and support a $\chi^{(2)}$ nonlinearity. Thus, despite the known challenges, TFLN is uniquely posed to address this wavelength range. Potential reasons for the lack of visible TFLN devices stem from the difficulty in fabricating visible nonlinear circuits on thin-film lithium niobate due to factors such as the ultra-short poling periods required for quasi-phase matching and losses from material absorption [37–39] and scattering [40]. In spite of these difficulties, high-performance visible devices in thin-film lithium niobate are becoming increasingly common for classical applications such as electro-optic modulation and second harmonic generation [41–45].

Here, we extend TFLN-based SPDC sources to shorter wavelengths to produce high-brightness photon pairs in the visible and near-IR. The device produces an

on-chip efficiency of $(2.3 \pm 0.5) \times 10^{11}$ pairs/s/mW, which corresponds to a per-photon conversion efficiency of more than 1 photon pair converted in every 10,000 pump photons ($(1.1 \pm 0.2) \times 10^{-4}$ pairs/s/photon). This efficiency is nearly two orders of magnitude better than visible-light diffused waveguide SPDC sources[31] and is on par with the highest-performing TFLN sources in the telecom regime[8]. The SPDC from this device exhibits a broad spectrum centered at 811 nm with a degenerate FWHM bandwidth of 117 nm and an average brightness of $(1.6 \pm 0.3) \times 10^9$ pairs/s/mW/nm, a number limited by at least an order of magnitude by the pump laser linewidth (0.8 nm). Consistent with this bandwidth, we measure an ultrashort coherence time of ~40 fs for the entangled photons with an indistinguishability of 100. ± 1%. These results are the shortest wavelength entangled photons generated in TFLN by nearly an octave to date. Our results therefore show that, although pumped at wavelengths near what would usually be considered its cutoff range, TFLN can equally be a platform for visible through near-IR entangled photon applications as it is at telecom wavelengths.

4.2 Device design and fabrication

The periodically poled lithium niobate waveguides (Figure 4.1a) were simulated in Lumerical MODE to determine the quasi-phase matching poling period. The guided modes at the design pump wavelength (406 nm) and SPDC center wavelength (812 nm) were simulated using the bulk Sellmeier coefficients of lithium niobate [46] and silicon dioxide [47] with the geometric parameters shown in Figure 4.1c and a 60° sidewall, which is consistent with the fabrication process. To take advantage of lithium niobate's largest nonlinear tensor element (d_{33} = 28.4 pm/V)[48], only the fundamental quasi-transverse electric (TE) modes of X-cut lithium niobate were considered. An etch depth of 420 nm, a top width of 1.5 μm, and a total LN thin film thickness of 600 nm were targeted for ease of optical coupling, fabrication, elimination of slab-mode leakage, and near-2 μm poling period while providing high performance. For these parameters, the effective refractive indices ($n_{\text{eff,pump}} = 2.29$, $n_{\text{eff,SPDC}} = 2.09$) result in a quasi-phase matching poling period of $\Lambda = \lambda_{\text{pump}}/\Delta n_{\text{eff}} = 2.03\ \mu$m at the target pump wavelength of 406 nm (Figure 4.1d).

The devices were fabricated from a 1 cm by 1 cm die of a 5% MgO-doped X-cut thin-film lithium niobate on insulator wafer (NanoLN), which consists of 600 nm of lithium niobate bonded to 2 μm of silicon dioxide on a 0.4 mm silicon substrate. An MgO-doped film was chosen to lower the coercive field necessary for poling [49, 50] and to reduce potential photorefractive effects from the violet laser diode

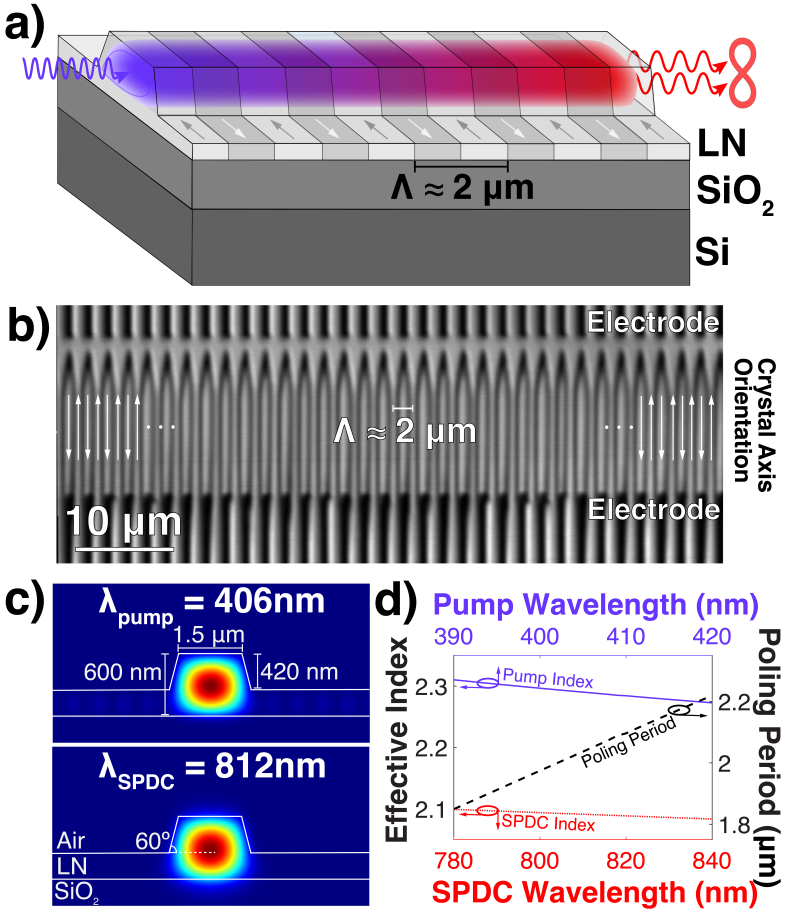

Figure 4.1: Design and fabrication of the periodically poled TFLN waveguides used for visible through near-IR SPDC. (a) Schematic of the periodically poled lithium niobate nanophotonic waveguide. (b) Second harmonic microscopy image of the periodic poling. Note that the distance between the electrodes is 15 μm while the waveguide top width is 1.5 μm, allowing for multiple waveguides in the center of the poled region where the duty cycle is 50%. (c) Mode profiles and waveguide geometry of the fundamental quasi-TE modes at the designed pump and SPDC center wavelengths. (d) Refractive indices and corresponding poling periods for a range of SPDC wavelengths.

[51]. MgO-doped LN has been demonstrated to lower propagation losses [38], but this doping may also result in irregular poled domains due to leakage current in the charged domain walls [50]. To quasi-phase match the SPDC sources, poling electrodes (7 mm long) were first fabricated by performing a metal lift-off through electron beam lithography with bilayer polymethyl methacrylate (PMMA) resist followed by electron beam evaporation of titanium (15 nm) and gold (55 nm). The electrodes were poled with a 490 V and 70 μs square wave, and the poled domain formation was monitored with second harmonic microscopy [52] (Figure 4.1b). After poling, waveguides were defined through an aligned electron beam lithography step with hydrogen silsesquioxane (HSQ) resist followed by argon inductive coupled plasma reactive ion etching to achieve an etch depth of 420 nm, verified through atomic force microscopy. The chip facets were manually polished to increase coupling efficiency, resulting in a final waveguide length of approximately 8 mm. A broadband oscillator was used to verify the phase matching wavelength through second harmonic generation (Appendix C.2) and was found to match with the computationally predicted second harmonic wavelength within ±3 nm. This small discrepancy was likely due to fabrication tolerances, particularly in the etch depth and film thickness.

4.3 Device characterization

The spectrum, generation rate, and coherence properties of the entangled photon pairs produced from the fabricated device are characterized as shown in Figure 4.2. In these experiments, the room-temperature periodically poled waveguide is pumped with a free-running laser diode (Coherent OBIS LX 405 nm) to produce entangled pairs (Figure 4.2a). An antireflection-coated aspheric lens (NA = 0.58, Thorlabs C140TMD-A) couples the free-space pump beam to the fundamental TE mode of the waveguide. The photon pairs produced in the fundamental TE mode are collected off-chip and collimated using a similar aspheric lens (NA = 0.58, Thorlabs C140TMD-B).

The spectra of the entangled photon pairs are measured to assess the phase-matching properties and tunability of the device (Figure 4.3). Pairs collected from the waveguide are transmitted to a grating spectrometer and measured using an electron-multiplying intensified camera (Figure 4.2b). To tune the SPDC emission, the center wavelength of the pump wavelength is varied from 405 to 406.4 nm by changing the drive current of the laser diode. Variable neutral-density filters are used to keep the pump power for all the collected spectra at a consistent 10 μW. Each spectrum

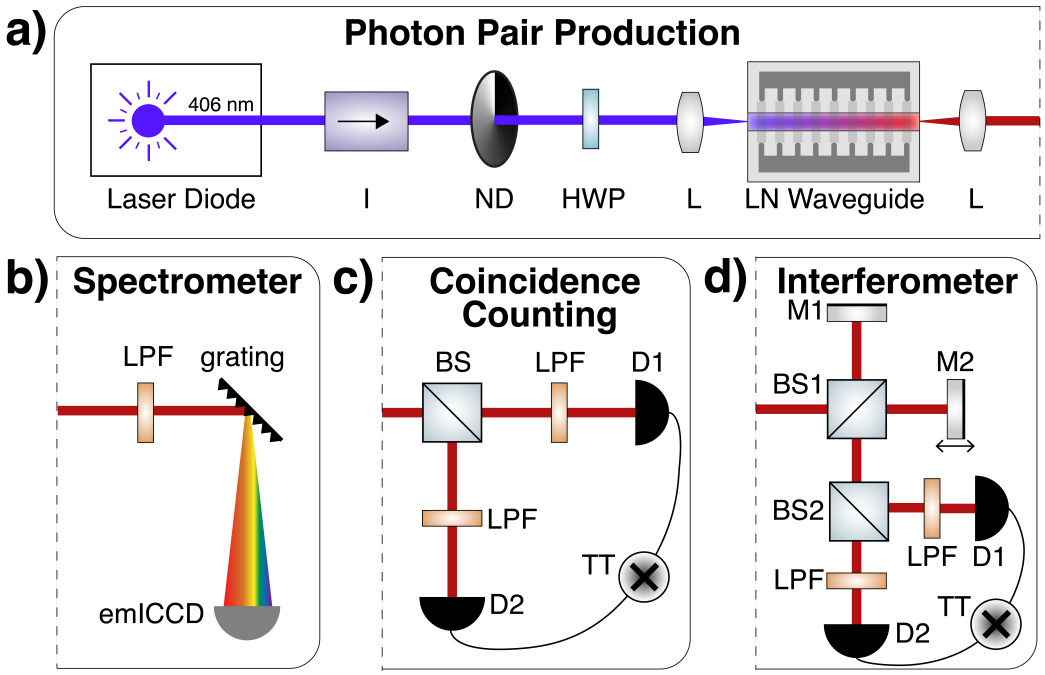

Figure 4.2: Schematic for coupling and detection of the photon pairs. Acronyms used: I, isolator; ND, variable neutral density filter; HWP, half-wave plate; L, aspheric lens; LPF, long-pass filter; emICCD, electron-multiplying intensified charge-coupled device; BS, beamsplitter; D, single-photon avalanche detector; TT, time-tagger; M, mirror. (a) Optical setup to couple into and out of the TFLN waveguide. (b) Characterization scheme for measuring the photon pair spectra. (c) Characterization scheme for coincidence counting. (d) Optical setup for the Michelson interferometer.

was divided by the spectrometer wavelength response and then normalized to the maximum count rate to infer the relative intensity. Three distinct phase matching regions are explored (Figure 4.3a): 1) at long pump wavelengths, the phase matching condition is not satisfied and SPDC emission is not observed; 2) from 405.6-405.9 nm, the degenerate wavelengths are phasematched; and 3) at short pump wavelengths, the spectrum splits and non-degenerate emission extending to the cutoff wavelength of the filter is observed. The dip in intensity in Figure 4.3a around 755 nm is likely due to on-chip loss, potentially from a mode-crossing [53], and is investigated in further detail with a transmission measurement (Appendix C.2). Due to the linewidth of the laser used in the experiment (0.8 nm FWHM), the spectra are considerably broadened compared to the spectra expected from a single-frequency pump laser (Figure C.4). Nevertheless, experiment and theory reach qualitative agreement by accounting for the pump linewidth (Figure 4.3b), described further in

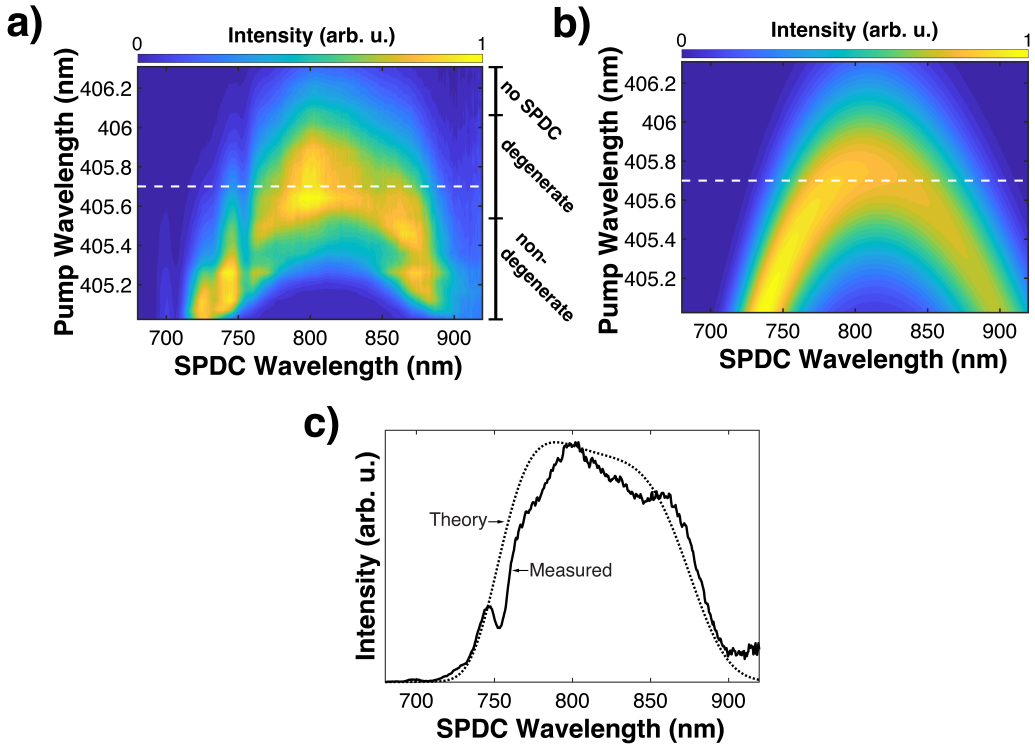

Figure 4.3: SPDC spectra from the TFLN waveguide. a) Measured and (b) theoretical SPDC spectra as a function of pump wavelength. Note that the arbitrary units for intensity could also be interpreted as counts per max counts due to the normalization of the spectra. (c) Lineouts of the measured and theoretical SPDC spectra at a pump wavelength of 405.7 nm, corresponding to the dashed horizontal lines in (a) and (b). Note that the frequency bandwidth per nm and the downconversion efficiency are wavelength dependent (Equation 2.51), resulting in higher intensities for shorter wavelengths. The theoretical spectra in (b) and (c) are calculated with the laser linewidth taken into account, described further in Appendix C.6

Appendix C.6. Further spectral broadening can also arise from propagation loss at the pump or SPDC wavelengths [54] or index variations [55–57]. For all subsequent experiments, a laser center wavelength of 405.7 nm is used for degenerate phase matching. The resulting spectrum (Figure 4.3c) is centered at 811.4 ± 0.7 nm with a FWHM bandwidth of 117 nm (53 THz) that accounts for 85% of the overall flux.

The pair generation efficiency of the device is measured through coincidence counting between two SPADs (Figure 4.2c). In this measurement, the pairs from the chip were split at a 50:50 broadband beamsplitter (Thorlabs BS014) and coupled to multimode optical fibers (Thorlabs M122L01) connected to the detectors. Coincidence detection events between the SPADs (Laser Components Count) were recorded with

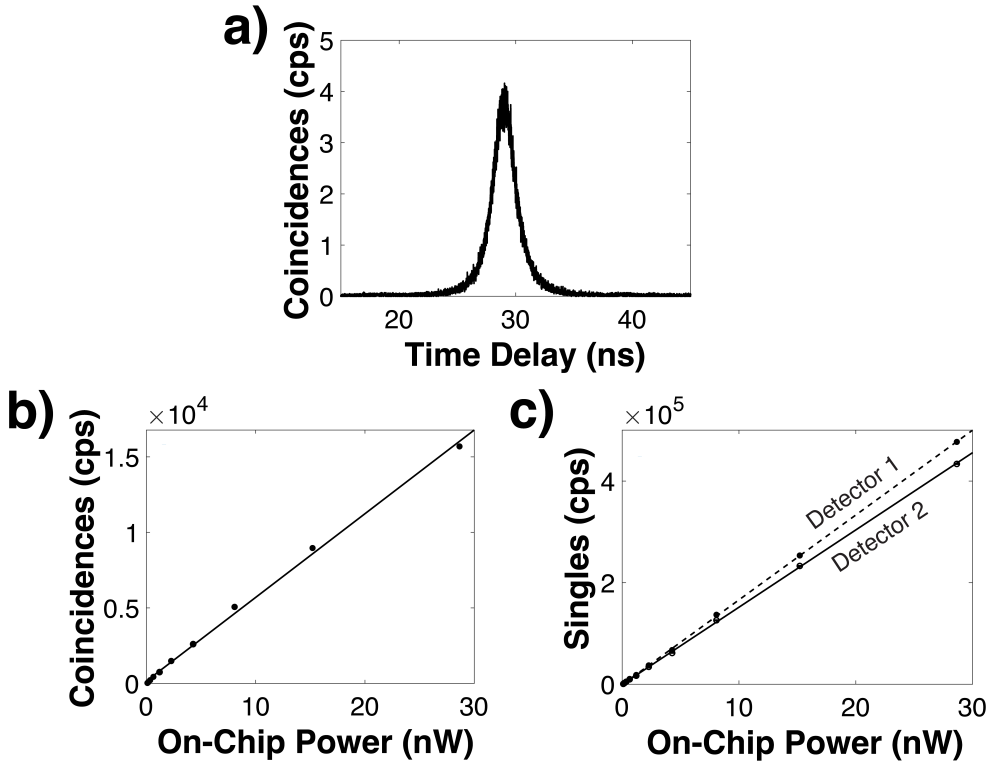

Figure 4.4: Coincidence histogram and power sweeps used to obtain the SPDC efficiency. (a) Raw coincidence histogram, including accidentals, at an input on-chip pump power of 4.3 nW. Measured (b) coincidence counts with accidentals subtracted and (c) singles counts while sweeping the input power. The vertical axes are measured in coincidence or singles counts per second (cps). The fitted slopes (lines) produce the pair generation efficiency of our device. Note that error bars are included in (b) and (c) but are smaller than the data markers. Additional experimental details and the raw data can be found in Appendix C.4 and Table C.1.

a time-tagger (Picoquant PicoHarp 300). Figure 4.4a shows a representative raw coincidence histogram recorded at 4.3 nW of on-chip pump power. The temporal correlation in this graph (3.4 ns FWHM) is given by the response time of the SPADs and not the entangled photon correlations (see Figure 4.5 later in the chapter). The coincidence counts are corrected by background subtraction of the number of counts in a 9.5 ns window at the histogram peak from the number of counts in another 9.5 ns window in a background region far from the peak. Sweeping the laser power with a neutral density filter yields the curves in Figure 4.4b-c, which are linearly fit to determine the pair generation efficiency. Additional experimental details and the raw data from these measurements are given in Appendix C.4 and Table C.1. To account for the wavelength dependence of the SPAD quantum efficiency (Appendix C.3), all

wavelengths in the spectrum are integrated over to calculate the average detection efficiency for single photons ($\eta_1 = 0.52$) as well as the average joint pair detection probability ($\eta_{12} = 0.27$). Including a factor of 2 due to the probability of splitting pairs at the beamsplitter yields Equation 4.1 for the measured efficiency of the source:

$$E = \frac{m_1 m_2}{m_c} \frac{\eta_{12}}{2\eta_1^2}. \tag{4.1}$$

Here E is the pair generation efficiency, m_1 and m_2 are the singles rates at the two detectors, and m_c is the rate of coincidences, all in units of counts/s/mW. A derivation of Equation 4.1 can be found in Appendix C.5. Accounting for the 10.2 dB transmission loss of the pump laser into the waveguide, a pair generation efficiency of $(2.3 \pm 0.5) \times 10^{11}$ pairs/s/mW is measured, which is equivalent to a per-pump-photon efficiency of $(1.1 \pm 0.2) \times 10^{-4}$ pairs/s/photon. Over the 117 nm FWHM bandwidth of the spectrum, this efficiency translates to an average brightness of $(1.6 \pm 0.3) \times 10^9$ pairs/s/nm/mW. The uncertainties here and throughout this work are reported as one standard deviation, derived from the standard error in the fits of Figure 4.4b-c and the uncertainty in the detector quantum efficiency. The ratio of singles counts to coincidence counts suggests that the transmission of the SPDC from the waveguide to each of the two detectors is 8.4 dB and 8.0 dB, respectively, which includes losses out of the waveguide and of the free-space optics. Our theoretical efficiency (Appendix C.6), including the FWHM of the pump laser, is 2.66×10^{11} pairs/s/mW, in close agreement with our experimental results.

Finally, the two-photon interference is measured (Figure 4.2d) to demonstrate the non-classical behaviour of the produced photon pairs. Figure 4.5 shows the measured two-photon interferogram (Figure 4.5a) obtained from the device without subtracting accidentals, as well as the one-photon interferogram (Figure 4.5c) for comparison. Due to the aforementioned temporal resolution of the SPADs used here, the four unique paths through the interferometer are indistinguishable and combine to yield the interference pattern. The important features of the interferogram are as follows: 1) Near the zero time delay, photons are delayed within the coherence length of the source and exhibit both one- and two-photon interference. A visibility of 100.±1% is measured within the coherence length, with an uncertainty derived assuming Poissonian statistics. This near-perfect visibility indicates good mode overlap in the interferometer and indistinguishability of the photons within the pair. 2) Far from the coherence length of the source (delays greater than ±20 fs), interference between two photons taking different paths disappears, which explains why the

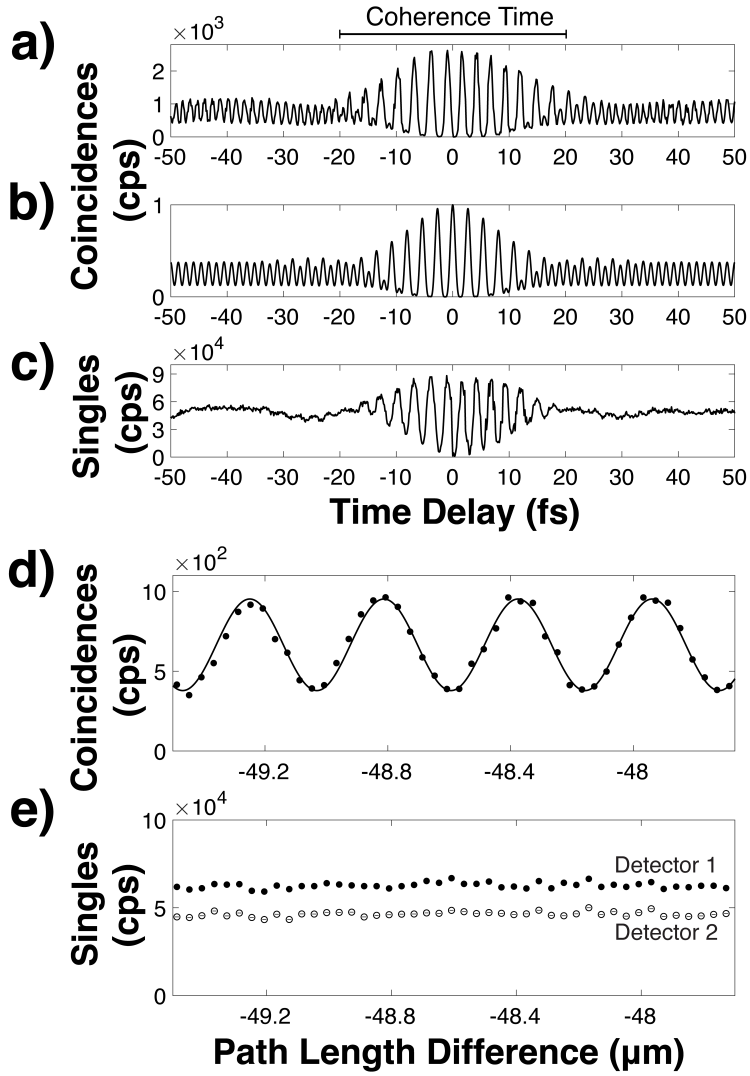

Figure 4.5: Michelson interferograms for SPDC. The (a) measured and (b) simulated two photon Michelson interferogram for the device. (c) Corresponding singles counts out of the interferometer, demonstrating single photon interference within the coherence length of the source. The (d) coincidence counts and (e) singles counts far from the coherence length of the source. All measured coincidence counts ((a) and (d)) do not have accidentals subtracted. Note that error bars are included in (d) and (e) but are smaller than the data markers. Details of the simulated two-photon Michelson interferogram in (b) and the sinusoidal fit in (d) can be found in Appendix C.7

single-photon interference (Figure 4.5c) disappears in this region, shown in more detail in Figure 4.5e. Notably, interference between pairs of photons that travel together through the interferometer persists with a fringe period at half the pair wavelength (Figure 4.5d). This feature suggests quantum interference due to the energy-time entanglement of the pairs, and would not be observed if the light was generated from a coherent or a thermal source with a similar spectrum [58]. A fringe visibility of $43 \pm 3\%$ is observed in this region far from the coherence length, which is close to the theoretical maximum of 50% for this experiment due to the temporal resolution of the detectors. The uncertainty in visibility is given from the standard error in the fit of Figure 4.5d, the details of which are outlined in Appendix C.7. The qualitative agreement between the measured and theoretical two-photon interferogram (Figure 4.5a-b) suggests that SPDC and genuine energy-time entanglement are being produced.

4.4 Discussion

Compared to the state of the art for visible photon pair sources, the device presented in this work exhibits substantially improved brightness and efficiency due to the small effective area of the nanophotonic waveguide. The device's performance against reported literature devices spanning from the visible to IR is plotted in Figure 4.6 using efficiency, brightness, and wavelength as the figures of merit. Our visible through near-IR device demonstrates improved efficiency and brightness even over other TFLN sources at the better-explored telecom band [6, 7, 9] and has comparable performance to the most efficient telecom TFLN source (Ref. [8]) to date. At short wavelengths, the phase-matching bandwidth decreases due to group velocity dispersion in lithium niobate, but the efficiency remains high because the downconversion spectral power density scales with the inverse fifth power of the SPDC wavelength (λ_s^{-5}) [29]. Thus, in addition to the benefits of higher-energy photon pairs, decreasing the SPDC wavelength to access higher efficiencies could enable single-photon nonlinearities when integrated with a resonator [59]. The high efficiency of this device has significant implications for practical uses of entangled photons, including allowing the use of low-power laser diodes for pair generation, reducing integration times, allowing high signal-to-noise coincidence measurements at low (nW) laser powers even with losses present, and reducing fluorescence and stray light.

Although the efficiency and brightness of the device compares well with literature, these values can be further improved by narrowing the bandwidth of the pump

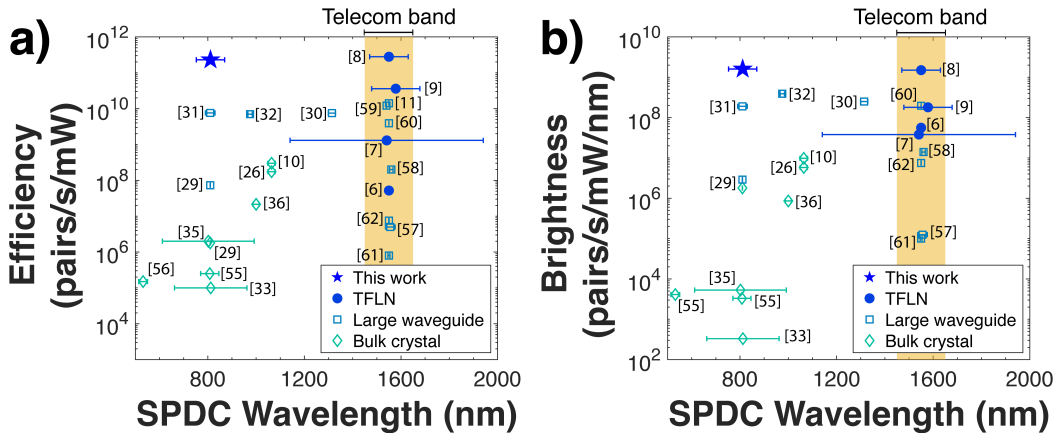

Figure 4.6: Comparison of relevant literature SPDC sources to this work with respect to (a) efficiency and (b) brightness against the SPDC wavelength. Horizontal error bars represent the reported bandwidth of the sources. Data for the efficiency, brightness, center wavelength, and bandwidth are taken from Refs. [10, 26, 29, 33, 35, 36, 60, 61] for bulk crystal sources, Refs. [11, 29–32, 62–67] for large waveguide sources (including micromachined and diffused waveguides), and Refs. [6–9] for TFLN sources. Note that Refs. [11, 64] are not included in (b) since the brightness and bandwidth were not reported. The yellow shaded region represents the typical telecommunication wavelength window.

laser, as discussed further in Appendix C.6. A single-frequency pump is estimated to shrink the phase-matching bandwidth from 117 nm to 35 nm, increasing the brightness by a comparable factor. The SPDC process is also most efficient near degeneracy because the group velocity of the signal and idler are equal to first order, so the efficiency could increase by a factor of 5. Furthermore, compared to SPDC produced with a monochromatic pump, the radiation produced here with a multimode pump will exhibit reduced time-energy entanglement (and greater separability) due to the uncertainty in the energy of the pump photons. The coherence properties of the pump laser are also transferred to the SPDC state, which can reduce the N00N state interference visibility at delays longer than the coherence length of the pump laser. Note that this negative effect is not observed here since the path length differences in Figure 4.5 cover more than the full coherence length of the SPDC source but less than the coherence length of the pump laser [68, 69], indicating that the pump laser coherence does not impair the visibilities measured in this work. Conversely, one benefit of using a multifrequency pump is that the device sensitivity to the laser wavelength is reduced, yielding a higher stability average response with greater bandwidth. Another benefit of the multifrequency pump is in time-bin entanglement, which can be generated from revivals in the biphoton

interference at integer multiples of the laser cavity length [70]. For these benefits as well as for the greater accessibility of multimode lasers, a multimode pump laser was utilized in this work to represent an alternate and more applied use of photon pair sources. Furthermore, despite the aforementioned drawbacks of a multimode pump, the device was still able to achieve high efficiencies on par with the current state of the art telecom TFLN pair sources.

4.5 Conclusion

Efficient photon pair generation has been demonstrated with an integrated thin-film lithium niobate waveguide at visible and near-IR wavelengths (720-900 nm). An on-chip SPDC efficiency of $(2.3 \pm 0.5) \times 10^{11}$ pairs/s/mW, which is on par with reported TFLN literature at the better-explored telecom wavelengths even with a multimode pump laser, has been produced near the usually associated cut-off wavelengths for the pump (406 nm) in TFLN. The photon pair spectra has an average brightness of $(1.6 \pm 0.3) \times 10^9$ pairs/s/mW/nm, centered at 811 nm with a 117 nm bandwidth. To date, these results are the shortest wavelength photon pairs generated in a thin film platform by nearly an octave. The work opens up opportunities to exploit the quantum advantage of integrated entangled photon circuits beyond telecom to imaging and spectroscopy applications in the visible and near-IR.

References

[1] M. Jankowski, C. Langrock, B. Desiatov, A. Marandi, C. Wang, M. Zhang, C. R. Phillips, M. Lončar, M. M. Fejer, *Optica* **2020**, *7*, 40.

[2] C. Wang, C. Langrock, A. Marandi, M. Jankowski, M. Zhang, B. Desiatov, M. M. Fejer, M. Lončar, *Optica* **2018**, *5*, 1438.

[3] R. Nehra, R. Sekine, L. Ledezma, Q. Guo, R. M. Gray, A. Roy, A. Marandi, *Science* **2022**, *377*, 1333–1337.

[4] A. Boes, L. Chang, C. Langrock, M. Yu, M. Zhang, Q. Lin, M. Lončar, M. Fejer, J. Bowers, A. Mitchell, *Science* **2023**, *379*, eabj4396.

[5] D. Zhu, L. Shao, M. Yu, R. Cheng, B. Desiatov, C. J. Xin, Y. Hu, J. Holzgrafe, S. Ghosh, A. Shams-Ansari, E. Puma, N. Sinclair, C. Reimer, M. Zhang, M. Lončar, *Advances in Optics and Photonics* **2021**, *13*, 242.

[6] J. Zhao, C. Ma, M. Rüsing, S. Mookherjea, *Physical Review Letters* **2020**, *124*, 163603.

[7] U. A. Javid, J. Ling, J. Staffa, M. Li, Y. He, Q. Lin, *Physical Review Letters* **2021**, *127*, 183601.

[8] G.-T. Xue, Y.-F. Niu, X. Liu, J.-C. Duan, W. Chen, Y. Pan, K. Jia, X. Wang, H.-Y. Liu, Y. Zhang, P. Xu, G. Zhao, X. Cai, Y.-X. Gong, X. Hu, Z. Xie, S. Zhu, *Physical Review Applied* **2021**, *15*, 064059.

[9] Y. Zhang, H. Li, T. Ding, H. Yiwen, L. Liang, X. Sun, Y. Tang, J. Wang, S. Liu, Y. Zheng, X. Chen, *Optica* **2023**, *10*, 688–693.

[10] B. Dayan, A. Pe'er, A. A. Friesem, Y. Silberberg, *Physical Review Letters* **2005**, *94*, 043602.

[11] M. Bock, A. Lenhard, C. Chunnilall, C. Becher, *Optics Express* **2016**, *24*, 23992.

[12] T. Miya, Y. Terunuma, T. Hosaka, T. Miyashita, *Electronics Letters* **1979**, *15*, 106.

[13] K. Nagayama, M. Kakui, M. Matsui, T. Saitoh, Y. Chigusa, *Electronics Letters* **2002**, *38*, 1168.

[14] N. Gisin, R. Thew, *Nature Photonics* **2007**, *1*, 165–171.

[15] J. L. O'Brien, *Science* **2007**, *318*, 1567–1570.

[16] H. J. Kimble, *Nature* **2008**, *453*, 1023–1030.

[17] E. Toninelli, P.-A. Moreau, T. Gregory, A. Mihalyi, M. Edgar, N. Radwell, M. Padgett, *Optica* **2019**, *6*, 347.

[18] H. Defienne, P. Cameron, B. Ndagano, A. Lyons, M. Reichert, J. Zhao, A. R. Harvey, E. Charbon, J. W. Fleischer, D. Faccio, *Nature Communications* **2022**, *13*, 3566.

[19] P.-A. Moreau, E. Toninelli, T. Gregory, M. J. Padgett, *Nature Reviews Physics* **2019**, *1*, 367–380.

[20] D. Zia, N. Dehghan, A. D'Errico, F. Sciarrino, E. Karimi, *Nature Photonics* **2023**, DOI 10.1038/s41566-023-01272-3.

[21] Y. Zhang, D. England, A. Nomerotski, B. Sussman, *Optics Express* **2021**, *29*, 28217.

[22] N. Harper, B. P. Hickam, M. He, S. K. Cushing, *The Journal of Physical Chemistry Letters* **2023**, *14*, 5805–5811.

[23] A. Eshun, X. Yi, A. Wilson, S. Jeppson, J. H. Yoo, S. Kiannejad, M. Rushford, T. Bond, T. Laurence, *Optics Express* **2023**, *31*, 26935.

[24] G. Scarcelli, S. H. Yun, *Optics Express* **2008**, *16*, 16189.

[25] H. Zhang, X.-M. Jin, J. Yang, H.-N. Dai, S.-J. Yang, T.-M. Zhao, J. Rui, Y. He, X. Jiang, F. Yang, G.-S. Pan, Z.-S. Yuan, Y. Deng, Z.-B. Chen, X.-H. Bao, S. Chen, B. Zhao, J.-W. Pan, *Nature Photonics* **2011**, *5*, 628–632.

[26] D. Tabakaev, A. Djorović, L. La Volpe, G. Gaulier, S. Ghosh, L. Bonacina, J.-P. Wolf, H. Zbinden, R. T. Thew, *Physical Review Letters* **2022**, *129*, 183601.

[27] A. Pe'er, B. Dayan, A. A. Friesem, Y. Silberberg, *Physical Review Letters* **2005**, *94*, 073601.

[28] F. Ceccarelli, G. Acconcia, A. Gulinatti, M. Ghioni, I. Rech, R. Osellame, *Advanced Quantum Technologies* **2021**, *4*, 2000102.

[29] M. Fiorentino, S. M. Spillane, R. G. Beausoleil, T. D. Roberts, P. Battle, M. W. Munro, *Optics Express* **2007**, *15*, 7479.

[30] S. Tanzilli, H. De Riedmatten, W. Tittel, H. Zbinden, P. Baldi, M. De Micheli, D. Ostrowsky, N. Gisin, *Electronics Letters* **2001**, *37*, 26.

[31] T. B. Gäbler, P. Hendra, N. Jain, M. Gräfe, *Advanced Physics Research* **2024**, *3*, 2300037.

[32] A. Jechow, A. Heuer, R. Menzel, *Optics Express* **2008**, *16*, 13439.

[33] M. B. Nasr, S. Carrasco, B. E. A. Saleh, A. V. Sergienko, M. C. Teich, J. P. Torres, L. Torner, D. S. Hum, M. M. Fejer, *Physical Review Letters* **2008**, *100*, 183601.

[34] A. Tanaka, R. Okamoto, H. H. Lim, S. Subashchandran, M. Okano, L. Zhang, L. Kang, J. Chen, P. Wu, T. Hirohata, S. Kurimura, S. Takeuchi, *Optics Express* **2012**, *20*, 25228.

[35] M. Okano, H. H. Lim, R. Okamoto, N. Nishizawa, S. Kurimura, S. Takeuchi, *Scientific Reports* **2015**, *5*, 18042.

[36] S. Sensarn, G. Y. Yin, S. E. Harris, *Physical Review Letters* **2010**, *104*, 253602.

[37] R. Bhatt, I. Bhaumik, S. Ganesamoorthy, A. K. Karnal, M. K. Swami, H. S. Patel, P. K. Gupta, *Physica Status Solidi (a)* **2012**, *209*, 176–180.

[38] J. R. Schwesyg, M. C. C. Kajiyama, M. Falk, D. H. Jundt, K. Buse, M. M. Fejer, *Applied Physics B* **2010**, *100*, 109–115.

[39] M. V. Ciampolillo, A. Zaltron, M. Bazzan, N. Argiolas, C. Sada, *Applied Spectroscopy* **2011**, *65*, 216–220.

[40] R. Maurer, *Proceedings of the IEEE* **1973**, *61*, 452–462.

[41] S. Xue, Z. Shi, J. Ling, Z. Gao, Q. Hu, K. Zhang, G. Valentine, X. Wu, J. Staffa, U. A. Javid, Q. Lin, *Optica* **2023**, *10*, 125–126.

[42] D. Renaud, D. R. Assumpcao, G. Joe, A. Shams-Ansari, D. Zhu, Y. Hu, N. Sinclair, M. Loncar, *Nature Communications* **2023**, *14*, 1496.

[43] T. Park, H. S. Stokowski, V. Ansari, T. P. McKenna, A. Y. Hwang, M. M. Fejer, A. H. Safavi-Naeini, *Optics Letters* **2022**, *47*, 2706.

[44] B. Desiatov, A. Shams-Ansari, M. Zhang, C. Wang, M. Lončar, *Optica* **2019**, *6*, 380–384.

[45] A. A. Sayem, Y. Wang, J. Lu, X. Liu, A. W. Bruch, H. X. Tang, *Applied Physics Letters* **2021**, *119*, 231104.

[46] O. Gayer, Z. Sacks, E. Galun, A. Arie, *Applied Physics B* **2008**, *91*, 343–348.

[47] T. Toyoda, M. Yabe, *Journal of Physics D: Applied Physics* **1983**, *16*, L97–L100.

[48] I. Shoji, T. Kondo, A. Kitamoto, M. Shirane, R. Ito, *Journal of the Optical Society of America B* **1997**, *14*, 2268.

[49] K. Mizuuchi, A. Morikawa, T. Sugita, K. Yamamoto, *Journal of Applied Physics* **2004**, *96*, 6585–6590.

[50] J. T. Nagy, R. M. Reano, *Optical Materials Express* **2019**, *9*, 3146.

[51] Y. Furukawa, K. Kitamura, S. Takekawa, A. Miyamoto, M. Terao, N. Suda, *Applied Physics Letters* **2000**, *77*, 2494–2496.

[52] M. Rüsing, J. Zhao, S. Mookherjea, *Journal of Applied Physics* **2019**, *126*, 114105.

[53] Y. Hu, M. Yu, B. Buscaino, N. Sinclair, D. Zhu, R. Cheng, A. Shams-Ansari, L. Shao, M. Zhang, J. M. Kahn, M. Lončar, *Nature Photonics* **2022**, *16*, 679–685.

[54] L. G. Helt, M. J. Steel, J. E. Sipe, *New Journal of Physics* **2015**, *17*, 013055.

[55] J. Zhao, X. Li, T.-C. Hu, A. A. Sayem, H. Li, A. Tate, K. Kim, R. Kopf, P. Sanjari, M. Earnshaw, N. K. Fontaine, C. Wang, A. Blanco-Redondo, *APL Photonics* **2023**, *8*, 126106.

[56] P. S. Kuo, *Optics Letters* **2022**, *47*, 54.

[57] P.-K. Chen, I. Briggs, C. Cui, L. Zhang, M. Shah, L. Fan, *Nature Nanotechnology* **2024**, *19*, 44–50.

[58] Z. Y. Ou, X. Y. Zou, L. J. Wang, L. Mandel, *Physical Review Letters* **1990**, *65*, 321–324.

[59] M. Jankowski, J. Mishra, M. M. Fejer, *Journal of Physics: Photonics* **2021**, *3*, 042005.

[60] M. Okano, R. Okamoto, A. Tanaka, S. Subashchandran, S. Takeuchi, *Optics Express* **2012**, *20*, 13977.

[61] J. Lavoie, T. Landes, A. Tamimi, B. J. Smith, A. H. Marcus, M. G. Raymer, *Advanced Quantum Technologies* **2020**, *3*, 1900114.

[62] D. Kang, A. Anirban, A. S. Helmy, *Optics Express* **2016**, *24*, 15160.

[63] H. Jin, F. M. Liu, P. Xu, J. L. Xia, M. L. Zhong, Y. Yuan, J. W. Zhou, Y. X. Gong, W. Wang, S. N. Zhu, *Physical Review Letters* **2014**, *113*, 103601.

[64] E. Meyer-Scott, D. McCloskey, K. Gołos, J. Z. Salvail, K. A. G. Fisher, D. R. Hamel, A. Cabello, K. J. Resch, T. Jennewein, *Physical Review Letters* **2016**, *116*, 070501.

[65] D.-S. Ding, W. Zhang, S. Shi, Z.-Y. Zhou, Y. Li, B.-S. Shi, G.-C. Guo, *Optica* **2015**, *2*, 642.

[66] P. Sarrafi, E. Y. Zhu, B. M. Holmes, D. C. Hutchings, S. Aitchison, L. Qian, *Optics Letters* **2014**, *39*, 5188.

[67] G. Fujii, N. Namekata, M. Motoya, S. Kurimura, S. Inoue, *Optics Express* **2007**, *15*, 12769.

[68] A. V. Burlakov, M. V. Chekhova, O. A. Karabutova, S. P. Kulik, *Physical Review A* **2001**, *63*, 053801.

[69] O. Kwon, Y.-S. Ra, Y.-H. Kim, *Optics Express* **2009**, *17*, 13059–13069.

[70] O. Kwon, K.-K. Park, Y.-S. Ra, Y.-S. Kim, Y.-H. Kim, *Optics Express* **2013**, *21*, 25492–25500.

Chapter 5

ON-CHIP SAMPLE INTERACTIONS FOR EVANESCENT WAVE SENSING

Thin-film lithium niobate (TFLN) is promising for optical sensing due to its high nonlinearities, but its material properties present unique design challenges. We compare the sensing performance of the fundamental modes on a TFLN waveguide with a fluorescent dye sample. The TM mode has better overlap with the sample, with a 1.4× greater sample absorption rate versus the TE mode. However, the TM mode also scatters at a 1.4× greater rate, yielding less fluorescence overall. The TE mode is, therefore, more appropriate for sensing. Our findings have important implications for TFLN-based sensor designs. Supplementary theory and dye measurements can be found in Appendix D.

Most of this chapter has been adapted with permission from:
N. A. Harper, E. Y. Hwang, P. A. Kocheril, T. K. Lam, S. K. Cushing, *Optics Express* **2024**, *32*, 27931

5.1 Introduction

Thin-film lithium niobate is a promising candidate for on-chip sensing because its strong nonlinearities and low material losses allow for light generation, manipulation, and sample interaction within the same compact device [1, 2]. Lithium niobate's strong quadratic nonlinearity, sub-μm modal confinement, and ability for quasi-phase matching lead to efficient frequency conversion through second harmonic generation [3], optical parametric amplification [4], optical parametric oscillation [5, 6], and spontaneous parametric downconversion [7, 8]. TFLN has been used to generate light spanning from the UV-A [9] to the mid-IR [10] in photonic circuits, with efficiencies unmatched in any other platform. Lithium niobate's electro-optic effect and versatile fabrication allows for the efficient modulation of light with low voltages, high bandwidths, compact footprints, and excellent insertion losses [11, 12]. Electro-optic modulators on TFLN can also be utilized as light sources, including frequency combs [13, 14], ultrafast laser pulses [15], and frequency shifters [16]. Efficient switches are useful for routing light to different sensing regions on one chip, and the electro-optic effect has been harnessed to increase the resolution of on-chip Fourier-transform interferometers [17]. With

the addition of waveguided detectors [18], the components necessary for a fully integrated optical sensor can all be fabricated on TFLN.

While frequency conversion sources and electro-optic modulation in TFLN are being widely explored, integrated sample interaction geometries for on-chip sensors are less studied. Since the evanescent field of light coupled into a waveguide extends only a few hundred nanometers past its surface, evanescent field sensing allows for highly specific analyte interrogation [19–21]. Evanescent wave sensors have been implemented in materials such as silicon, silicon nitride, and glass with multiple waveguide architectures, including fiber optic waveguides, planar waveguides, slot waveguides, rib waveguides, and strip waveguides [22–25]. For example, TE slot waveguides and TM strip waveguides have been proposed as optimal sensing geometries on silicon-on-insulator (SOI) based on the modal confinement factors and scattering losses of these waveguide configurations in the SOI platform [26]. However, the material properties of lithium niobate present additional concerns for evanescent wave sensing designs. Lithium niobate's angled sidewall profile, which is a well known feature of the TFLN platform and arises due to redeposition from the physical nature of the waveguide etching process [27], makes slot waveguides difficult to fabricate, and its high refractive index and birefringence present unique design challenges to sample interaction geometries, warranting additional study. Evanescent wave sensing can be modeled with mode overlap calculations between the waveguide mode and the sample to investigate the efficiency of the sample excitation. However, practical devices need to account for additional sources of loss that are not easily captured by modeling, such as the scattering from sub-wavelength imperfections in the waveguide profile, scatterers in the sample, and the refractive index contrast at the material interfaces. While it is known that the TM mode exhibits larger losses than the TE mode in some bare TFLN waveguides [28], it is unknown if this relationship holds with the addition of a sample, or if the gains in the sample-mode overlap outweigh the additional scattering losses.

Here, we quantify the interaction strength of the guided modes with a sample in a model TFLN waveguide fluorescent dye sensor. The sensing region is an X-cut TFLN rib waveguide clad with a sample layer that consists of a 5 mM fluorescent dye (Coumarin-153) doped in a 60 nm thick poly(methyl methacrylate) polymer film. The device is pumped with a 406 nm diode laser, yielding a fluorescence signal from 450-700 nm which is detected with a camera. By measuring the fluorescence and scatter from the dye sample along the length of the waveguide, we determine the

amount of light absorbed by the sample compared to the amount of light scattered from the waveguide. Theoretical models predict that the fundamental TM mode of the rib waveguide has a nearly two-fold larger overlap with the sample than the quasi-transverse-electric (TE) mode. Experimentally, the TM mode is more efficiently absorbed by the sample than the TE mode by a factor of 1.4 (desired sample absorption of 0.95 ± 0.01 dB/cm and 0.67 ± 0.01 dB/cm, respectively). However, the scattering losses are also larger for the TM mode compared to the TE mode by a factor of 1.4 (undesired scattering losses of 31.5±0.3 dB/cm and 22.4±0.2 dB/cm, respectively). The TM mode thus loses its apparent advantage because of the realities of non-ideal waveguide sidewalls and sample nonuniformities. The TE mode within an X-cut TFLN film accesses the strongest optical and electro-optic nonlinearities in TFLN (d_{33} = 28.4 pm/V) since the mode is polarized along the crystal's optical axis. Therefore, the finding that the TE mode can be directly used for sensing is important for sensor compatibility with integrated frequency conversion sources and modulators. Our comparison of theory and experiment also provides important correction factors for modeling realistic waveguide properties in TFLN waveguide sensors.

5.2 Device design, fabrication, and characterization

The waveguide with the sample layer was modeled in Lumerical MODE before fabrication (Figure 5.1b-d). The confinement factors [29] and the propagation losses of the fundamental TE and TM waveguide modes are calculated in the presence of the Coumarin-153 (C153) dye-doped poly(methyl methacrylate) (PMMA) sample film. For a fixed device aspect ratio, the confinement factor is inversely proportional to the lithium niobate thickness because the mode is delocalized from the rib into the sample cladding, resulting in stronger sample absorption. This behavior is quantified in Appendix D.1 for thin-film thicknesses ranging from 100-600 nm. For a 406 nm pump wavelength, waveguides with total lithium niobate thicknesses <400 nm exhibit a confinement factor larger than 0.01 for the TM mode. For the waveguide geometry shown in Figure 5.1b, the confinement factors of the fundamental TM and TE modes in the PMMA/C153 film are 0.013 and 0.0073, respectively. In a 60 nm homogeneous PMMA/C153 film (as experimentally measured through profilometry), the theoretical sample absorption loss due to the presence of the dye molecules is calculated as 7.2 dB/cm for the TM mode and 4.4 dB/cm for the TE mode. The difference in sample absorption loss between the modes arises from the difference in the electric field profile between the two fundamental waveguide

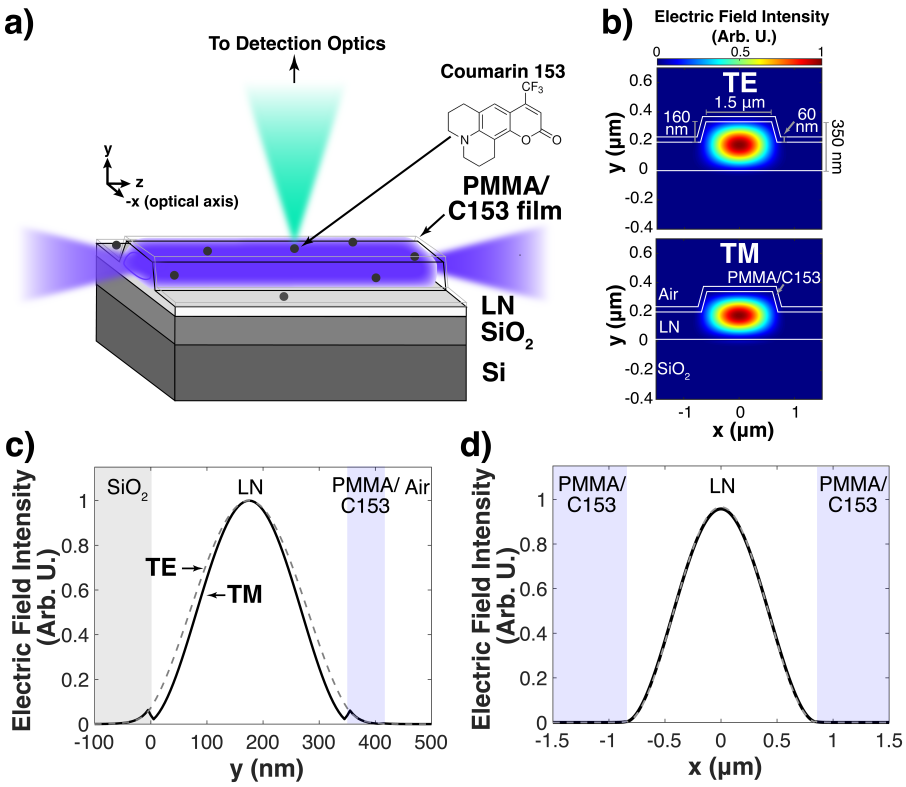

Figure 5.1: Device design of the TFLN waveguides for evanescent wave sensing. (a) Schematic of the lithium niobate nanophotonic waveguides and PMMA/C153 film. Note that in the coordinate system used here, the x-axis is parallel to the optical axis of lithium niobate. (b) Waveguide geometry and calculated electric field profiles profiles of the fundamental TE and TM modes using Lumerical. Lineouts of the simulated electric field in the (c) y direction in the center of the waveguide (at $x = 0$ μm) and (d) x direction in the PMMA/C153 film (at $y = 200$ nm).

modes, and is related to the aspect ratio of the waveguides relative to the polarization of the fundamental guided modes (Figure 5.1c-d).

The waveguides were then fabricated from an 8 mm by 12 mm die of a 5% MgO-doped X-cut thin-film lithium niobate on insulator wafer (NanoLN), which consists of 350 nm of lithium niobate bonded to 2 µm of silicon dioxide on a 0.4 mm silicon substrate. Waveguides were patterned through an electron beam lithography exposure with hydrogen silesoxquiane resist (Applied Quantum Materials Inc.) followed by argon inductively coupled plasma reactive ion etching. The final device geometry consists of a lithium niobate rib waveguide with a 1.5 µm top width and 160 nm etch depth (Figure 5.1b). The chip facets were manually polished to increase coupling efficiency, resulting in a final waveguide length of approximately 5 mm.

The PMMA/C153 films were prepared after the waveguide fabrication. To form the films, 1 µL of a 10 mM stock solution of Coumarin 153 (Millipore Sigma 546186) in dimethyl sulfoxide (DMSO, Millipore Sigma 276855) was added to 99 µL of a PMMA (Millipore Sigma 182230) solution (1% in toluene; Millipore Sigma 244511). 20 µL of the PMMA/C153 solution was deposited on the TFLN chip by spin coating (MicroNano Tools BSC-100) at 300 rpm for 10 s followed by 2000 rpm for 60 s. The spin coating results in a film thickness of ~60 nm, confirmed through profilometry on a separate device and in good agreement with literature [30]. Assuming minimal evaporation of DMSO, the C153 concentration is approximately 5 mM in the film. A confocal fluorescence micrograph verified that the film was relatively homogeneous across the sample, though strong variations in the fluorescence at the waveguide sidewalls and surface were observed (Appendix D.3).

The fluorescence and scatter from the PMMA/C153 film on the waveguide are characterized as shown in Figure 5.2a. In these experiments, the room-temperature waveguide is pumped with a free-running 406 nm laser diode (Coherent OBIS LX 406 nm) to excite the C153 dye, causing the sample to fluoresce from 450-700 nm (Appendix D.3). An antireflection-coated aspheric lens (NA = 0.58, Thorlabs C140TMD-A) couples the free-space pump beam to the fundamental TE or TM mode of the waveguide depending on the polarization of the free-space beam, which is tuned with a half-wave plate. The total scatter from the top of the waveguides is collected using a camera lens (Edmund Optics 54691, f =75 mm, operated at $f/4$ with a 300 mm working distance) and camera (Teledyne FLIR BFLY-U3-23S6M-C), with a collection efficiency of 0.025%. To measure the fluorescence, a 500 nm long pass filter (Thorlabs FELH0500) is used with an optical density >5 at the pump wavelength while rejecting only 10% of the generated fluorescence. A second aspheric lens collects the output of the waveguide into a power meter to monitor the stability of the coupling. Figure 5.2b shows an image of the device and the coupling lenses used in this setup. All images were acquired for 5 minutes and were background corrected using images recorded with the laser shuttered. The images with the longpass filter were acquired for 1000 ms at 1 FPS (300 images total), while the images without the longpass filter were acquired for 100 ms at 10 FPS (3000 images total). To avoid photobleaching the dye, the alignment into the waveguide was performed at 5 nW of free-space power and image acquisition was performed with 100 nW of free-space power (Appendix D.5).

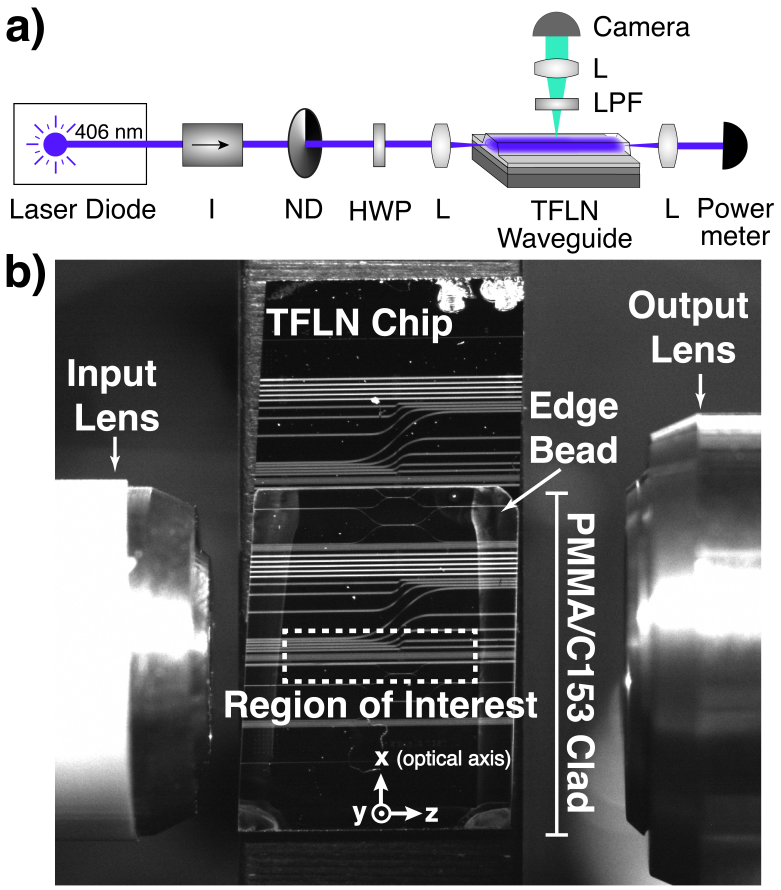

Figure 5.2: Characterization scheme to measure the dye fluorescence. (a) Optical setup for waveguide coupling and fluorescence detection. Acronyms used: I, isolator; ND, variable neutral density filter; HWP, half-wave plate; L, lens; LPF, long-pass filter. (b) Optical image of the lithium niobate chip and lens setup with the PMMA/C153 clad area, edge bead, and region of interest marked.

Due to the presence of an edge bead in the PMMA/C153 layer from the spin-coating process, a 4.3 mm section in the center of the waveguide with uniform film thickness (region of interest in Figure 5.2b) is used for data analysis. The images are processed by summing the intensity of 24 vertical pixels at each horizontal pixel along the waveguide. The fluorescence counts are scaled up by 11% to account for loss caused by the filter in the C153 emission spectrum passband (Appendix D.2). The counts from scatter are measured by subtracting the counts due to fluorescence from the counts recorded without the filter in place. A lithographically defined feature on the device is used to infer the measurement dimensions from the camera images.

5.3 Results and discussion

Figure 5.3 shows the intensities measured across the images of the PMMA/C153-clad waveguide when the TE and TM modes are excited. The traces are fit with a single exponential of the form $Ae^{-\alpha x}$, where x is length, α is the propagation loss of the device with units of length^{-1}, and A is a scaling term. The propagation loss of the TE mode is 23.0 ± 0.2 dB/cm, while the propagation loss of the TM mode is 32.5 ± 0.3 dB/cm, both inferred from the fluorescence images. A similar measurement using a bare waveguide determined that the propagation loss is 16.1 ± 0.5 dB/cm for the TE mode, and 18.1 ± 0.7 dB/cm for the TM mode, as summarized in Table 5.1. The PMMA/C153 cladding therefore introduces additional loss to the waveguide.

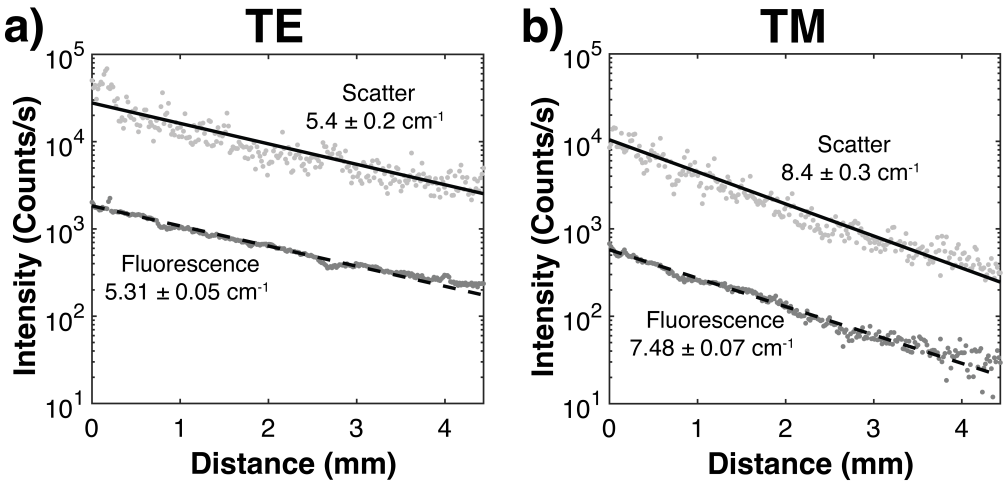

Figure 5.3: Measured fluorescence and scatter in the waveguide region of interest when coupled into the (a) TE and (b) TM modes.

Figure 5.3 shows that the intensity of the scattered signal is larger than the intensity of the fluorescence signal, which suggests that scattering is a more efficient loss mechanism than sample absorption in the device. The fluorescence loss and scattering loss show good agreement for the TE mode (23.0 ± 0.2 dB/cm and 23.4 ± 0.9 dB/cm, respectively) but show some disagreement for the TM mode (32.5 ± 0.3 dB/cm and 37 ± 1 dB/cm, respectively), most likely due to the higher sensitivity of the TM mode to sidewall scattering and PMMA film variations. Since the fluorescence intensity shows less spatial variance than the scattering intensity (Figure 5.3 and Figure D.4), the loss coefficient measured via fluorescence is chosen for all subsequent results.

To model how the individual losses of sample absorption $\alpha_{\text{absorption}}$ and scattering α_{scatter} contribute to the total propagation loss α_{total} inferred from Figure 5.3, a modified form of Beer's law can be used:

$$-\frac{1}{I(z)}\left(\frac{\mathrm{d}I(z)}{\mathrm{d}z}\right) = \alpha_{\text{scatter}} + \alpha_{\text{absorption}} = \alpha_{\text{total}}. \tag{5.1}$$

Here, $I(z)$ is the intensity of the pump laser along the length of the waveguide. At each location along the waveguide, the number of photons lost to absorption $N_{\text{absorption}}(z)$ compared to the number of photons lost to scatter $N_{\text{scatter}}(z)$ is given by:

$$\frac{N_{\text{absorption}}(z)}{N_{\text{scatter}}(z)} = \frac{\alpha_{\text{absorption}}}{\alpha_{\text{scatter}}}. \tag{5.2}$$

The number of photons lost to absorption and scatter can be inferred from the data of Figure 5.3. With the knowledge of the total propagation loss α_{total}, the individual loss coefficients of absorption and scatter are then given by:

$$\alpha_{\text{absorption}} = \alpha_{\text{total}}\frac{N_{\text{absorption}}(z)}{N_{\text{absorption}}(z) + N_{\text{scatter}}(z)} \tag{5.3}$$

$$\alpha_{\text{scatter}} = \alpha_{\text{total}}\frac{N_{\text{scatter}}(z)}{N_{\text{absorption}}(z) + N_{\text{scatter}}(z)}. \tag{5.4}$$

Since Equations 5.1-5.4 hold over the entire length of the waveguide, the total number of photons lost through the region of interest $N_{\text{absorption}}$ and N_{scatter} can be substituted for their spatially-dependent counterparts.

Over the 4.3 mm section of the waveguide used for loss measurements, the ratio of total counts due to scatter versus total counts due to fluorescence is 15.82 ± 0.01 and 15.73 ± 0.04 for the TE and TM modes, respectively. The raw integrated counts can be found in Appendix D.6. To relate the scatter-to-fluorescence ratio to the scatter-to-absorption ratio ($N_{\text{scatter}}/N_{\text{absorption}}$), the following factors are taken into account: 1) The collection efficiency of the system is the same for any photon radiated from the waveguide. 2) The camera quantum efficiency is 30% at 406 nm and ~70% over the emission range of C153 (500-600 nm), as reported on the camera datasheet. 3) Fluorescence from the dye has a 90% chance of transmitting through the filter based on the filter attenuation. 4) The quantum yield of Coumarin-153 in PMMA is 90%, the same as its quantum yield in nonpolar solvents such as

cyclohexane [31]. 5) The PMMA film is thin enough that absorption of scatter and fluorescence reabsorption is negligible for both the TE and TM modes. With these assumptions, the probability that a photon lost to molecular absorption generates a count through fluorescence is roughly 2.1 times as high as the probability that a photon lost to scatter generates a count. The ratios of the scatter to molecular absorption for the TE and TM modes are therefore 33.22 ± 0.02 and 33.03 ± 0.08, respectively. The individual loss coefficients consistent with these ratios and the measured total propagation loss are displayed in Table 5.1. The measured ratios confirm that scattering dominates the overall propagation loss in both the TE and TM modes. Compared to the TE mode, the TM mode is measured to experience higher loss, but not to a degree proportional to the fluorescence. Increased scattering in the TM mode is largely responsible for the increased total propagation loss, most likely due to inhomogeneities in the sample film.

Experiment	α_{total} (dB/cm)	α_{scatter} (dB/cm)	$\alpha_{\text{absorption}}$ (dB/cm)
PMMA/C153, TE	23.0 ± 0.2	22.4 ± 0.2	0.67 ± 0.01
PMMA/C153, TM	32.5 ± 0.3	31.5 ± 0.3	0.95 ± 0.01
Bare Waveguide, TE	16.1 ± 0.5	16.1 ± 0.5	0
Bare Waveguide, TM	18.1 ± 0.7	18.1 ± 0.7	0

Table 5.1: Summary of measured and inferred propagation losses caused by scattering and C153 absorption.

The experiments confirm the theoretically predicted relative interaction strength of the TM mode compared to the TE mode with the sample (7.2 dB/cm and 4.4 dB/cm), but the measured interaction is much smaller (0.95 dB/cm and 0.67 dB/cm). The discrepancy comes from the difficulty in modeling the PMMA film parameters, especially the film profile in the vicinity of the waveguide. The PMMA/C153 layer was measured to be 60 nm on average using profilometry, but the film profile is not homogeneously 60 nm thick in the vicinity of the waveguide, as measured by confocal fluorescence microscopy (Appendix D.3). The measured propagation loss could also be underestimated if the assumed dye quantum yield of 90% is too high, which could be the case due to the PMMA microstructure around the dye, quenching of the dye (such as self-quenching by homo-Förster resonance energy transfer), or degradation of the dye. Decreases in the dye cross-section from these effects by up to 50% have been observed in the Coumarin family [32] when dissolved in PMMA. If the dye quantum yield and film non-uniformity are included in the simulations,

the absorption losses can become as low as 0.80 dB/cm for TM and 0.55 dB/cm for TE, close to the experimentally measured values in Table 5.1.

Based on our findings, future work improving TFLN-based evanescent field sensors should focus on decreasing the waveguide scattering loss imparted by the fabrication process and realistic sample interaction layers. Propagation losses of 0.002 dB/cm have been demonstrated in TFLN waveguides with methods such as post-fabrication annealing [33], ion beam milling [34], and redeposition-free etching [27]. Compared to the losses in Table 5.1, such improvements in the scattering loss will increase the fluorescence-to-scatter ratio from the 3% demonstrated here to upwards of 30,000%. A liquid sample with microfluidics will also eliminate much of the uncertainties associated with the polymer film used here.

5.4 Conclusion

TFLN rib waveguides are analyzed for their light-matter interaction strength. The thin-film thickness is found to be the primary variable for increasing the sample interaction. While the fundamental TM mode is predicted to exhibit a two-fold stronger sample interaction, increased scattering losses from the waveguide for the TM mode outweigh this factor. We demonstrate the importance of quantifying different loss mechanisms on the waveguide when measuring a LN sensor's efficacy, which we accomplish by comparing the spatially-resolved intensities of scatter and fluorescence without requiring any knowledge of the actual on-chip pump intensities. The suitability of the TE versus TM mode for sensing has important implications. The main advantage of using TFLN is the integration of a sensor with up- or downstream nonlinear frequency conversion, which utilizes the TE mode in X-cut TFLN to access the highest quadratic nonlinearity. Therefore, a sensor utilizing the TE mode in a rib waveguide is the most compatible with up- or downstream nonlinear frequency conversion. Although a polarization mode converter could be designed to convert between the TE and TM modes, any additional integrated components will likely incur more loss than is gained in interaction strength. Further improvements in the sensor performance, regardless of TE or TM mode, can be achieved with improved fabrication to decrease the scattering loss. Our work thus represents a first step toward fully integrated TFLN sensors.

References

[1] A. Boes, L. Chang, C. Langrock, M. Yu, M. Zhang, Q. Lin, M. Lončar, M. Fejer, J. Bowers, A. Mitchell, *Science* **2023**, *379*, eabj4396.

[2] D. Zhu, L. Shao, M. Yu, R. Cheng, B. Desiatov, C. J. Xin, Y. Hu, J. Holzgrafe, S. Ghosh, A. Shams-Ansari, E. Puma, N. Sinclair, C. Reimer, M. Zhang, M. Lončar, *Advances in Optics and Photonics* **2021**, *13*, 242.

[3] M. Jankowski, C. Langrock, B. Desiatov, A. Marandi, C. Wang, M. Zhang, C. R. Phillips, M. Lončar, M. M. Fejer, *Optica* **2020**, *7*, 40.

[4] L. Ledezma, R. Sekine, Q. Guo, R. Nehra, S. Jahani, A. Marandi, *Optica* **2022**, *9*, 303.

[5] J. Lu, A. A. Sayem, Z. Gong, J. B. Surya, C.-L. Zou, H. X. Tang, *Optica* **2021**, *8*, 539–544.

[6] A. Y. Hwang, H. S. Stokowski, T. Park, M. Jankowski, T. P. McKenna, C. Langrock, J. Mishra, V. Ansari, M. M. Fejer, A. H. Safavi-Naeini, *Optica* **2023**, *10*, 1535–1542.

[7] G.-T. Xue, Y.-F. Niu, X. Liu, J.-C. Duan, W. Chen, Y. Pan, K. Jia, X. Wang, H.-Y. Liu, Y. Zhang, P. Xu, G. Zhao, X. Cai, Y.-X. Gong, X. Hu, Z. Xie, S. Zhu, *Physical Review Applied* **2021**, *15*, 064059.

[8] N. A. Harper, E. Y. Hwang, R. Sekine, L. Ledezma, C. Perez, A. Marandi, S. K. Cushing, *Optica Quantum* **2024**, *2*, 103.

[9] E. Hwang, N. Harper, R. Sekine, L. Ledezma, A. Marandi, S. Cushing, *Optics Letters* **2023**, *48*, 3917.

[10] J. Mishra, T. P. McKenna, E. Ng, H. S. Stokowski, M. Jankowski, C. Langrock, D. Heydari, H. Mabuchi, M. M. Fejer, A. H. Safavi-Naeini, *Optica* **2021**, *8*, 921.

[11] C. Wang, M. Zhang, X. Chen, M. Bertrand, A. Shams-Ansari, S. Chandrasekhar, P. Winzer, M. Lončar, *Nature* **2018**, *562*, 101–104.

[12] S. Xue, Z. Shi, J. Ling, Z. Gao, Q. Hu, K. Zhang, G. Valentine, X. Wu, J. Staffa, U. A. Javid, Q. Lin, *Optica* **2023**, *10*, 125–126.

[13] M. Zhang, B. Buscaino, C. Wang, A. Shams-Ansari, C. Reimer, R. Zhu, J. M. Kahn, M. Lončar, *Nature* **2019**, *568*, 373–377.

[14] A. Shams-Ansari, M. Yu, Z. Chen, C. Reimer, M. Zhang, N. Picqué, M. Lončar, *Communications Physics* **2022**, *5*, 88.

[15] M. Yu, D. Barton III, R. Cheng, C. Reimer, P. Kharel, L. He, L. Shao, D. Zhu, Y. Hu, H. R. Grant, L. Johansson, Y. Okawachi, A. L. Gaeta, M. Zhang, M. Lončar, *Nature* **2022**, *612*, 252–258.

[16] Y. Hu, M. Yu, D. Zhu, N. Sinclair, A. Shams-Ansari, L. Shao, J. Holzgrafe, E. Puma, M. Zhang, M. Lončar, *Nature* **2021**, *599*, 587–593.

[17] D. Pohl, M. Reig Escalé, M. Madi, F. Kaufmann, P. Brotzer, A. Sergeyev, B. Guldimann, P. Giaccari, E. Alberti, U. Meier, R. Grange, *Nature Photonics* **2020**, *14*, 24–29.

[18] A. A. Sayem, R. Cheng, S. Wang, H. X. Tang, *Applied Physics Letters* **2020**, *116*, 151102.

[19] P. Kozma, F. Kehl, E. Ehrentreich-Förster, C. Stamm, F. F. Bier, *Biosensors and Bioelectronics* **2014**, *58*, 287–307.

[20] E. Benito-Peña, M. G. Valdés, B. Glahn-Martínez, M. C. Moreno-Bondi, *Analytica Chimica Acta* **2016**, *943*, Publisher: Elsevier, 17–40.

[21] P. A. Kocheril, K. D. Lenz, D. E. Jacobsen, J. Z. Kubicek-Sutherland, *Frontiers in Sensors* **2022**, *3*, 948466.

[22] Y. Wang, B. Tan, S. Liu, T. Tian, G. Xu, B. Cai, *Sensors and Actuators B: Chemical* **2020**, *306*, 127548.

[23] C. Lavers, K. Itoh, S. Wu, M. Murabayashi, I. Mauchline, G. Stewart, T. Stout, *Sensors and Actuators B: Chemical* **2000**, *69*, 85–95.

[24] D. Yuan, Y. Dong, Y. Liu, T. Li, *Sensors* **2015**, *15*, 21500–21517.

[25] M. Pi, C. Zheng, H. Zhao, Z. Peng, G. Guan, J. Ji, Y. Huang, Y. Min, L. Liang, F. Song, et al., *ACS Nano* **2023**, *17*, 17761–17770.

[26] D. M. Kita, J. Michon, S. G. Johnson, J. Hu, *Optica* **2018**, *5*, 1046–1054.

[27] F. Kaufmann, G. Finco, A. Maeder, R. Grange, *Nanophotonics* **2023**, *12*, 1601–1611.

[28] I. Krasnokutska, J.-L. J. Tambasco, X. Li, A. Peruzzo, *Optics Express* **2018**, *26*, 897–904.

[29] M. Vlk, A. Datta, S. Alberti, H. D. Yallew, V. Mittal, G. S. Murugan, J. Jágerská, *Light: Science & Applications* **2021**, *10*, 26.

[30] M. Rowinska, S. Kelleher, F. Soberon, A. Ricco, S. Daniels, *Journal of Materials Chemistry B* **2015**, *3*, 135–143.

[31] G. Jones, W. Jackson, C. Choi, W. Bergmark, *Journal of Physical Chemistry* **1985**, *89*, 294–300.

[32] J. Donovalová, M. Cigáň, H. Stankovičová, J. Gašpar, M. Danko, A. Gáplovský, P. Hrdlovič, *Molecules* **2012**, *17*, 3259–3276.

[33] A. Shams-Ansari, G. Huang, L. He, Z. Li, J. Holzgrafe, M. Jankowski, M. Churaev, P. Kharel, R. Cheng, D. Zhu, N. Sinclair, B. Desiatov, M. Zhang, T. J. Kippenberg, M. Lončar, *APL Photonics* **2022**, *7*, 081301.

[34] S. Y. Siew, E. J. H. Cheung, H. Liang, A. Bettiol, N. Toyoda, B. Alshehri, E. Dogheche, A. J. Danner, *Optics Express* **2018**, *26*, 4421.

Chapter 6

CASCADED SPONTANEOUS PARAMETRIC DOWNCONVERSION ON THIN-FILM LITHIUM NIOBATE

Multiphoton entanglement is an important resource for applications in quantum communication and computing. Entangled states with more than two photons are typically created using multiple independent spontaneous parametric downconversion (SPDC) emitters and post-selection, which can limit the quantum correlations of the produced states. Here, we propose a device that directly generates entangled photon triplets through cascaded spontaneous parametric downconversion (CSPDC). Previous demonstrations of CSPDC have utilized bulk crystals or ion-diffused large area waveguides, restricting the triplet generation efficiency. By utilizing the TFLN platform, the CSPDC efficiency can be enhanced and the overall device and optical setup can be simplified. The initial device is composed of two equal-length down conversion regions. The effects of dispersion are also explored through the waveguide geometry. Individual down conversion efficiencies of 2.2×10^{10} pairs/s/mW and 1.0×10^{10} pairs/s/mW are measured, resulting in an expected triplet efficiency of 165 triplets/s/mW. Future designs will incorporate adapted poling and pole-after-etch fabrication processes as well as alternate strategies to further increase the CSPDC source efficiency.

6.1 Introduction

Entanglement is one of the fundamental phenomena of quantum mechanics. Spontaneous parametric downconversion (SPDC) has been used for decades to produce photons entangled in various photonic degrees of freedom, serving as a workhorse in emerging quantum optical applications such as quantum computing [1], internet [2], cryptography [3–5], teleportation [6, 7], communication [8], metrology [9, 10], sensing [11, 12], and spectroscopy [13].

In SPDC, a pair of entangled photons are produced from one pump photon, so a single SPDC event creates a two photon entangled state. However, multiphoton entangled states with more than two photons [14], such as GHZ states [15], are of great interest for applications such as quantum secret sharing [16, 17], quantum secure direct communication [18, 19], and boson sampling [20–22]. Entanglement swapping is often utilized to produce multiphoton states through multiple independent SPDC

emitters [23–25]; however, this method requires post-selection to project onto the desired states [26].

An alternative method to produce multiphoton entanglement is through cascaded spontaneous parametric downconversion (CSPDC)[27]. In CSPDC, two successive SPDC events directly create an entangled photon triplet from one pump photon. Since the entangled photons produced through CSPDC are downconverted from a single pump photon and do not require post-selection, the photon triplets exhibit genuine tripartite entanglement and can be used as heralded Bell states [23]. CSPDC has been demonstrated with entanglement across multiple degrees of freedom [28–34]. However, entangled triplet generation efficiencies with CSPDC have remained low to date (<1 Hz/mW) due to the limited single pass efficiency of bulk crystals and ion-diffused waveguides used as the SPDC sources.

Advances in nanophotonic platforms such as thin-film lithium niobate (TFLN) have resulted in significantly more efficient frequency conversion and quantum state generation processes [35–37]. This enhanced efficiency is enabled through the high nonlinearities of lithium niobate [38] as well as the sub-μm^2 modal interaction areas and low material losses [39] of waveguides fabricated on the thin film platform [40, 41]. Recent demonstrations of SPDC in TFLN [42–46] have achieved entangled pair generation efficiencies orders of magnitude greater than the highest performing bulk crystals or large diffused waveguide SPDC sources [47, 48].

Here, we present a device design and preliminary data for CSPDC on the TFLN platform. The CSPDC device consists of a single periodically poled TFLN waveguide (Figure 6.1). The waveguide is comprised of two downconversion regions with individual poling periods to phase match the SPDC processes. The dispersion of the device can be engineered through the waveguide geometry, and the relative efficiencies of the two SPDC downconversion regions can be tailored through the periodically poled lengths. Due to the simplicity of the single-waveguide design, the losses between the two SPDC regions will depend only on the inherent waveguide loss, as opposed to both the source or waveguide loss and the coupling loss present when using two distinct crystals or waveguides. The preliminary results of the device show an efficiency of 2.2×10^{10} pairs/s/mW for the first downconversion region and 1.0×10^{10} pairs/s/mW for the second downconversion region, with a projected triplet efficiency of 165 triplets/s/mW.

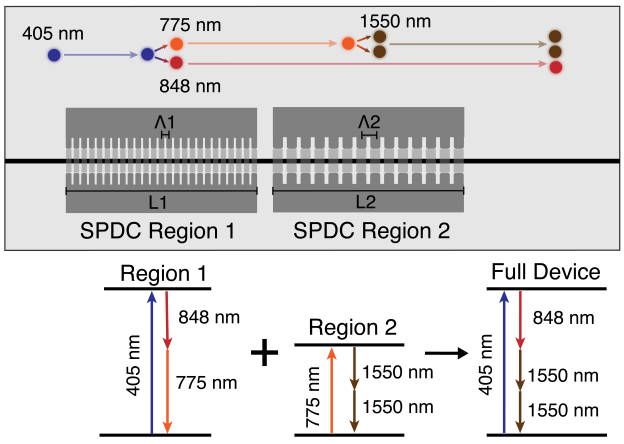

Figure 6.1: Schematic of the proposed TFLN-based CSPDC device (top) and overview of the CSPDC process in a photon picture (bottom). The first down-conversion region (SPDC Region 1) downconverts a 405 nm pump photon into a 775 nm and 848 nm entangled pair and has an associated poling electrode length of $L1$ and poling period of $\Lambda 1$. The second downconversion region (SPDC Region 2) downconverts the 775 nm photon produced from the first downconversion event into a pair of 1550 nm photons and has an associated poling electrode length of $L2$ and poling period of $\Lambda 2$. The end result is that a 405 nm pump photon downconverts into an entangled photon triplet consisting of one 848 nm photon and two 1550 nm photons.

6.2 Device design and fabrication

The periodically poled lithium niobate waveguides were simulated in Lumerical MODE to determine the quasi-phase matching poling periods and target waveguide geometry. The guided modes at the wavelengths of interest (405 nm, 775 nm, 848 nm, 1550 nm) were simulated using the bulk Sellmeier coefficients of 5% MgO-doped lithium niobate [49] and silicon dioxide [50] with the geometric parameters shown in Figure 6.2a. To take advantage of lithium niobate's largest nonlinear coefficient (d_{33} = 28.4 pm/V) [38], only the fundamental quasi-transverse electric (TE) modes of X-cut lithium niobate were considered for quasi-phase matching. The poling period of the first downconversion region was calculated for non-degenerate emission from a pump photon with a wavelength of 405 nm downconverting to photons at 775 nm and 848 nm. The poling period of the second downconversion region was calculated for degenerate emission from a pump photon with a wavelength of 775 nm to a downconverted pair at 1550 nm.

The group velocity dispersion (GVD) and group velocity mismatch (GVM) for the second SPDC process from 775 nm to 1550 nm was also calculated, as shown in

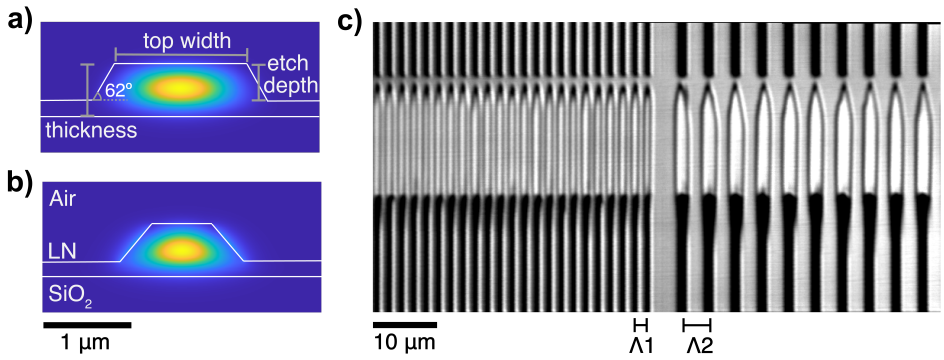

Figure 6.2: Mode profiles of the a) not dispersion engineered waveguide geometry and b) dispersion engineered waveguide geometry at 1550 nm with relevant materials and waveguide geometry parameters indicated. c) The domain inversion for periodic poling of the CSPDC devices was monitored through SHG microscopy, demonstrating the difference in the poling periods (indicated as $\Lambda 1$ and $\Lambda 2$) between the two downconversion regions.

Figure 6.3. Through dispersion engineering, a near-zero GVD or a near-zero GVM enhances the source efficiency by increasing the SPDC bandwidth or by increasing the pump acceptance bandwidth, respectively [51]. Two waveguide geometries were targeted on the same chip to explore the different dispersion regimes (Figure 6.3c). The first geometry targets a low GVD and a low GVM (31 fs^2/mm GVD and -6 fs/mm GVM) with a 0.55 µm top width and 470 nm etch depth (Figure 6.2b), corresponding to poling periods of 1.776 µm for the first downconversion region and 2.8415 µm for the second downconversion region. The second geometry is not dispersion engineered and serves as a control, with a GVD of -54 fs^2/mm) and GVM of 141 fs/mm. Note that the GVD of this second geometry is rather low, which holds true for many waveguides within the range of geometries invested for the source design (Figure 6.3a). The second, non-dispersion engineered geometry has a targeted top width of 1.7 µm and 470 nm etch depth (Figure 6.2a), corresponding to poling periods of 2.035 µm for the first downconversion region and 4.271 µm for the second downconversion region. For film thicknesses of 600 nm, an etch depth greater than 420 nm was chosen to eliminate slab leakage losses at the 405 nm pump wavelength [52].

The devices were fabricated from a 1 cm by 1 cm die of a 5% MgO-doped X-cut thin-film lithium niobate on insulator wafer (NanoLN), which consists of approximately 600 nm of lithium niobate bonded to 2 µm of silicon dioxide on a 0.4 mm silicon substrate. For quasi-phase matching, poling electrodes for the two downconversion

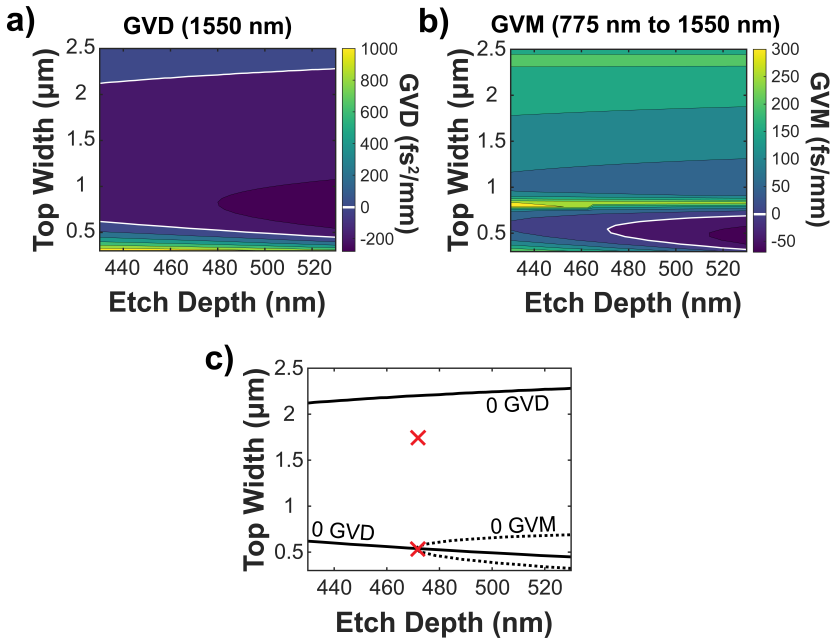

Figure 6.3: Calculated dispersion of the waveguide geometries for the second downconversion region. The a) GVD at 1550 nm and b) GVM between 775 nm and 1550 nm were calculated for waveguide top widths between 0.3 µm and 2.5 µm and waveguide etch depths between 425 nm and 525 nm, with contour lines for the zero GVD and zero GVM geometries marked in solid white. c) The contour lines corresponding to zero GVD (solid) and zero GVM (dashed) are plotted, with the two targeted waveguide geometries marked in red X's.

regions (each 3.5 mm long) were first fabricated by performing a metal lift-off through electron beam lithography with bilayer poly(methyl methacrylate) (PMMA) resist followed by electron beam evaporation of chromium. Periodic poling domain formation was monitored with second harmonic microscopy [53, 54] (Figure 6.2c). After poling, waveguides were defined through aligned electron beam lithography followed by argon inductive coupled plasma reactive ion etching to achieve an etch depth of 500 nm, verified through atomic force microscopy. The chip facets were manually polished to increase coupling efficiency, resulting in a final waveguide length of approximately 8 mm.

6.3 Device characterization and preliminary data

Each downconversion region was individually characterized to verify the quasi-phase matching wavelengths and SPDC efficiencies before characterizing the entangled photon triplet statistics.

First downconversion region (405 nm to 775 nm and 848 nm)

The spectrum and SPDC generation rate of the entangled photon pairs produced from the first downconversion region are characterized as shown in Figure 6.4a-b. A single-frequency tunable Ti:sapphire laser (Spectra-Physics Matisse) frequency doubled with a BBO crystal is used to pump the periodically poled waveguide to produce entangled pairs from the first downconversion region. An antireflection-coated aspheric lens (Thorlabs C140TMD-A) couples the free-space pump beam to the fundamental TE mode of the waveguide. The photon pairs produced in the fundamental TE mode are collected off-chip and collimated using a reflective objective (Thorlabs LMM40X-UVV).

The SPDC spectra were collected to verify the quasi-phase matching and tunability of the downconversion region. SHG measurements with a broadband oscillator were first performed to verify the phase matching wavelengths. Pairs collected from the waveguide were transmitted to a grating spectrometer and measured using an electron-multiplying intensified camera (Figure 6.4a). To tune the SPDC emission and find non-degenerate emission at 775 nm and 848 nm, the pump wavelength was varied from 406.6 nm to 407.1 nm. The resulting SPDC spectra are shown in Figure 6.4c. The behavior of the SPDC spectra with pump wavelength demonstrate the typical regimes of SPDC, with no emission, then degenerate emission, and finally non-degenerate emission as the pump wavelength decreases. A pump wavelength of 406.7 nm was chosen to maximize 775 nm generation for the second downconversion region, indicated by the dotted line in Figure 6.4c. Some losses are present based on dips in the spectra in Figure 6.4c but fall outside the target wavelength range for non-degenerate emission to pump the second downconversion region. A lineout of the resulting spectrum and the corresponding theoretical spectrum are shown in Figure 6.4d. Compared to the theoretical spectrum, the experimental spectrum has multiple weaker satellite peaks in addition to the main SPDC emission peaks. This behavior also manifests as the weaker SPDC signal shifted towards longer pump wavelengths in Figure 6.4c with a similar response to the pump wavelength as the main SPDC spectral peaks. These deviations from theory are likely due to thickness variations along the length of the waveguide, which is discussed further in Section 6.4.

Once the pump wavelength was determined, the pair generation efficiency of the first downconversion was found through coincidence counting with near-IR single photon detectors using the setup in Figure 6.4b. The photon pairs generated from

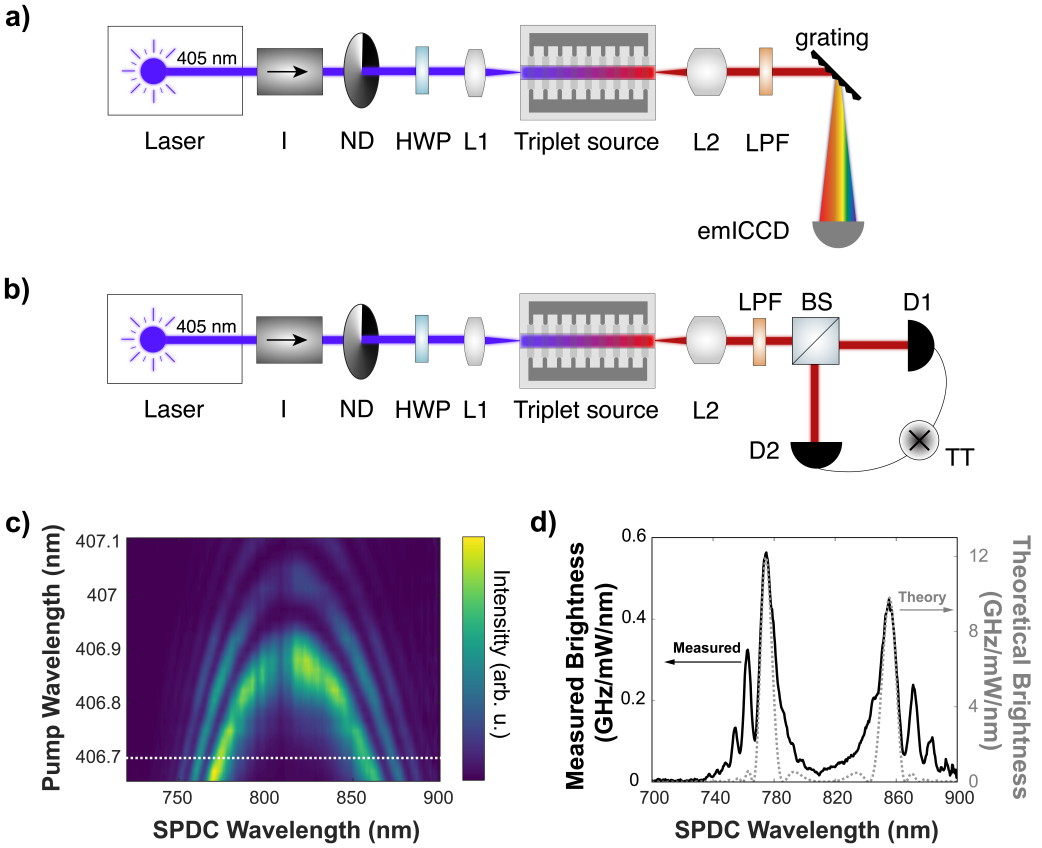

Figure 6.4: Characterization setup for the first downconversion region to measure a) spectra and b) coincidence counts. Acronyms used: I, isolator; ND, neutral density filter; HWP, half-wave plate; L1, aspheric lens; L2, reflective objective; LPF, long-pass filter; emICCD, electron-multiplying intensified charge-coupled device; BS, beamsplitter; D1 and D2, near-IR single-photon avalanche detectors (SPADs); TT, time-tagger. c) Measured experimental SPDC spectra from the first CSPDC downconversion region with the pump wavelength swept from 406.6 nm to 407.1 nm. d) Lineout of the measured SPDC spectrum (solid) and theoretical SPDC spectrum (dashed). The experimental spectrum corresponds to a pump wavelength of 406.7 nm, indicated by the dashed line in c), and was chosen for the demonstrated non-degenerate emission at 775 nm and 848 nm. Note that the frequency bandwidth per nm and the downconversion efficiency are wavelength dependent (Equation 2.51), resulting in higher intensities for shorter wavelengths. The theoretical spectrum in d) was calculated for a single-frequency pump laser and a waveguide without any thickness variations.

the waveguide were coupled to multimode optical fibers (Thorlabs M43L01) and split at a 50:50 broadband multimode fiber beamsplitter (Thorlabs TM105R5F1B) connected to the detectors. Coincidence detection events between two near-IR SPADs (Laser Components Count) were recorded with a time-tagger (Picoquant PicoHarp 300) in the same manner as Chapter 4. From a power sweep of the coincidence counts, the SPDC efficiency was measured as 2.2×10^{10} pairs/s/mW or 1.1×10^{-5} pairs/photon in a per-photon basis. The corresponding theoretical efficiency for the first downconversion region is 2.6×10^{11} pairs/s/mW or 1.3×10^{-4} pairs/photon. To obtain the spectrum with units of brightness (Figure 6.4d), the measured spectrum was integrated over the wavelength range and calibrated using the measured SPDC generation efficiency from coincidence counting and the detector efficiency.

Second downconversion region (775 nm to 1550 nm)

The spectrum and generation rate of the entangled photon pairs produced from the second downconversion region are characterized as shown in Figure 6.5a-b. A single-frequency tunable Ti:sapphire laser (Spectra-Physics Matisse) is used to pump the periodically poled waveguide to produce entangled pairs from the second down-conversion region. An antireflection-coated aspheric lens (Thorlabs C140TMD-B) couples the free-space pump beam to the fundamental TE mode of the waveguide. The photon pairs produced in the fundamental TE mode are collected off-chip and collimated using a reflective objective (Thorlabs LMM40X-UVV).

To verify the quasi-phase matching and tunability of the second downconversion region, coincidence counts and SPDC spectra were collected. To select a quasi-phase matched waveguide, the singles counts were measured with a 30 nm band-pass filter centered at 1556 nm and an IR SPAD. The pump wavelength was swept from 771 nm to 786 nm to measure the single photon counts from degenerate SPDC within the range of the band-pass filter. The waveguide with the singles counts maximized at the center of the range of the band-pass filter (corresponding to a pump wavelength of 778 nm) was chosen for quasi-phase matching. After determining the phase-matched waveguide and pump wavelength, the setup shown in Figure 6.5a was used to collect coincidences. The photons collected from the waveguide were filtered with the 30 nm band-pass filter centered at 1556 nm and with a long-pass filter to block the residual pump. The photon pairs were split at a 50:50 beamsplitter (Thorlabs UFBS50502) and sent to two IR SPADs (ID Quantique ID230). Coincidence detection between the SPADs were recorded with

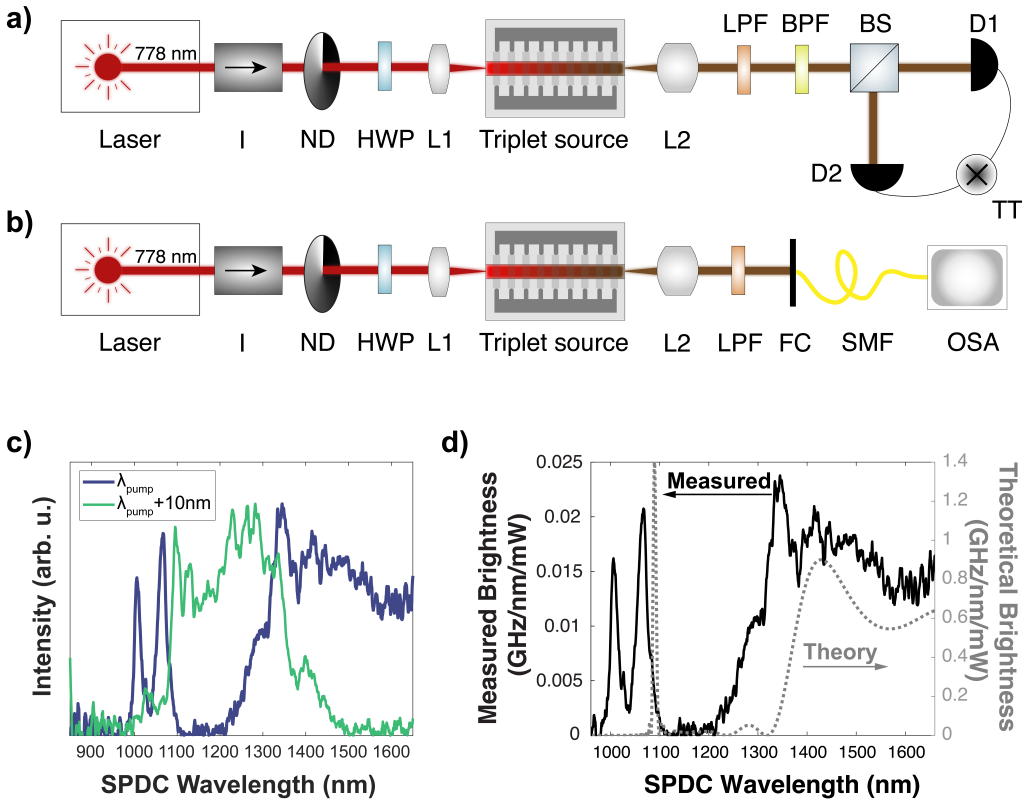

Figure 6.5: Characterization setup for the second downconversion region to measure a) coincidence counts and b) spectra. Acronyms used: I, isolator; ND, neutral density filter; HWP, half-wave plate; L1, aspheric lens; L2, reflective objective; LPF, long-pass filter; BPF, band-pass filter; BS, beamsplitter; D1 and D2, IR SPADs; TT, time-tagger; FC, fiber collimator; SMF, single-mode fiber; OSA, optical spectrum analyzer. c) Measured experimental SPDC spectra from the second CSPDC downconversion region at the pump wavelength (λ_{pump} = 778.112 nm) and with the pump wavelength detuned by 10 nm. d) Comparison of the experimental spectrum (solid) and the theoretical SPDC spectrum (dashed). The theoretical spectrum was calculated for a single-frequency pump laser and a waveguide without any thickness variations.

a time-tagger (Picoquant PicoHarp 300). The input power was swept to determine the pair generation efficiency of the second downconversion region with the band-pass filter, resulting in a filtered on-chip SPDC efficiency of 4.2×10^8 pairs/s/mW. Using the 30 nm bandwidth of the band-pass filter, this efficiency corresponds to an average brightness of 1.5×10^7 pairs/s/mW/nm in the range of the filter.

Once the quasi-phase matched waveguide was determined, spectra were collected using the setup shown in Figure 6.5b. The output of the chip was collected into a single-mode fiber using a fiber collimator and monitored using an optical spectrum analyzer (OSA) (Yokogawa AQ6374). The resulting spectra are shown in Figure 6.5c for the non-dispersion engineered waveguide geometry. The pump wavelength of 778 nm was detuned by 10 nm to verify the SPDC tunability. A lineout of the spectrum measured from the second downconversion region and the corresponding theoretical spectrum are shown in Figure 6.5d. Similarly to the spectra from the first downconversion region, the SPDC spectrum from the second downconversion region shows additional satellite peaks and broadening compared to the theoretical spectrum. These discrepancies are again likely to thickness variations. Due to the wavelength sensitivity of the OSA, the SPDC spectra could not be collected at wavelengths longer than 1650 nm. However, the SPDC bandwidth can be calculated using energy conservation with the onset SPDC wavelength, producing an expected FWHM SPDC bandwidth of 590 nm (1315 to 1905 nm) based on the spectra in Figure 6.5c-d. Using the average brightness of 1.5×10^7 pairs/s/mW/nm measured with the 1541 nm to 1571 nm band-pass filter, the measured spectrum can be scaled for units of brightness. Using the brightness scaling and the calculated bandwidth from energy conservation, the SPDC spectrum can then be integrated to obtain an SPDC efficiency of 1.0×10^{10} pairs/s/mW over the full SPDC bandwidth, or 2.6×10^{-6} pairs/photon. The corresponding theoretical efficiency of the second downconversion region is 2.9×10^{11} pairs/s/mW or 7.4×10^{-5} pairs/photon.

The spectra in Figure 6.5c-d and the 1.0×10^{10} pairs/s/mW measured efficiency correspond to the non-dispersion engineered waveguide geometry. The dispersion engineered geometry was also characterized (Appendix E). However, the brightness of the dispersion engineered waveguide geometry was measured as 5.8×10^6 pairs/s/mW with the 30 nm band-pass filter, which is more than a factor of two lower than the corresponding brightness of 1.5×10^7 pairs/s/mW/nm measured from the non-dispersion engineered waveguides. This reduced performance of the dispersion engineered geometry is likely due to increased propagation loss in

the waveguides due to the smaller top widths required for a near-zero GVM (Figure 6.3b-c). The non-dispersion engineered waveguides on this chip were decided to be more advantageous for triplet measurements due to the decreased brightness and increased loss of the dispersion engineered waveguides. However, as discussed further in Section 6.4, the advantages of the dispersion engineered waveguide geometry could be utilized in future designs if the loss is addressed.

Expected triplet statistics

The entangled photon triplets will be characterized with the setup shown in Figure 6.6. A single-frequency tunable Ti:sapphire laser frequency doubled with a PPLN crystal pumps the periodically poled waveguide at 406.7 nm, which was determined through the characterization of the first downconversion region. An antireflection-coated aspheric lens (Thorlabs C140TMD-A) couples the free-space pump beam to the fundamental TE mode of the waveguide. The photon pairs produced in the fundamental TE mode are collected off-chip and collimated using a reflective objective (Thorlabs LMM40X-UVV). Threefold coincidence counts between one near-IR and two IR SPADs will be taken using a time tagger (Picoquant MultiHarp 150 4P). For maximum heralding efficiency, the 848 nm heralding arm with the near-IR SPAD can be filtered with a monochromator with a 0.1 nm linewidth (WL Photonics WLTF-WM). For maximum triplet generation efficiency, the monochromator can be replaced with a band-pass filter or removed entirely.

If the heralding arm is filtered with a monochromator, the expected triplet rates can be estimated from the individual downconversion efficiencies and brightnesses with the linewidth of the monochromator. Using the peak brightness from the

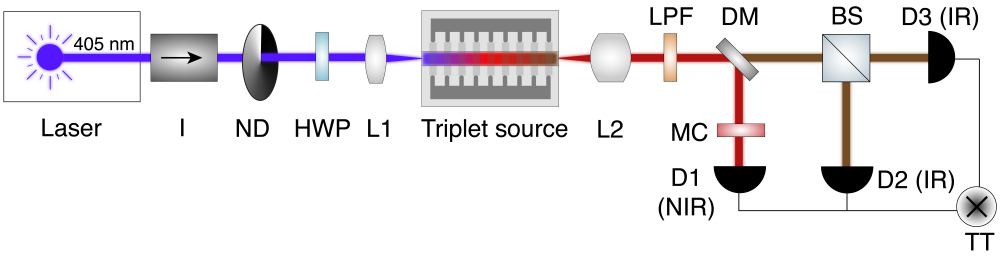

Figure 6.6: Proposed characterization scheme to measure threefold coincidence counts for entangled photon triplets produced through CSPDC. Acronyms used: I, isolator; ND, neutral density filter; HWP, half-wave plate; L1, aspheric lens; L2, reflective objective; LPF, long-pass filter; DM, dichroic mirror; MC, monochromator; BS, beamsplitter; D1, NIR SPAD; D2 and D3, IR SPADs; TT, time-tagger.

first downconversion region at 775 nm as a proxy for the filtered heralding arm, the per-photon efficiency of the second downconversion region, and the relative propagation losses results in an expected triplet efficiency of 165 triplets/s/mW, orders of magnitude higher than the efficiencies from the previous reports of CSPDC (Table 6.1).

Table 6.1: Triplet efficiencies and source types of reported CSPDC sources.

Reference	Region 1 source type	Region 2 source type	Triplet Efficiency (Hz/mW)
[28]	bulk PPKTP	ion-diffused LN	0.0005
[29]	bulk PPKTP	ion-diffused LN	0.0002
[30]	bulk PPKTP	ion-diffused LN	0.007
[31]	ion-diffused LN	ion-diffused LN	0.08
[32]	bulk PPKTP	ion-diffused LN	0.001
[33]	bulk PPKTP	ion-diffused LN	0.0002
[34]	bulk PPKTP	ion-diffused LN	0.003
This work	TFLN	TFLN	165

As with the previous demonstrations of CSPDC, the challenges in measuring triplets include the on- and off-chip losses and the triplet detection. Since CSPDC relies on two subsequent but inefficient downconversion events to occur and because a triplet detection even requires all three photons to arrive at the detectors, measurements of CSPDC triplets will be particularly sensitive to losses present in the waveguide or setup. To characterize the losses in the waveguides, the coupling and propagation losses at the pump wavelengths of each downconversion region were measured through transmission testing and Fabry-Perot interferometry. For a 405 nm pump, the coupling efficiency was 4.9 dB/facet and the upper limit of the propagation loss was estimated as 8.1 dB/cm. For a 775 nm pump, the coupling efficiency was 3.9 dB/facet and the upper limit of the propagation loss was 3.8 dB/cm. The loss from the external optics in the setup was estimated as 1.2 dB. From the total loss implied by the singles and coincidence counts, the collection efficiency from the chip is estimated to be 11.9 dB. Improved collection efficiencies could be realized with non-reflective high-NA objectives, at the expense of chromatic aberration.

The performance of the detectors also impact the measurement of threefold coincidence counts. Deadtime artifacts, which can arise from a triplet arriving within the detector deadtime from a previous detection event of an uncorrelated photon, can result in "true" triplet coincidences being represented as an accidental coincidences.

For SPDC and other second order processes, the integration times and input powers can be increased to boost the coincidence signal and compensate for both loss and deadtime artifacts. However, due to the cascaded nature of CSPDC, the beam out of the waveguide will have significantly more photons from SPDC produced from the first downconversion region compared to the contribution from the second downconversion region. Thus, the near-IR SPAD will saturate at lower powers compared to the IR SPADs, limiting the maximum input power into the waveguides.

6.4 Future work

Once threefold coincidences are measured, future work can be done in optimizing the CSPDC sources.

Fabrication optimization

As described in Section 6.3, the performance of both downconversion regions demonstrate deviations from the theory, particularly in terms of the broadened bandwidth, additional peaks, and lowered brightness and efficiencies. These deviations are likely due to thickness variations along the length of the waveguide [55, 56]. Approximating the thickness variations with a $1/f$ noise model (Figure 6.7b), a spread in thickness of approximately 4 nm can reproduce the behavior of the experimental spectrum (Figure 6.7a). To maximize the CSPDC efficiency, the bandwidth

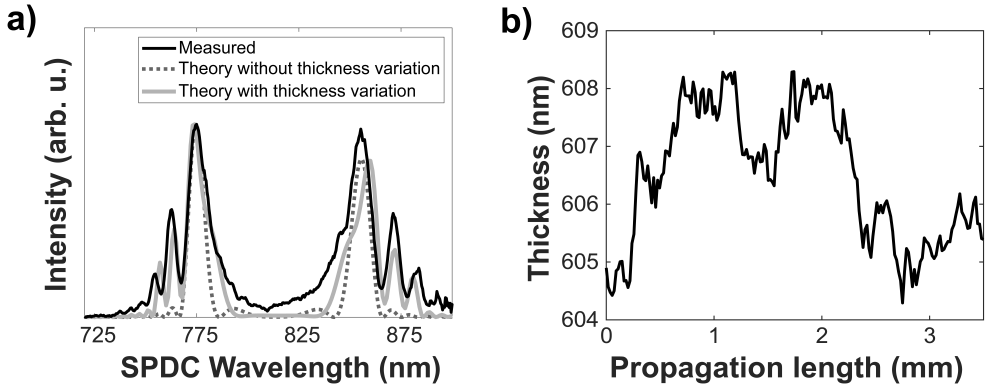

Figure 6.7: Thickness variation effects on the first downconversion region. a) Spectra demonstrating the effects of thickness variations in the first downconversion region. The experimentally measured spectrum (solid, black) demonstrates multiple peaks that are not expected in the theoretical spectrum without any index variations (gray, dashed). The features of the experimental spectrum can be encapsulated if thickness variations are incorporated (gray, solid). b) The corresponding thickness profile has a thickness spread of 4 nm.

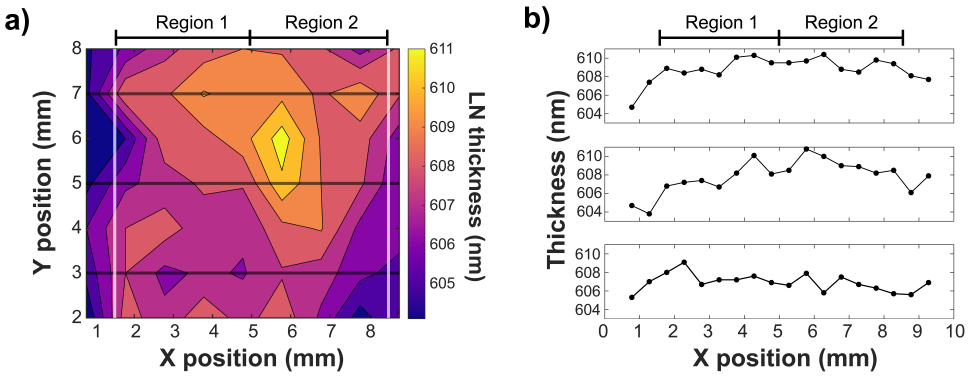

Figure 6.8: Lithium niobate film thickness mapping for adapted poling. a) Thickness map for a TFLN die. Thickness measurements are taken by fitting the reflection spectra from a white light source using thin-film interference. Vertical lines denote the periodic poling electrode region. b) Lineouts of the TFLN thickness corresponding to the horizontal black lines in a).

of the SPDC from the first downconversion region should be designed to be equal to the phase-matching acceptance bandwidth of the second downconversion region. Engineering the bandwidths of the two regions is difficult to design or predict in the presence of such spectral artifacts from thickness variations.

An adapted poling method could be incorporated to address the spectral features from variations in the film thickness [57]. In conventional poling, the poling period is calculated assuming that the film thickness is a constant value. In adapted poling, the thickness of the lithium niobate film is mapped across the chip and the poling periods are calculated for a particular area from the map, gradually changing across the length of the electrode to phase match the measured thickness in each region of the chip. With this type of poling, the full length of the electrodes is utilized for phase-matching, thus maximizing the efficiency and brightness while also eliminating the additional features seen in Figure 6.4c and 6.7a. An example thickness map for adapted poling is shown in Figure 6.8. Thicknesses were measured by illuminating a TFLN chip with a white light source and fitting the resulting reflection spectrum for thin film interference of lithium niobate. The poling periods are then fit to the the lithium niobate film thicknesses to translate the thickness map to a poling period map. Thus, the CSPDC efficiency and spectra can be improved by incorporating adapted poling.

The waveguide propagation loss should also be improved, particularly to realize the enhanced efficiencies of the dispersion engineered waveguide geometry. The

waveguide etching and redeposition removal steps in the fabrication process impart sidewall roughness and corrugations from the periodically poled inverted domains, increasing the propagation losses of the waveguides. Although the roughness and corrugations are present in any periodically poled waveguide fabricated with the conventional TFLN process, waveguides with smaller top widths are more impacted by the increased scattering due to the greater contribution of the electric field at the sidewalls from the tighter confinement area of the modes.

The roughness and scattering imparted by the fabrication can potentially be reduced with a pole-after-etch approach [58] with post-etch annealing [39]. As opposed to the conventional pole-before-etch process, this process would involve first etching the waveguides, annealing to reduce roughness and loss, and poling the already-etched waveguides. A limitation in this process is in achieving the same domain inversion depth as conventional processing, as it can be difficult to pole the full thickness of the waveguides after etching. However, recent implementations of sidewall poling have shown enhanced efficiencies [59], demonstrating the full capability and potential of this process.

CSPDC source design

In addition to fabrication and processing improvements, the CSPDC source design can also be optimized to increase the efficiency.

Because the SPDC efficiency increases with the periodic poling electrode length (Equation 2.51), a straightforward approach to increase the CSPDC efficiency is to increase the length of the downconversion regions. A single straight waveguide design, as fabricated in the device characterized in Section 6.3, is limited by the linear dimensions of the TFLN chips. By incorporating a meander, a single waveguide can traverse multiple downconversion regions without requiring very large chips or wafer scale fabrication (Figure 6.9a). Furthermore, as described in Section 6.3, the cascaded nature of CSPDC makes the photon stream out of the waveguide have a significant higher contribution from the first downconversion region and a much weaker contribution from the second downconversion region, restricting the input power due to the saturation of the near-IR detector. By optimizing the downconversion region lengths, the relative efficiency of the second downconversion region can be increased to make the photon stream more balanced, addressing the detector saturation and making the triplet measurements more feasible. Due to the increased length, this meandered approach will be particularly sensitive to thickness

variations, fabrication imperfections, and loss. Long downconversion region lengths will also have a tradeoff between the length, SPDC bandwidth, pump acceptance bandwidth, and heralding efficiency. The meander will also likely restrict the number of devices able to be fabricated onto a single chip. However, this approach benefits from the simplicity in scaling of both the device footprint and the efficiency.

Another alternate design to increase the CSPDC efficiency is to incorporate an on-chip cavity to increase the effective path length. In this design, a singly-resonant optical parametric oscillator (OPO) will resonate the 775 nm photons to more efficiently pump the second downconversion region (Figure 6.9b). The cavity and the cavity couplers will likely be challenging in both design and fabrication compared to the simple meander. The input coupler will need to efficiently couple the 405 nm pump; however, the small waveguide top widths and coupler distances required to couple shorter wavelength photons make the fabrication of the input coupler difficult. Similarly, the output coupler needs to behave as a dichroic beamsplitter with a cutoff wavelength between 775 nm and 848 nm. This coupler should not

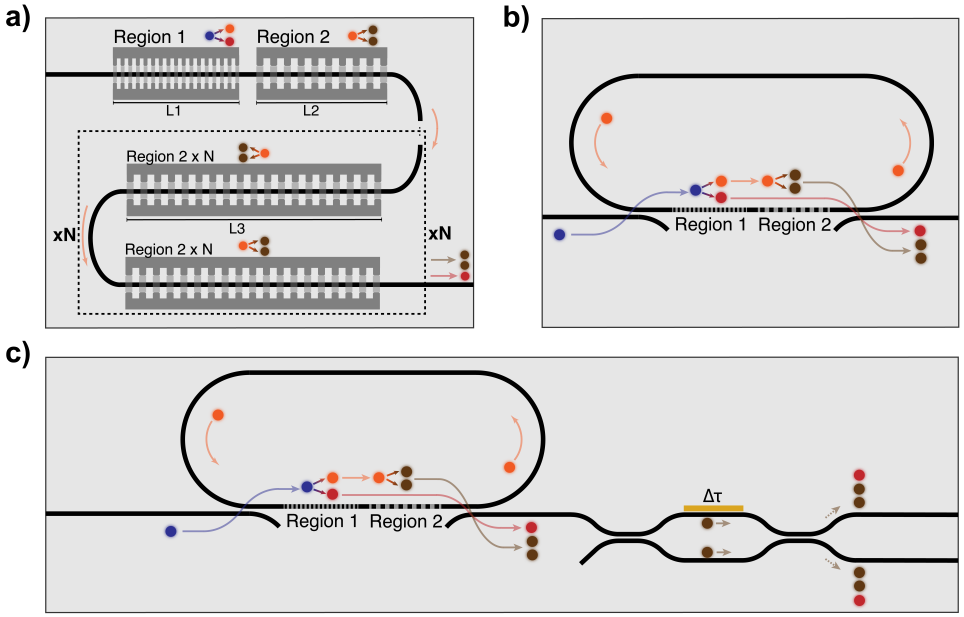

Figure 6.9: Proposed designs to increase the efficiency of CSPDC in periodically poled TFLN waveguides. a) Schematic to increase the length of the second down-conversion regions through a waveguide meander. b) Schematic to singly-resonate the 775 nm light in an optical cavity. c) Downstream circuitry such as polarization converters or Mach-Zehnder interferometers can be integrated with the CSPDC source for quantum state manipulation.

couple any 775 nm photons so that they can circulate in the cavity, but it should efficiently couple 848 nm and 1550 nm photons so that they can be collected off-chip for the triplet detection, requiring careful design to target the specific wavelengths of interest. Though the design and fabrication of a CSPDC OPO will be challenging, a cavity-based design will not be restricted by the increasing footprint or linear efficiency scaling with length of the meander-based design and thus can potentially remain in a compact form factor with significantly increased CSPDC efficiency.

Additional downstream optics can also be incorporated with the CSPDC source to manipulate the quantum state (Figure 6.9c). Passive components such as tapered couplers can be implemented to increase the on- and off-chip coupling efficiencies of the pump and triplet photons. A Mach-Zehnder interferometer (MZI) with electro-optic modulators or thermo-optic heaters can be implemented downstream to incorporate a tunable phase shift between the CSPDC photons and impart interference fringes. A combination of MZIs, couplers, and polarization converters can be implemented with the CSPDC sources to impart path or polarization entanglement. These upstream and downstream photonic components will likely require even more complexity in the design and device fabrication, but the incorporation of these components demonstrates the full capabilities of the TFLN platform, with frequency conversion, passive components, and state manipulation all incorporated as a compact photonic integrated circuit.

6.5 Outlook

In conclusion, a design for CSPDC in periodically poled TFLN waveguides is proposed. Preliminary characterization of the individual downconversion regions demonstrates SPDC efficiencies of 2.2×10^{10} pairs/s/mW and 1.0×10^{10} pairs/s/mW, resulting in an expected triplet generation rate of 165 triplets/s/mW. The fabrication can be further improved to decrease the effects of thickness variations and the propagation loss through adapted poling and pole-after-etch approaches. Finally, further designs to optimize the CSPDC efficiency and quantum state through increased downconversion region lengths, on-chip cavities, and downstream state manipulation are presented.

References

[1] J. L. O'Brien, *Science* **2007**, *318*, 1567–1570.

[2] H. J. Kimble, *Nature* **2008**, *453*, 1023–1030.

[3] A. K. Ekert, *Physical Review Letters* **1991**, *67*, 661–663.

[4] M. Erhard, M. Krenn, A. Zeilinger, *Nature Reviews Physics* **2020**, *2*, 365–381.

[5] C. H. Bennett, G. Brassard, *Theoretical Computer Science* **2014**, *560*, 7–11.

[6] D. Bouwmeester, J.-W. Pan, K. Mattle, M. Eibl, H. Weinfurter, A. Zeilinger, *Nature* **1997**, *390*, 575–579.

[7] C. H. Bennett, G. Brassard, C. Crépeau, R. Jozsa, A. Peres, W. K. Wootters, *Physical Review Letters* **1993**, *70*, 1895–1899.

[8] N. Gisin, R. Thew, *Nature Photonics* **2007**, *1*, 165–171.

[9] V. Giovannetti, S. Lloyd, L. Maccone, *Nature Photonics* **2011**, *5*, 222–229.

[10] J. Huang, M. Zhuang, C. Lee, *Applied Physics Reviews* **2024**, *11*, 031302.

[11] S. Pirandola, B. R. Bardhan, T. Gehring, C. Weedbrook, S. Lloyd, *Nature Photonics* **2018**, *12*, 724–733.

[12] C. L. Degen, F. Reinhard, P. Cappellaro, *Reviews of Modern Physics* **2017**, *89*, 035002.

[13] K. E. Dorfman, F. Schlawin, S. Mukamel, *Reviews of Modern Physics* **2016**, *88*, 045008.

[14] J.-W. Pan, Z.-B. Chen, C.-Y. Lu, H. Weinfurter, A. Zeilinger, M. Żukowski, *Reviews of Modern Physics* **2012**, *84*, 777–838.

[15] D. Bouwmeester, J.-W. Pan, M. Daniell, H. Weinfurter, A. Zeilinger, *Physical Review Letters* **1999**, *82*, 1345–1349.

[16] M. Hillery, V. Bužek, A. Berthiaume, *Physical Review A* **1999**, *59*, 1829–1834.

[17] L. Xiao, G. Lu Long, F.-G. Deng, J.-W. Pan, *Physical Review A* **2004**, *69*, 052307.

[18] G. L. Long, X. S. Liu, *Physical Review A* **2002**, *65*, 032302.

[19] K. Boström, T. Felbinger, *Physical Review Letters* **2002**, *89*, 187902.

[20] J. B. Spring, B. J. Metcalf, P. C. Humphreys, W. S. Kolthammer, X.-M. Jin, M. Barbieri, A. Datta, N. Thomas-Peter, N. K. Langford, D. Kundys, J. C. Gates, B. J. Smith, P. G. R. Smith, I. A. Walmsley, *Science* **2013**, *339*, 798–801.

[21] M. Tillmann, B. Dakić, R. Heilmann, S. Nolte, A. Szameit, P. Walther, *Nature Photonics* **2013**, *7*, 540–544.

[22] H.-S. Zhong et al., *Science* **2020**, *370*, 1460–1463.

[23] M. Żukowski, A. Zeilinger, M. A. Horne, A. K. Ekert, *Physical Review Letters* **1993**, *71*, 4287–4290.

[24] S. Bose, V. Vedral, P. L. Knight, *Physical Review A* **1998**, *57*, 822–829.

[25] J.-W. Pan, D. Bouwmeester, H. Weinfurter, A. Zeilinger, *Physical Review Letters* **1998**, *80*, 3891–3894.

[26] A. Zeilinger, M. A. Horne, H. Weinfurter, M. Żukowski, *Physical Review Letters* **1997**, *78*, 3031–3034.

[27] D. M. Greenberger, M. A. Horne, A. Shimony, A. Zeilinger, *American Journal of Physics* **1990**, *58*, 1131–1143.

[28] H. Hübel, D. R. Hamel, A. Fedrizzi, S. Ramelow, K. J. Resch, T. Jennewein, *Nature* **2010**, *466*, 601–603.

[29] L. K. Shalm, D. R. Hamel, Z. Yan, C. Simon, K. J. Resch, T. Jennewein, *Nature Physics* **2013**, *9*, 19–22.

[30] D. R. Hamel, L. K. Shalm, H. Hübel, A. J. Miller, F. Marsili, V. B. Verma, R. P. Mirin, S. W. Nam, K. J. Resch, T. Jennewein, *Nature Photonics* **2014**, *8*, 801–807.

[31] S. Krapick, B. Brecht, H. Herrmann, V. Quiring, C. Silberhorn, *Optics Express* **2016**, *24*, 2836.

[32] S. Agne, T. Kauten, J. Jin, E. Meyer-Scott, J. Z. Salvail, D. R. Hamel, K. J. Resch, G. Weihs, T. Jennewein, *Physical Review Letters* **2017**, *118*, 153602.

[33] Z. M. E. Chaisson, P. F. Poitras, M. Richard, Y. Castonguay-Page, P.-H. Glinel, V. Landry, D. R. Hamel, *Physical Review A* **2022**, *105*, 063705.

[34] A. Z. Leger, S. Gambhir, J. Légère, D. R. Hamel, *Physical Review Research* **2023**, *5*, 023131.

[35] M. Jankowski, C. Langrock, B. Desiatov, A. Marandi, C. Wang, M. Zhang, C. R. Phillips, M. Lončar, M. M. Fejer, *Optica* **2020**, *7*, 40.

[36] C. Wang, C. Langrock, A. Marandi, M. Jankowski, M. Zhang, B. Desiatov, M. M. Fejer, M. Lončar, *Optica* **2018**, *5*, 1438.

[37] R. Nehra, R. Sekine, L. Ledezma, Q. Guo, R. M. Gray, A. Roy, A. Marandi, *Science* **2022**, *377*, 1333–1337.

[38] I. Shoji, T. Kondo, A. Kitamoto, M. Shirane, R. Ito, *Journal of the Optical Society of America B* **1997**, *14*, 2268.

[39] A. Shams-Ansari, G. Huang, L. He, Z. Li, J. Holzgrafe, M. Jankowski, M. Churaev, P. Kharel, R. Cheng, D. Zhu, N. Sinclair, B. Desiatov, M. Zhang, T. J. Kippenberg, M. Lončar, *APL Photonics* **2022**, *7*, 081301.

[40] A. Boes, L. Chang, C. Langrock, M. Yu, M. Zhang, Q. Lin, M. Lončar, M. Fejer, J. Bowers, A. Mitchell, *Science* **2023**, *379*, eabj4396.

[41] D. Zhu, L. Shao, M. Yu, R. Cheng, B. Desiatov, C. J. Xin, Y. Hu, J. Holzgrafe, S. Ghosh, A. Shams-Ansari, E. Puma, N. Sinclair, C. Reimer, M. Zhang, M. Lončar, *Advances in Optics and Photonics* **2021**, *13*, 242.

[42] J. Zhao, C. Ma, M. Rüsing, S. Mookherjea, *Physical Review Letters* **2020**, *124*, 163603.

[43] U. A. Javid, J. Ling, J. Staffa, M. Li, Y. He, Q. Lin, *Physical Review Letters* **2021**, *127*, 183601.

[44] G.-T. Xue, Y.-F. Niu, X. Liu, J.-C. Duan, W. Chen, Y. Pan, K. Jia, X. Wang, H.-Y. Liu, Y. Zhang, P. Xu, G. Zhao, X. Cai, Y.-X. Gong, X. Hu, Z. Xie, S. Zhu, *Physical Review Applied* **2021**, *15*, 064059.

[45] Y. Zhang, H. Li, T. Ding, H. Yiwen, L. Liang, X. Sun, Y. Tang, J. Wang, S. Liu, Y. Zheng, X. Chen, *Optica* **2023**, *10*, 688–693.

[46] N. A. Harper, E. Y. Hwang, R. Sekine, L. Ledezma, C. Perez, A. Marandi, S. K. Cushing, *Optica Quantum* **2024**, *2*, 103.

[47] B. Dayan, A. Pe'er, A. A. Friesem, Y. Silberberg, *Physical Review Letters* **2005**, *94*, 043602.

[48] M. Bock, A. Lenhard, C. Chunnilall, C. Becher, *Optics Express* **2016**, *24*, 23992.

[49] O. Gayer, Z. Sacks, E. Galun, A. Arie, *Applied Physics B* **2008**, *91*, 343–348.

[50] T. Toyoda, M. Yabe, *Journal of Physics D: Applied Physics* **1983**, *16*, L97–L100.

[51] L. Ledezma, R. Sekine, Q. Guo, R. Nehra, S. Jahani, A. Marandi, *Optica* **2022**, *9*, 303.

[52] A. Boes, L. Chang, T. Nguyen, G. Ren, J. Bowers, A. Mitchell, *Journal of Physics: Photonics* **2021**, *3*, 012008.

[53] M. Rüsing, J. Zhao, S. Mookherjea, *Journal of Applied Physics* **2019**, *126*, 114105.

[54] S. Reitzig, M. Rüsing, J. Zhao, B. Kirbus, S. Mookherjea, L. M. Eng, *Crystals* **2021**, *11*, 288.

[55] M. Santandrea, M. Stefszky, V. Ansari, C. Silberhorn, *New Journal of Physics* **2019**, *21*, 033038.

[56] G.-T. Xue, X.-H. Tian, C. Zhang, Z. Xie, P. Xu, Y.-X. Gong, S.-N. Zhu, *Chinese Physics B* **2021**, *30*, 110313.

[57] P.-K. Chen, I. Briggs, C. Cui, L. Zhang, M. Shah, L. Fan, *Nature Nanotechnology* **2024**, *19*, 44–50.

[58] C. J. Xin, S. Lu, J. Yang, A. Shams-Ansari, B. Desiatov, L. S. Magalhães, S. S. Ghosh, E. McGee, D. Renaud, N. Achuthan, A. Zvyagintsev, D. Barton III, N. Sinclair, M. Lončar, *Communications Physics* **2025**, *8*, 136.

[59] C. A. A. Franken, S. S. Ghosh, C. C. Rodrigues, J. Yang, C. J. Xin, S. Lu, D. Witt, G. Joe, G. S. Wiederhecker, K.-J. Boller, M. Lončar, **2025**, arXiv preprint arXiv:2503.16785 [physics.optics].

Chapter 7

CONCLUSION AND FUTURE DIRECTIONS

Integrated frequency conversion and quantum light sources are becoming increasingly popular for applications in spectroscopy, microscopy, and sensing for their high efficiencies and compact footprints. The growing field of lithium niobate nanophotonics has enabled frequency conversion, quantum state generation, sample interaction, and state manipulation all inline in a single device. This thesis has extended the wavelength range of nonlinear frequency conversion in thin-film lithium niobate from the more established infrared wavelengths to the ultraviolet through telecom wavelengths that are of interest for spectroscopy. The work presented here lays the groundwork for integrated, compact, entangled photon spectrometers. Three promising future research directions to extend the work in this thesis include incorporating further downstream components to fully realize on-chip spectrometers, improving the fabrication process to address the thickness variations and loss, and exploring material platforms other than lithium niobate to push deeper into the ultraviolet region.

7.1 Towards integrated spectrometers

This work has mainly focused on frequency conversion and entangled photon generation sources in periodically poled lithium niobate waveguides, demonstrating the potential for integrated entangled photon-based spectrometers on the TFLN platform. However, work still needs to be done to benchmark and incorporate photonic components other than the entangled photon source, such as a sample interaction region, pump filter, and interferometer (Figure 7.1).

Engineered Sample Interactions

The rib waveguide-fluorescent dye system presented in Chapter 5 represents a first attempt at a simple sample interaction on the TFLN platform. Future designs can engineer the interaction region to have a more localized sample region and a stronger overlap between the waveguide mode and the sample, such as slot waveguide geometries [1] or microfluidics-based sample delivery systems [2]. A tradeoff between a higher sample-waveguide mode overlap and excess loss from scattering will likely be a concern for such designs and will need to be carefully characterized.

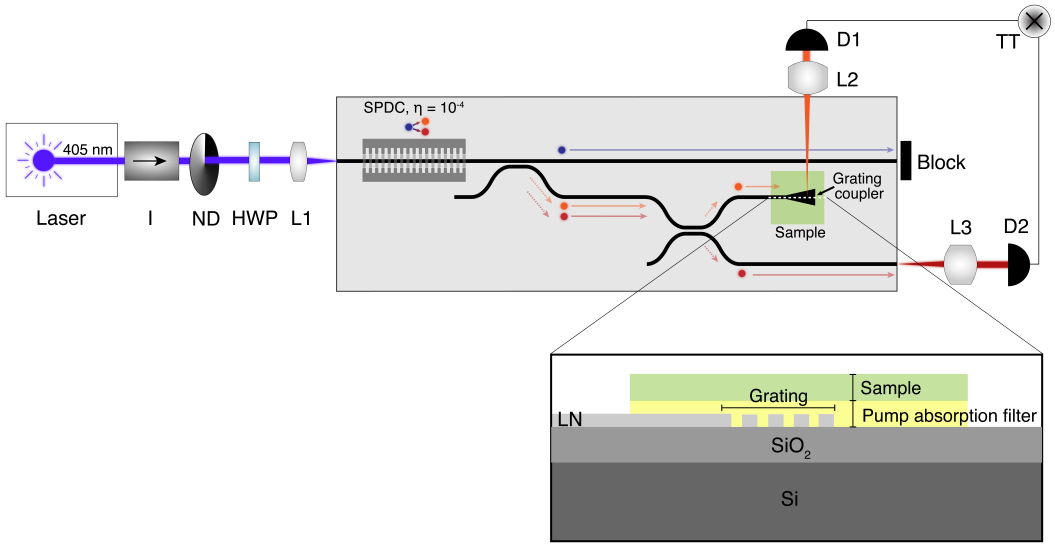

Figure 7.1: Example schematic of a TFLN device for time-resolved fluorescence measurements. A grating coupler geometry is used to interact the entangled photons with a surface-cladded sample. Both spatial- and absorption-based filtering of the pump is utilized. Acronyms used: I, isolator; ND, neutral-density filter; HWP, half-wave plate; L1, aspheric lens; L2 and L3, reflective objective; D1 and D2, near-IR SPADs; TT, time tagger.

One potential sample geometry would be to maintain the surface-cladded sample in Chapter 5, but change the interaction region from the evanescent mode-based rib waveguide to a grating coupler (Figure 7.1). The coupler will require additional and more complex simulations with a finite-difference time-domain (FDTD) solver to ensure that the mode can be efficiently collected with and without the sample, and the fabrication may be difficult depending on the grating period. However, the strength of the sample-mode interaction will likely be increased since the full SPDC beam will be forced to interact with the sample as it is coupled out of the waveguide, compared to the sample only interacting with the SPDC mode at the surface of the waveguide in Chapter 5.

Pump Filtering

Filtering is an integral part of an entangled photon-based spectrometer. For sample excited using SPDC, filtering out any residual pump illumination is integral to ensure that any sample response originates from the entangled photons instead of the pump [3, 4]. Thus, an inline pump rejection filter is essential for any integrated spectrometers with both on-chip entangled photon pair generation and on-chip sample interactions.

TFLN filters have been demonstrated in resonator- [5, 6], grating- [7, 8], and adiabatic coupler- [9, 10] based designs. However, the target wavelengths of these filters have largely been near-infrared and telecom (775 to 1550 nm) wavelengths. These designs will need to be adapted for the 405 nm pump wavelengths used for SPDC in this work. The stringent device requirements for shorter wavelengths may push the required device tolerances to the limits of current TFLN fabrication, particularly the waveguide top widths, grating periods, and coupling distances depending on the filter design of choice. Furthermore, spectroscopy with SPDC requires heavy pump filtering of at least two orders of magnitude greater than the SPDC efficiency, so an inline filter will require a 10^{-6} pump rejection ratio (60 dB) for the 10^{-4} pairs/photon SPDC efficiency in Chapter 4, while maintaining low losses at the SPDC wavelengths. This high rejection ratio means that multiple inline filters will likely be required for adequate pump filtering. On-chip pump filtering on TFLN will likely be a significant design and fabrication challenge for integrated entangled photon spectrometers.

Interferometers and Phase Shifters

Downstream state manipulation elements also need to be incorporated for on-chip spectroscopy. Free-space interferometers such as Mach-Zehnder interferometers (MZIs) have analogous waveguided structures, although the beamsplitters will need to be adapted for the shorter wavelengths used in this work. To apply time delays, phase shifts can be incorporated through thermo-optic [11] or electro-optic [12] modulators. Electro-optic modulators in particular are of great interest to the TFLN community and have been demonstrated at CMOS-compatible voltages [13] on TFLN at wavelengths near the ones used in this work [14].

7.2 Fabrication improvements

To improve the device performance, the current fabrication process (Appendix B) could be changed to address the thickness variations and propagation losses present in the devices presented in this work.

As demonstrated by the devices in Chapters 3 and 6, thickness variations in the TFLN thicknesses can greatly impact the spectra for both SHG and SPDC. These thickness variations were also likely present in the visible through near-IR SPDC device presented in Chapter 4, but may have been obscured by the multimode pump laser. An adapted poling method can be incorporated the spectral features induced by the thickness variations [15]. Compared to the conventional poling process,

which calculates a single poling period for the entire electrode length assuming that the film thickness is constant, with adapted poling, the period is varied across the length of the electrodes according to the mapped thickness of the lithium niobate film. With this type of poling, the full length of the electrodes is utilized for phase-matching, thus maximizing the efficiency and brightness while also eliminating the unwanted spectral features that are imparted by the varying film thickness.

The propagation losses measured in the devices presented here, particularly in Chapter 5 and Chapter 6, are also considerably higher than the current state-of-the-art of approximately 0.2 dB/m [16]. These high losses are likely due to the waveguide etching and redeposition removal processes during fabrication, which impart sidewall roughness from micro-masking and corrugations from the different etch rates of the $+z$ and $-z$ planes of lithium niobate [17]. The increased loss in conventionally fabricated periodically poled LN waveguides can potentially be reduced with a pole-after etch-approach [18]. As opposed to the conventional process, which consists of poling before etching, with an etch-before-pole approach, the waveguides are first etched and annealed to reduce roughness and loss [16], then poled as the final step. The domain inversion depth with this process can be limited compared to the conventional processing, since it can be difficult to pole the full height and thickness of the waveguides after etching. However, recent implementations of sidewall poling have shown enhanced efficiencies and poling depths equivalent to conventionally-fabricated devices [19].

The adapted poling and pole-before-etch methods are mutually compatible and can be incorporated simultaneously. Improving the poling quality and reducing the propagation loss through the incorporation of both of these processes has been shown to greatly enhance the efficiency for ultraviolet generation [19] and would likely similarly enhance the performances of the devices presented throughout this work.

7.3 Ultraviolet nonlinear materials

Although the focus of this work has been lithium niobate, the number and variety of nonlinear optical platforms continues to grow thanks to innovations in crystal and thin film growth. To enable higher energy sample excitations, such as semiconductor electronic transitions, and for greater wavelength spread and tunability to multiplex samples, the frequency conversion sources presented here can be extended further towards the ultraviolet region. Although lithium niobate can be pushed further

towards its band gap around 326 nm [20], two optical materials of interest that can go even further into the UV are LBGO and lithium tantalate.

As a UV optical platform, LBGO ($LaBGeO_5$) [21] has potential due to its ferroelectricity and 195 nm bandgap, enabling downconversion centered at 532 nm with a 266 nm pump laser, though it suffers from a low second order nonlinearity (d_{22} = 1.41 pm/V and d_{33} = 1.15 pm/V at 532 nm) [22, 23]. However, LGBO has yet to be implemented in a thin-film platform or even as large-area micromachined waveguides, restricting its current applications to UV downconversion with bulk crystals.

Lithium tantalate (LT, $LiTaO_3$) is another material with promising properties at ultraviolet wavelengths. LT has a very similar crystal structure and nonlinear properties to lithium niobate but with a band gap of approximately 280 nm, enabling even shorter wavelength conversion. LT has a lower second order nonlinearity (d_{33}=10.6 pm/V) [24] and lower Curie temperature (660°C) [25] but higher power handling and optical damage threshold [26] compared to LN. Furthermore, unlike LBGO, LT has been implemented in a thin film platform, with periodic poling [27], waveguided frequency conversion sources [28, 29], low loss waveguides [25], and electro-optic modulation [30] recently demonstrated. With these UV material platforms, future integrated devices can continue to push towards shorter wavelengths for integrated UV through IR spectroscopy.

References

[1] D. M. Kita, J. Michon, S. G. Johnson, J. Hu, *Optica* **2018**, *5*, 1046–1054.

[2] R. Zamboni, L. Gauthier-Manuel, A. Zaltron, L. Lucchetti, M. Chauvet, C. Sada, *Optics Express* **2023**, *31*, 28423.

[3] T. Landes, M. G. Raymer, M. Allgaier, S. Merkouche, B. J. Smith, A. H. Marcus, *Optics Express* **2021**, *29*, 20022.

[4] M. He, B. P. Hickam, N. Harper, S. K. Cushing, *The Journal of Chemical Physics* **2024**, *160*, 094305.

[5] S. Hou, P. Chen, M. Shah, I. Briggs, W. Xing, Z. Liu, L. Fan, *ACS Photonics* **2023**, *10*, 3896–3900.

[6] Y. Ding, S. Tao, X. Wang, C. Shang, A. Pan, C. Zeng, J. Xia, *Optics Express* **2022**, *30*, 22135.

[7] A. Prencipe, M. A. Baghban, K. Gallo, *ACS Photonics* **2021**, *8*, 2923–2930.

[8] J. He, D. Liu, B. Pan, Y. Huang, M. Zhu, M. Zhang, D. Dai, *Optics Express* **2022**, *30*, 34140.

[9] H.-P. Chung, C.-H. Lee, K.-H. Huang, S.-L. Yang, K. Wang, A. S. Solntsev, A. A. Sukhorukov, F. Setzpfandt, Y.-H. Chen, *Optics Express* **2019**, *27*, 1632.

[10] C. W. Wu, A. S. Solntsev, D. N. Neshev, A. A. Sukhorukov, *Optics Letters* **2014**, *39*, 953.

[11] A. Maeder, F. Kaufmann, D. Pohl, J. Kellner, R. Grange, *Optics Letters* **2022**, *47*, 4375.

[12] Y. Hu, D. Zhu, S. Lu, X. Zhu, Y. Song, D. Renaud, D. Assumpcao, R. Cheng, C. J. Xin, M. Yeh, H. Warner, X. Guo, A. Shams-Ansari, D. Barton, N. Sinclair, M. Loncar, *Nature Reviews Physics* **2025**, *7*, 237–254.

[13] C. Wang, M. Zhang, X. Chen, M. Bertrand, A. Shams-Ansari, S. Chandrasekhar, P. Winzer, M. Lončar, *Nature* **2018**, *562*, 101–104.

[14] D. Assumpcao, D. Renaud, A. Shams-Ansari, M. Loncar, *Optics Letters* **2025**, *50*, 1473.

[15] P.-K. Chen, I. Briggs, C. Cui, L. Zhang, M. Shah, L. Fan, *Nature Nanotechnology* **2024**, *19*, 44–50.

[16] A. Shams-Ansari, G. Huang, L. He, Z. Li, J. Holzgrafe, M. Jankowski, M. Churaev, P. Kharel, R. Cheng, D. Zhu, N. Sinclair, B. Desiatov, M. Zhang, T. J. Kippenberg, M. Lončar, *APL Photonics* **2022**, *7*, 081301.

[17] F. Kaufmann, G. Finco, A. Maeder, R. Grange, *Nanophotonics* **2023**, *12*, 1601–1611.

[18] C. J. Xin, S. Lu, J. Yang, A. Shams-Ansari, B. Desiatov, L. S. Magalhães, S. S. Ghosh, E. McGee, D. Renaud, N. Achuthan, A. Zvyagintsev, D. Barton III, N. Sinclair, M. Lončar, *Communications Physics* **2025**, *8*, 136.

[19] C. A. A. Franken, S. S. Ghosh, C. C. Rodrigues, J. Yang, C. J. Xin, S. Lu, D. Witt, G. Joe, G. S. Wiederhecker, K.-J. Boller, M. Lončar, **2025**, arXiv preprint arXiv:2503.16785 [physics.optics].

[20] A. Zanatta, *Results in Physics* **2022**, *39*, 105736.

[21] A. A. Kaminskii, A. V. Butashin, I. A. Maslyanizin, B. V. Mill, V. S. Mironov, S. P. Rozov, S. E. Sarkisov, V. D. Shigorin, *Physica Status Solidi (a)* **1991**, *125*, 671–696.

[22] N. Umemura, J. Hirohashi, Y. Nakahara, H. Oda, Y. Furukawa, *Optical Materials Express* **2019**, *9*, 2159.

[23] R. Tanaka, N. Hirayama, M. Yamanobe, I. Shoji in OSA Advanced Photonics Congress 2021, Novel Optical Materials and Applications, Optica Publishing Group, Washington, DC, **2021**, NoW2A.6.

[24] M. Marangoni, R. Ramponi in *Ferroelectric Crystals for Photonic Applications*, *Vol. 91*, (Eds.: P. Ferraro, S. Grilli, P. De Natale), Springer Berlin Heidelberg, Berlin, Heidelberg, **2009**, pp. 79–99.

[25] C. Wang, Z. Li, J. Riemensberger, G. Lihachev, M. Churaev, W. Kao, X. Ji, J. Zhang, T. Blesin, A. Davydova, Y. Chen, K. Huang, X. Wang, X. Ou, T. J. Kippenberg, *Nature* **2024**, *629*, 784–790.

[26] K. Kitamura, Y. Furukawa, S. Takekawa, T. Hatanaka, H. Ito, V. Gopalan, *Ferroelectrics* **2001**, *257*, 235–243.

[27] H. Chen, M. Zhao, H. Xie, Y. Su, Z. Ye, J. Ma, Y. Nie, Y. Niu, P. Zhan, S. Zhu, X. Hu, *Optical Materials Express* **2023**, *13*, 3543.

[28] H. Chen, X. Zhang, Z. Ye, X. Chen, C. Huang, P. Zhan, X. Ou, S. Zhu, X. Hu, *Optics Letters* **2025**, *50*, 1125.

[29] A. Shelton, C. J. Xin, K. Powell, J. Yang, S. Lu, N. Sinclair, M. Loncar, **2025**, arXiv preprint arXiv:2504.17980 [physics.optics].

[30] J. Zhang, C. Wang, C. Denney, J. Riemensberger, G. Lihachev, J. Hu, W. Kao, T. Blésin, N. Kuznetsov, Z. Li, M. Churaev, X. Ou, G. Santamaria-Botello, T. J. Kippenberg, *Nature* **2025**, *637*, 1096–1103.

Appendix A

PROPAGATION OF ELECTROMAGNETIC FIELDS

This appendix reviews Maxwell's equations in linear and nonlinear media. Relevant equations for electromagnetic propagation as well as dispersion are also covered.

A.1 Electromagnetic wave equations in linear media

Maxwell's equations in matter are [1]:

$$\nabla \times \mathbf{E} + \frac{\partial \mathbf{B}}{\partial t} = 0 \tag{A.1}$$

$$\nabla \times \mathbf{H} - \frac{\partial \mathbf{D}}{\partial t} = \mathbf{J} \tag{A.2}$$

$$\nabla \cdot \mathbf{D} = \rho \tag{A.3}$$

$$\nabla \cdot \mathbf{B} = 0 \tag{A.4}$$

where $\mathbf{E}$ is the electric field, $\mathbf{H}$ is the magnetic field, $\mathbf{D}$ is the electric displacement, $\mathbf{B}$ is the magnetic induction, ρ is the current density, and $\mathbf{J}$ is the current density.

To find a solution, Maxwell's equations also need to be supplemented with the constitutive relations:

$$\mathbf{D} = \varepsilon \mathbf{E} = \varepsilon_0 \mathbf{E} + \mathbf{P} \tag{A.5}$$

$$\mathbf{B} = \mu \mathbf{H} = \mu_0 \mathbf{H} + \mu_0 \mathbf{M} \tag{A.6}$$

where ε is the permittivity tensor, μ is the permeability tensor, $\mathbf{P}$ is the electric polarization, $\mathbf{M}$ is the magnetic polarization, ε_0 is the vacuum permittivity, and μ_0 is vacuum permeability.

In linear media, the polarization is proportional to the electric field:

$$\mathbf{P} = \varepsilon_0 \chi^{(1)} \mathbf{E} \tag{A.7}$$

where we have also defined the linear susceptibility $\chi^{(1)}$:

$$\varepsilon = \varepsilon_0 (1 + \chi^{(1)}). \tag{A.8}$$

To obtain the electromagnetic wave equations in linear media, the constitutive relations can first be plugged into Equations A.1 and A.2 of Maxwell's equations:

$$\begin{aligned} \nabla \times \mathbf{E} + \frac{\partial}{\partial t}(\mu \mathbf{H}) &= 0 \\ \nabla \times \mathbf{E} + \mu \frac{\partial \mathbf{H}}{\partial t} &= 0 \end{aligned} \tag{A.9}$$

$$\begin{aligned} \nabla \times \mathbf{H} - \frac{\partial}{\partial t}(\varepsilon \mathbf{E}) &= \mathbf{J} \\ \nabla \times \mathbf{H} - \varepsilon \frac{\partial \mathbf{E}}{\partial t} &= \mathbf{J}. \end{aligned} \tag{A.10}$$

Assuming the material has no free currents ($\mathbf{J} = 0$), these equations can be simplified to:

$$\nabla \times \mathbf{E} + \mu \frac{\partial \mathbf{H}}{\partial t} = 0 \tag{A.11}$$

$$\nabla \times \mathbf{H} - \varepsilon \frac{\partial \mathbf{E}}{\partial t} = 0. \tag{A.12}$$

Taking the curl of Equation A.11 produces:

$$\begin{aligned} \nabla \times (\nabla \times \mathbf{E}) + \nabla \times (\mu \frac{\partial \mathbf{H}}{\partial t}) &= 0 \\ \nabla \times (\nabla \times \mathbf{E}) + \mu \frac{\partial}{\partial t}(\nabla \times \mathbf{H}) &= 0 \end{aligned} \tag{A.13}$$

and plugging in the expression for $\nabla \times \mathbf{H}$ from Equation A.12:

$$\begin{aligned} \nabla \times (\nabla \times \mathbf{E}) + \mu \frac{\partial}{\partial t}(\varepsilon \frac{\partial \mathbf{E}}{\partial t}) &= 0 \\ \nabla \times (\nabla \times \mathbf{E}) + \mu \varepsilon \frac{\partial^2 \mathbf{E}}{\partial t^2} &= 0. \end{aligned} \tag{A.14}$$

The first term can be expanded using the following vector calculus identity:

$$\nabla \times (\nabla \times \mathbf{E}) = \nabla(\nabla \cdot \mathbf{E}) - \nabla^2 \mathbf{E}. \tag{A.15}$$

Starting from Equation A.3 and assuming a linear medium ($\mathbf{D} \propto \mathbf{E}$) with no free charges ($\rho = 0$), it follows that:

$$\begin{aligned} \nabla \cdot \mathbf{D} &= \rho \\ \nabla \cdot (\varepsilon \mathbf{E}) &= \rho \\ \varepsilon(\nabla \cdot \mathbf{E}) &= \rho = 0 \\ \nabla \cdot \mathbf{E} &= 0. \end{aligned} \tag{A.16}$$

Therefore, the first term on the right hand side of Equation A.15 is zero. Following a similar treatment for **H** using Equation A.12, we arrive at the wave equations for electromagnetic fields in linear media:

$$\nabla^2\mathbf{E} - \mu\varepsilon\frac{\partial^2\mathbf{E}}{\partial t^2} = 0 \tag{A.17}$$

$$\nabla^2\mathbf{H} - \mu\varepsilon\frac{\partial^2\mathbf{H}}{\partial t^2} = 0. \tag{A.18}$$

Solutions to the wave equations and commonly used definitions

The wave equations are satisfied by monochromatic plane waves of the form:

$$\Psi = Ae^{i(\mathbf{k}\cdot\mathbf{r}-\omega t)} \tag{A.19}$$

where ω is the angular frequency of the wave and $\mathbf{k}$ is the wavevector with magnitude:

$$|\mathbf{k}| = k = \omega\sqrt{\mu\varepsilon} = \frac{n\omega}{c} = \frac{2\pi n}{\lambda} \tag{A.20}$$

where n is the refractive index defined as $n = \sqrt{\frac{\mu\varepsilon}{\mu_0\varepsilon_0}}$, c is the speed of light defined as $c = \frac{1}{\sqrt{\mu_0\varepsilon_0}}$, and λ is the wavelength. In waveguides, this expression for the wavevector is modified to account for the confined modes:

$$\beta = n_{\text{eff}}\frac{\omega}{c} = n_{\text{eff}}\frac{2\pi}{\lambda} \tag{A.21}$$

where β is the propagation constant, analogous to k, and n_{eff} is the effective refractive index of the modes. For the waveguides used in this work, n_{eff} is calculated using a mode solver software (Ansys Lumerical).

We can also define the phase velocity v of the propagating plane wave:

$$v = \frac{\omega}{k} = \frac{1}{\sqrt{\mu\varepsilon}} = \frac{c}{n}. \tag{A.22}$$

For optical pulses, the group velocity is the speed at which the pulse envelope propagates through a medium. The group velocity v_g is defined as:

$$v_g = \frac{\partial\omega}{\partial k} = \frac{c}{n_g} \tag{A.23}$$

where n_g is the group index.

Dispersion

Dispersion is the phenomenon where the refractive index, and therefore the phase velocity and group velocity, varies with frequency. In bulk optics, dispersion is often associated with the behavior of the refractive index of a particular material, but dispersion can also be associated with the geometrical confinement of modes in waveguides, known as the waveguide dispersion. In waveguides, the total dispersion is typically a combination of the material dispersion and the waveguide dispersion.

The group velocity dispersion and group velocity mismatch are measures of dispersion that can affect the phase matching characteristics of nonlinear processes [2]. The group velocity dispersion (GVD) describes the temporal broadening of a pulse as it propagates through a medium and is defined as:

$$\text{GVD} = \frac{\partial}{\partial\omega}\left(\frac{1}{v_g}\right) = \frac{\partial^2 k}{\partial\omega^2}. \tag{A.24}$$

In nonlinear processes, a near-zero GVD can produce spectral broadening.

A similar quantity is the group velocity mismatch (GVM), which describes temporal walk-off or the difference in propagation of pulses at different frequencies. GVM is defined as:

$$\begin{aligned}\text{GVM} &= \frac{1}{v_{g,1}} - \frac{1}{v_{g,2}} \\ &= \left.\frac{\partial k}{\partial\omega}\right|_{\omega_1} - \left.\frac{\partial k}{\partial\omega}\right|_{\omega_2} \\ &= \frac{1}{c}\left(n_g|_{\omega_1} - n_g|_{\omega_2}\right).\end{aligned} \tag{A.25}$$

In nonlinear processes, a near-zero GVM will increase the phase-matching bandwidth.

A.2 Electromagnetic wave equations in nonlinear media

In Section A.1, the polarization was assumed to be linear to the electric field (Equations A.7, A.16). However, nonlinear crystals have a more general form for the polarization [3], as described in Equation 2.3, and therefore the wave equations must be revisited for nonlinear media.

Revisiting (Equation A.14) with the polarization $\mathbf{P}$ explicitly included:

$$\begin{aligned}\nabla\times(\nabla\times\mathbf{E}) + \mu\frac{\partial}{\partial t}(\frac{\partial}{\partial t}(\mathbf{D})) &= 0 \\ \nabla\times(\nabla\times\mathbf{E}) + \mu\frac{\partial^2}{\partial t^2}(\varepsilon_0\mathbf{E}+\mathbf{P}) &= 0.\end{aligned} \tag{A.26}$$

Splitting the polarization into its linear and nonlinear components following Equation 2.3:

$$\nabla \times (\nabla \times \mathbf{E}) + \mu \frac{\partial^2}{\partial t^2}(\varepsilon_0 \mathbf{E} + \mathbf{P}_L + \mathbf{P}_{NL}) = 0. \tag{A.27}$$

Expanding the expression for the linear polarization $\mathbf{P}_L$ using Equation 2.4, we can combine terms using the expression for the linear susceptibility and permittivity in Equation A.8:

$$\begin{aligned} \nabla \times (\nabla \times \mathbf{E}) + \mu \frac{\partial^2}{\partial t^2}(\varepsilon_0 \mathbf{E} + \varepsilon_0 \chi^{(1)} \mathbf{E} + \mathbf{P}_{NL}) = 0 \\ \nabla \times (\nabla \times \mathbf{E}) + \mu \frac{\partial^2}{\partial t^2}(\varepsilon_0 (1 + \chi^{(1)}) \mathbf{E} + \mathbf{P}_{NL}) = 0 \\ \nabla \times (\nabla \times \mathbf{E}) + \mu \varepsilon \frac{\partial^2}{\partial t^2} \mathbf{E} + \mu \frac{\partial^2}{\partial t^2} \mathbf{P}_{NL} = 0. \end{aligned} \tag{A.28}$$

We can see that this is a very similar expression to Equation A.14. Following Section A.1, we can use the vector calculus identity given in Equation A.15. However, we were able to use Maxwell's equations and the proportionality between the displacement and the electric field to show that $\nabla \cdot \mathbf{E} = 0$ in linear media (Equation A.16). This is not necessarily true for nonlinear media due to the more general form of $\mathbf{P}_{NL}$. However, in many cases the $\nabla \cdot \mathbf{E}$ term can either be dropped, such as for transverse plane waves, or be shown to have a negligible contribution, especially if the slowly varying amplitude approximation is valid [3].

We finally arrive at the wave equation for nonlinear crystals:

$$\nabla^2 \mathbf{E} - \mu \varepsilon \frac{\partial^2 \mathbf{E}}{\partial t^2} - \mu \frac{\partial^2 \mathbf{P}_{NL}}{\partial t^2} = 0 \tag{A.29}$$

which takes the form of a driven differential equation.

References

[1] A. Yariv, P. Yeh, *Photonics: Optical Electronics in Modern Communications*, 6. edition, Oxford University Press, New York, NY, **2007**, 836 pp.

[2] L. Ledezma, R. Sekine, Q. Guo, R. Nehra, S. Jahani, A. Marandi, *Optica* **2022**, *9*, 303.

[3] R. W. Boyd, *Nonlinear Optics*, 3rd ed, Academic Press, Amsterdam ; Boston, **2008**, 613 pp.

Appendix B

DEVICE FABRICATION

This appendix describes the fabrication of the devices described throughout this thesis. Device fabrication was performed in the Kavli Nanoscience Institute at Caltech. Periodic poling and second harmonic microscopy was performed at the Beckman Biological Imaging Facility.

B.1 Fabrication overview

Periodically poled lithium niobate waveguides can be fabricated in four general steps (Figure B.1). First, the poling periods and target waveguide cross section are calculated in a mode solver software. Next, electrodes are fabricated based on the design poling period. The electrodes are then ferroelectrically poled, resulting in the periodic inverted domains in lithium niobate that impart quasi-phase matching (QPM). Finally, waveguides are etched into the periodically poled region.

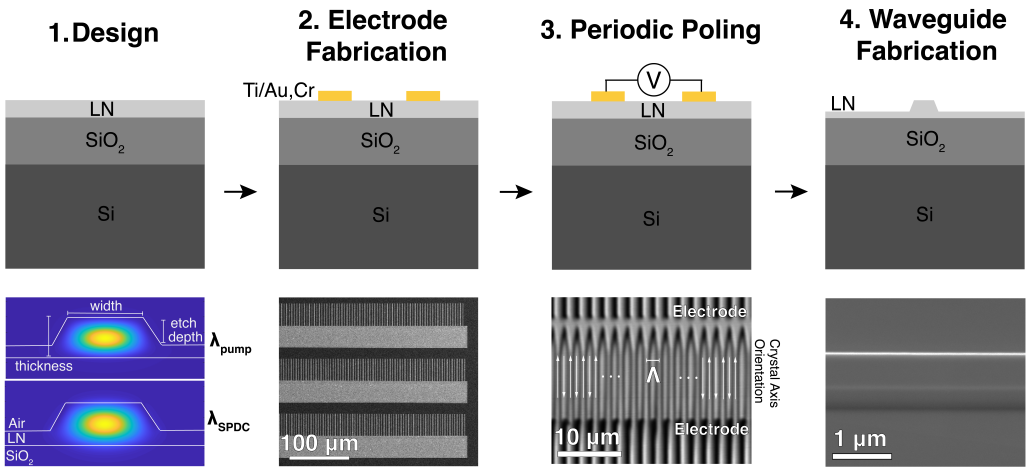

Figure B.1: General process flow for periodically poled TFLN waveguide fabrication.

For the alternate fabrication processes described in Section 6.4 and Chapter 7, many of the general steps shown in Figure B.1 remain the same. For adapted poling [1], the lithium niobate film thickness of the chip is first mapped. During the design of the waveguides, the poling period and electrodes are designed for the range of thicknesses measured throughout the chip, as opposed to assuming a constant

thicknesses. The remainder of the fabrication follows Figure B.1. For the etch-before-pole process [2, 3], the steps shown in Figure B.1 remain the same, but the order is changed such that after the design, the waveguides are fabricated first, then the electrodes are fabricated, and periodic poling is performed last. Both adapted poling and the etch-before-pole process can also be incorporated together. In this process, the process order would be: the lithium niobate thickness is mapped, the waveguide cross-section and poling periods are designed for the measured thicknesses, the waveguides are fabricated, the electrodes are fabricated, and finally the chip is poled.

B.2 Design

Devices are designed with a finite-difference eigenmode (FDE) solver (Ansys Lumerical MODE). For periodically poled waveguides, the mode profiles and effective refractive indices are calculated at each wavelength of interest, typically the fundamental pump and second harmonic wavelengths for SHG (Chapter 3), the excitation and fluorescence wavelengths for the dye samples (Chapter 5), or the pump and relevant degenerate or non-degenerate SPDC wavelengths for SPDC (Chapters 4 and 6). Additional dispersion calculations to calculate the group velocity dispersion (GVD) and group velocity mismatch (GVM) are performed for the CSPDC devices in Chapter 6.

B.3 Electrode fabrication

Electrodes for periodic poling are fabricated through a lift-off process (Figure B.2). Bilayer PMMA is exposed through electron beam lithography (Raith EBPG 5200) and developed to produce the periodic electrode fingers to impart quasi-phase matching. Metal (titanium and gold or chromium) is deposited through an electron beam evaporator (Kurt J. Lesker Labline evaporator, AJA Orion evaporator). The PMMA

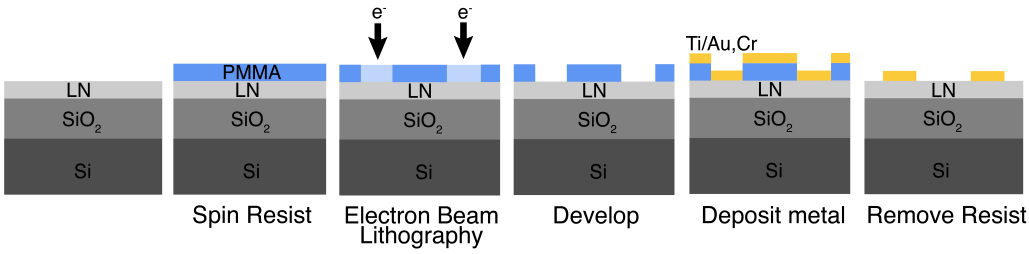

Figure B.2: Process flow (left to right) for the liftoff process used to fabricate periodic poling electrodes.

is removed in acetone, producing the patterned metal electrodes.

B.4 Periodic poling

To pole the lithium niobate thin films, high voltage square wave pulses (typically around 800 V and 40 µs) are applied to each pair of electrodes using a waveform generator and high voltage amplifier. The domain inversion and poling domain quality was monitored through confocal second harmonic microscopy (Zeiss LSM 880).

B.5 Waveguide fabrication

Waveguides are defined in hydrogen silsesquioxane (HSQ) resist exposed through an aligned write with electron beam lithography (Raith EBPG 5200). To improve the adhesion of HSQ to lithium niobate, adhesion layers of either spin-coated PMMA or evaporated titanium (Kurt J. Lesker Labline evaporator) are used. The waveguide pattern is transferred to the lithium niobate film with an argon plasma (Oxford III-V ICP-RIE). The physical nature of the argon plasma imparts angled sidewalls, resulting in a trapezoidal waveguide cross-section. The adhesion layer and any residual HSQ is removed, and redeposition is removed with a SC-1 clean. The etched waveguide dimensions are measured through atomic force microscopy (Bruker Dimension Icon) and the device facets are mechanically polished to increase optical transmission.

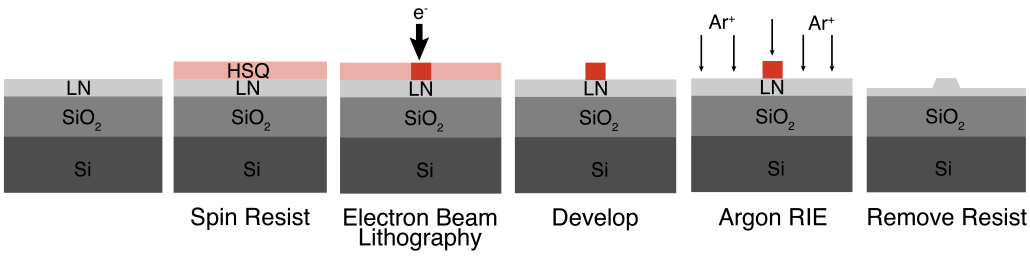

Figure B.3: Process flow (left to right) for waveguide lithography and etching.

References

[1] P.-K. Chen, I. Briggs, C. Cui, L. Zhang, M. Shah, L. Fan, *Nature Nanotechnology* **2024**, *19*, 44–50.

[2] C. J. Xin, S. Lu, J. Yang, A. Shams-Ansari, B. Desiatov, L. S. Magalhães, S. S. Ghosh, E. McGee, D. Renaud, N. Achuthan, A. Zvyagintsev, D. Barton III, N. Sinclair, M. Lončar, *Communications Physics* **2025**, *8*, 136.

[3] C. A. A. Franken, S. S. Ghosh, C. C. Rodrigues, J. Yang, C. J. Xin, S. Lu, D. Witt, G. Joe, G. S. Wiederhecker, K.-J. Boller, M. Lončar, **2025**, arXiv preprint arXiv:2503.16785 [physics.optics].

Appendix C

SUPPLEMENTARY INFORMATION FOR VISIBLE THROUGH NEAR-INFRARED SPONTANEOUS PARAMETRIC DOWNCONVERSION

C.1 SPDC theoretical efficiency with a multimode pump

The theory of parametric down-conversion in waveguides is well established, and has been reviewed in Section 2.3. Here, the equations used in the simulations for Chapter 4 for a multi-frequency pump are described. We can start from Equation 2.51 for the downconverted signal power P_s in the frequency interval $d\omega_s$ for a single-frequency pump with power P_p in a quasi-phase matched crystal [1]:

$$d\mathrm{P}_s = \frac{\hbar d_{\mathrm{QPM}}^2 \mathrm{P}_p \omega_s^2 \omega_i L^2}{\pi \varepsilon_0 c^3 n_p n_s n_i A_{\mathrm{eff}}} \mathrm{sinc}^2\left(\frac{\Delta\beta_{\mathrm{QPM}} L}{2}\right) d\omega_s \tag{C.1}$$

where $\hbar$ is the reduced Planck's constant, L is the periodically poled length, ω_i is the idler frequency based on energy conservation with the pump and signal frequencies, ε_0 is the vacuum permittivity, c is the speed of light, and $n_{p,s,i}$ are the respective effective refractive of the modes. As discussed in Section 2.4, the quasi-phase matched momentum mismatch $\Delta\beta_{\mathrm{QPM}}$ is (Equation 2.55):

$$\Delta\beta_{\mathrm{QPM}} = \beta_p - \beta_s - \beta_i - \frac{2\pi m}{\Lambda} \tag{C.2}$$

where $\beta_{p,s,i}$ are the respective propagation constants of the waveguide modes, m is the order of the phase matching, and Λ is the poling period. Similarly, d_{QPM} is given by (Equation 2.56):

$$d_{\mathrm{QPM}} = d_{\mathrm{eff}} \frac{2\sin(m\pi D)}{m\pi} \tag{C.3}$$

where D is the poling duty cycle and d_{eff} is the effective nonlinear coefficient. For the crystal orientation and waveguide polarizations used in Chapter 4, $d_{\mathrm{eff}} = d_{33} = 28.4$ pm/V for 5% MgO-doped lithium niobate at 852 nm [2]. With a duty cycle close to 50% (Figure 4.1b), $d_{\mathrm{eff}} = 18.1$ pm/V.

In the waveguide, the effective area A_{eff} is given as a mode overlap calculation of the three interacting waves mediated through the nonlinear tensor of the crystal[3]. For the device used in this work, the effective area can be simplified as:

$$A_{\text{eff}} = \frac{A_p A_s A_i}{\sqrt{\frac{n_p n_s n_i A_p A_s A_i}{8 Z_0^3 \text{P}^3}} \left| \iint \overline{d}_{33} E_s^* E_i^* E_p \, dx \, dy \right|^2}. \tag{C.4}$$

Here $A_{p,s,i}$ are the effective areas of each mode, Z_0 is the free space impedance, P is the power in each mode (normalized to 1 W here), $\overline{d}_{33}$ is the normalized d_{33} nonlinear tensor element, and $E_{p,s,i}$ are the electric field profiles of each mode. The mode profiles are evaluated in Lumerical MODE to find that $A_{\text{eff}} = 0.7\ \mu\text{m}^2$ for the device presented in Chapter 4.

To modify C.1 to accommodate a multi-frequency pump, the pump power P_p can be replaced with the spectral intensity of the pump $\text{P}(\omega_p)$ and integrated over all pump frequencies:

$$d\text{P}_s = \int_{\omega_p} \frac{\hbar d_{\text{QPM}}^2 \omega_s^2 \omega_i L^2}{\pi \varepsilon_0 c^3 n_p n_s n_i A_{\text{eff}}} \text{sinc}^2 \left(\frac{\Delta\beta_{\text{QPM}} L}{2} \right) d\omega_s \text{P}(\omega_p) d\omega_p \tag{C.5}$$

which can also be numerically integrated over all signal frequencies (Equation 2.52) to obtain theoretical SPDC spectra:

$$\text{P}_s = \iint \frac{\hbar d_{\text{eff}}^2 \omega_s^2 \omega_i L^2}{\pi \varepsilon_0 c^3 n_p n_s n_i A_{\text{eff}}} \text{sinc}^2 \left(\frac{\Delta\beta_{\text{QPM}} L}{2} \right) \text{P}(\omega_p) d\omega_s d\omega_p. \tag{C.6}$$

For the simulations given in Chapter 4, the pump spectral intensity is approximated as a Gaussian distribution with a mean μ and standard deviation σ such that the FWHM is 0.8 nm, as measured experimentally, and is normalized to an total intensity of 1 mW:

$$P(\omega_p) = \frac{1}{\sigma\sqrt{2\pi}} \exp\left[-\frac{1}{2} \left(\frac{\omega_p - \mu}{\sigma} \right)^2 \right]. \tag{C.7}$$

Because the signal and idler are indistinguishable, and thus both detected in our experiment, the expected total number of counts at a given frequency for the spectrally resolved experiments (Figure 4.3) is:

$$\frac{\text{d}W}{\text{d}\omega} = \left. \frac{\text{d}W}{\text{d}\omega} \right|_{\omega=\omega_s} + \left. \frac{\text{d}W}{\text{d}\omega} \right|_{\omega=\omega_p-\omega_s} \tag{C.8}$$

Finally, it is useful to have an equation for the probability of jointly detecting a signal photon at ω_s and an idler at ω_i. This distribution is typically called the Joint Spectral Intensity (JSI) and is obtained from C.5 by replacing the pump frequency by sum of the signal and idler frequencies:

$$\mathrm{JSI}(\omega_s, \omega_i) = C \frac{\omega_s \omega_i}{n_p n_s n_i} \mathrm{sinc}^2 \left(\frac{\Delta k L}{2} \right) P(\omega_s + \omega_i). \tag{C.9}$$

Here, C is a normalization constant chosen such that

$$\iint \mathrm{JSI}(\omega_s, \omega_i) \mathrm{d}\omega_s \mathrm{d}\omega_i \equiv 1. \tag{C.10}$$

Thus, the JSI represents a two-dimensional probability distribution, and is symmetric with respect to exchange of the variables ω_s and ω_i.

C.2 Broadband oscillator characterization

A broadband oscillator (Coherent Vitara) is used to test the phase matching and simulate the SPDC transmission of the device. In this characterization scheme, the oscillator output is sent into a single mode polarization-maintaining tapered fiber (OZ Optics Ltd.) to couple into the waveguide. A second identical tapered fiber collects the output of the waveguide and is sent into a grating spectrometer and electron-multiplying intensified camera, similarly to Figure 4.2b. The spectrum of the oscillator (Figure C.1a), although broad with an 85 nm FWHM bandwidth, aids

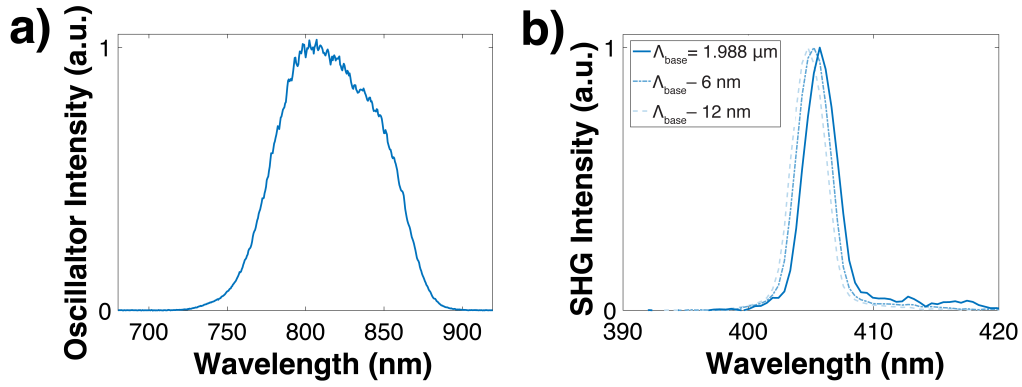

Figure C.1: Oscillator and second harmonic generation spectra. (a) Spectrum of the broadband oscillator. (b) Second harmonic generation spectra corresponding to waveguides with three different poling periods. The waveguide corresponding to the spectrum denoted with $\Lambda_{\mathrm{base}} = 1.988$ μm was chosen for the measurements in Chapter 4.

in finding phase-matching over a wide wavelength range and also mimics the spread of the SPDC spectrum (Figure 4.3c) for transmission measurements.

The phase matching of the device was tested through second harmonic generation (SHG), which should have similar phase matching to SPDC. Several sets of electrodes with varied poling periods near the computationally predicted value (2.03 μm, Section 4.2) were fabricated to compensate for possible fabrication imperfections that could disrupt phase matching. Three waveguides with different poling periods were tested to verify that the SHG was phase matched (Figure C.1b). The waveguide chosen for further measurements from the SHG measurements has a poling period of 1.988 μm. This poling period had a computationally predicted degenerate wavelength of 403 nm, which is under 3 nm from the experimentally measured degenerate wavelength of 405.7 nm. This <3 nm discrepancy is likely due to variations in the thin film thickness or etch depth.

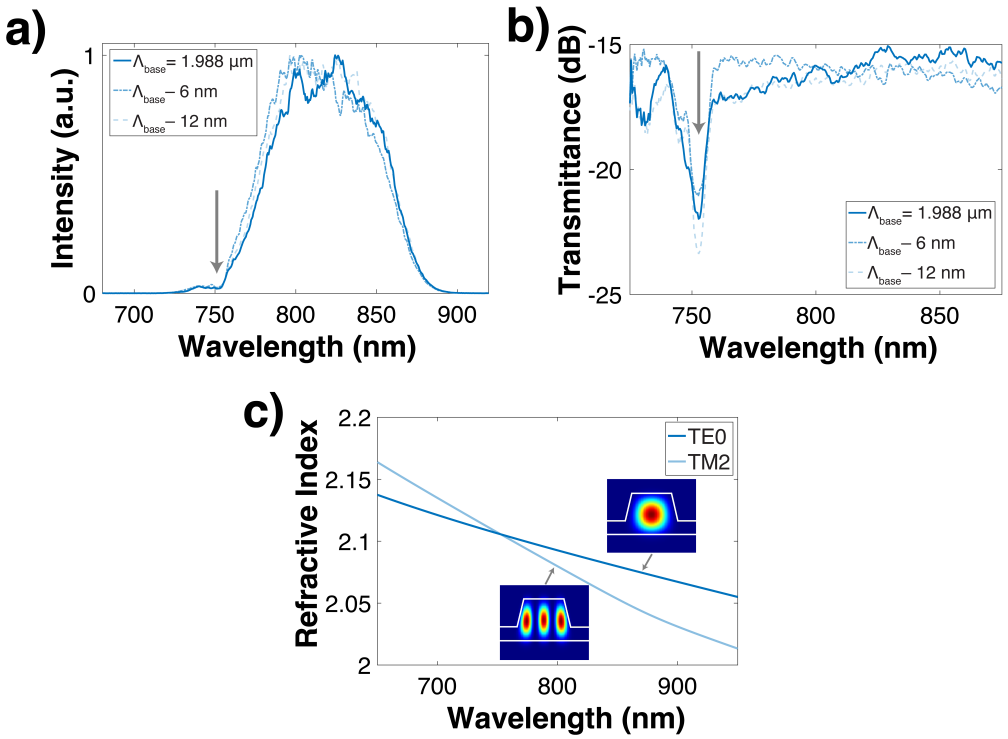

Figure C.2: Waveguide transmission spectra measured through three different waveguides in units of (a) normalized intensity and (b) transmittance in dB with respect to the oscillator spectrum from Figure C.1a. Loss at approximately 755 nm can be observed in both (a) and (b), indicated by the arrows. (c) Simulated mode refractive indices, demonstrating a mode-crossing near 755 nm between the TE0 and TM2 modes.

The transmission spectra of these same three devices show an approximately 5 dB dip in transmittance near 755 nm (Figure C.2a-b), which corresponds with the dip in the SPDC spectra seen in Figure 4.3a. These spectra suggest that the source of loss occurs downstream of the SPDC pair production and the loss occurs on-chip as opposed to in free space. If the dip was caused by a discontinuity in the phase-matching, a similar dip would be seen in the conjugate spectrum of the idler photon near 874 nm. Since different optical paths are used for the transmission spectra in Figure C.2 and the SPDC spectra in Figure 4.3, the loss occurs on-chip. It is also clear that this loss is systematic, as it is observed in all three waveguides tested. While slab mode leakage can be an issue for the TE waveguide modes in TFLN, this mechanism is unlikely because the transmission recovers at lower wavelengths, whereas slab mode leakage is expected to occur for all wavelengths below a certain cutoff, which is not true here as the transmission and SPDC both recover below 755 nm. One potential source of loss could be a mode-crossing [4] at 755 nm that transfers power from the fundamental TE mode to a higher-order mode, demonstrated by the calculated modal refractive indices in Figure C.2c. Such higher-order modes would be collected inefficiently by the aspheric lenses, which already suffer from chromatic aberrations, and the single-mode tapered fibers, which act as mode filters. Future mode-crossings could be avoided by careful selection of the waveguide top width, thickness, and etch depth.

C.3 Single and joint detection probability

The SPADs used in this study (Laser Components COUNT-10C) exhibit a spectrally-dependent quantum efficiency with a peak at 680 nm (Figure C.3). This wavelength dependence complicates the prediction of detection probabilities due to the large SPDC bandwidth.

The quantum efficiency curve from the manufacturer specifications can be interpolated to obtain a continuous quantum efficiency $\mathrm{QE}(\omega)$, which ranges from 0 to 1. From this distribution, the probability of detecting both the signal and idler (i.e. a coincidence) is an expectation value given as:

$$\eta_{12} = \iint \mathrm{JSI}(\omega_s, \omega_i)\mathrm{QE}(\omega_s)\mathrm{QE}(\omega_i)\mathrm{d}\omega_s\mathrm{d}\omega_i. \tag{C.11}$$

The probability of detection given the presence of a single photon is also given as an expectation value. The quantum efficiency is weighted by the probability distribution of the signal photon frequency, which is obtained by integrating over

all possible idler frequencies:

$$\eta_1 = \iint \mathrm{JSI}(\omega_s, \omega_i)\mathrm{QE}(\omega_s)\mathrm{d}\omega_s\mathrm{d}\omega_i. \tag{C.12}$$

Given that two near-identical SPAD detectors are used, the quantum efficiency of both detectors are assumed to be equal ($\eta_1 = \eta_2$). As a result, only η_1 appears in the following equations, as well as Equation 4.1. These probabilities are calculated as $\eta_1 = 0.522$ and $\eta_{12} = 0.266$. In this case, $\eta_{12} \approx \eta_1^2$, which would not be generally expected given the wide range of wavelengths and large variations in the quantum efficiency. However, due to the linearity of $\mathrm{QE}(\omega)$ in the vicinity of our experiment, an increase in the quantum efficiency of the signal photon at shorter wavelengths is balanced by the decreased probability of detecting the idler photon at longer wavelengths.

C.4 Power sweep experimental details and raw data

The raw data obtained from the power swept coincidence counting experiment are displayed in Table C.1. On-chip inferred powers are determined by multiplying the free-space laser power by the 10.2 dB transmission of the input coupler. For each power, the singles rate and a coincidence histogram are recorded. The mean singles rates of the two detectors are calculated from 10 consecutive measurements

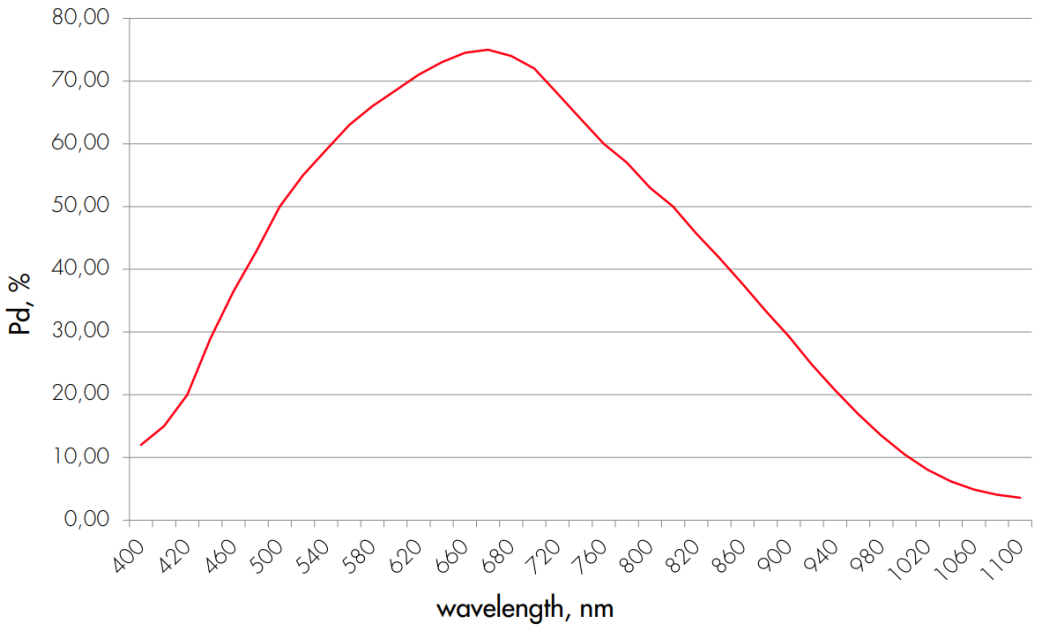

Figure C.3: Spectrally-dependent quantum efficiency $\mathrm{QE}(\omega)$ of the SPADs used in this work, from [5].

with a 1 s integration time. Each coincidence histogram is recorded with a 100 s integration time. Raw coincidence rates are calculated by integrating the number of coincidence counts in a 9.5 ns interval at the coincidence peak. This coincidence interval is centered at a time delay of 29.43 ns, which accounts for the electronic delay applied within the timing circuit and any mismatches in the electrical cabling from the detectors. Accidental counts are integrated from a time delay of 50 ns until the end of the histogram recording, 262.14 ns. This large range is chosen to minimize the uncertainty in the determination of the accidental rate at low pump powers. To be consistent with the coincidence rates, the accidental rates are scaled to give the count rate over a 9.5 ns window, which are reported in Table C.1. True coincidences are calculated by subtracting the inferred accidental rate from the raw coincidence rate. The coincidence to accidental ratio (CAR), defined as the ratio of true coincidences to accidentals, is also tabulated. The uncertainty in the singles rate is given as the standard deviation of the 10 singles measurements. The uncertainties in the raw coincidence and accidental rates are reported as standard deviations calculated assuming Poisson statistics. Here, the standard deviation in the total counts N is calculated as $\sqrt{N}$. The uncertainties in the count rates are then scaled by the integration times. Uncertainties in the true count rates and the CAR are determined using standard error propagation.

C.5 Power scaling equations

The scaling of the single and coincidence detection rates are useful for estimating the device efficiency and transmission efficiency of pairs through the system. A simple model is used to estimate these quantities, similar to Ref. [6]. First, the rate of singles counts at detectors 1 and 2 (S_1, S_2) are modeled as:

$$S_1(P) = 2EP\mu_1 R\eta_1 + \text{Dark}_1 \tag{C.13}$$

$$S_2(P) = 2EP\mu_2 T\eta_1 + \text{Dark}_2 \tag{C.14}$$

where E is the pair production efficiency, P is the on-chip power, $\mu_{1,2}$ are the transmission of the path to detectors 1 and 2, R and T are the beamsplitter reflection and transmission probabilities, η_1 is the average detector quantum efficiency given by Equation C.12, and $\text{Dark}_{1,2}$ are the dark counts of detectors 1 and 2. This can be interpreted as $2EP$ photons being produced by the device (the factor of 2 is from the two photons produced in each SPDC pair), then suffering losses of $\mu_1 R\eta_1$ or $\mu_2 T\eta_1$ in the setup before being detected by the respective SPADs.

Table C.1: Power Sweep Raw Data. Coincidence data used to calculate the pair generation efficiency of the device. Note that the true coincidence rate and the two singles rates are plotted against on-chip power in Figure 4.4b-c.

On-chip Power (nW)	Singles Rate Detector 1 (cps)	Singles Rate Detector 2 (cps)	Raw Coincidence Rate (cps)	Accidental Rate (cps)	True Coincidence Rate (cps)	CAR
0.096	$(8.1 \pm 0.5) \times 10^2$	$(7.4 \pm 0.4) \times 10^2$	$(3.10 \pm 0.06) \times 10^1$	$(3.8 \pm 0.4) \times 10^{-2}$	$(3.09 \pm 0.06) \times 10^1$	$(8.2 \pm 0.9) \times 10^2$
0.18	$(2.3 \pm 0.3) \times 10^3$	$(2.2 \pm 0.3) \times 10^3$	$(8.81 \pm 0.09) \times 10^1$	$(1.32 \pm 0.08) \times 10^{-1}$	$(8.80 \pm 0.09) \times 10^1$	$(6.7 \pm 0.4) \times 10^2$
0.34	$(5.20 \pm 0.06) \times 10^3$	$(4.84 \pm 0.6) \times 10^3$	$(2.17 \pm 0.01) \times 10^2$	$(2.3 \pm 0.1) \times 10^{-1}$	$(2.17 \pm 0.01) \times 10^2$	$(9.5 \pm 0.4) \times 10^2$
0.64	$(1.049 \pm 0.005) \times 10^4$	$(9.72 \pm 0.07) \times 10^3$	$(4.40 \pm 0.02) \times 10^2$	$(9.4 \pm 0.2) \times 10^{-1}$	$(4.39 \pm 0.02) \times 10^2$	$(4.7 \pm 0.1) \times 10^2$
1.2	$(1.83 \pm 0.02) \times 10^4$	$(1.68 \pm 0.01) \times 10^4$	$(7.55 \pm 0.03) \times 10^2$	$(2.86 \pm 0.04) \times 10^0$	$(7.52 \pm 0.03) \times 10^2$	$(2.63 \pm 0.03) \times 10^2$
2.3	$(3.71 \pm 0.03) \times 10^4$	$(3.42 \pm 0.01) \times 10^4$	$(1.498 \pm 0.004) \times 10^3$	$(1.15 \pm 0.07) \times 10^1$	$(1.486 \pm 0.004) \times 10^3$	$(1.288 \pm 0.009) \times 10^2$
4.3	$(6.73 \pm 0.03) \times 10^4$	$(6.15 \pm 0.03) \times 10^4$	$(2.641 \pm 0.005) \times 10^3$	$(3.76 \pm 0.1) \times 10^1$	$(2.604 \pm 0.005) \times 10^3$	$(6.92 \pm 0.03) \times 10^1$
8.1	$(1.368 \pm 0.006) \times 10^5$	$(1.260 \pm 0.006) \times 10^5$	$(5.221 \pm 0.007) \times 10^3$	$(1.547 \pm 0.002) \times 10^2$	$(5.067 \pm 0.007) \times 10^3$	$(3.276 \pm 0.007) \times 10^1$
15	$(2.535 \pm 0.009) \times 10^5$	$(2.329 \pm 0.008) \times 10^5$	$(9.50 \pm 0.01) \times 10^3$	$(5.295 \pm 0.005) \times 10^2$	$(8.96 \pm 0.01) \times 10^3$	$(1.692 \pm 0.002) \times 10^1$
29	$(4.771 \pm 0.006) \times 10^5$	$(4.337 \pm 0.007) \times 10^5$	$(1.752 \pm 0.001) \times 10^4$	$(1.833 \pm 0.001) \times 10^3$	$(1.569 \pm 0.001) \times 10^4$	$(8.561 \pm 0.008) \times 10^0$

Similarly, the rate of coincidences ($S_{cc}(P)$), which requires the detection of both photons, is:

$$S_{cc}(P) = EP\mu_1\mu_2 2RT\eta_{12} \tag{C.15}$$

where the factor of $2RT$ accounts for the two possible paths through the beamsplitter that result in a coincidence.

The slopes of Equations C.13-C.15 with respect to power, as shown below in Equations C.16-C.18, can be experimentally measured.

$$m_1 = 2E\mu_1 R\eta_1 \tag{C.16}$$

$$m_2 = 2E\mu_2 T\eta_1 \tag{C.17}$$

$$m_{cc} = 2E\mu_1\mu_2 RT\eta_{12} \tag{C.18}$$

These equations are then rearranged to solve for the efficiency and loss of the setup, given that R, T, η_1, and η_{12} are known.

$$E = \frac{m_1 m_2}{m_{cc}} \frac{\eta_{12}}{2\eta_1^2} \tag{C.19}$$

$$\mu_1 = \frac{m_{cc}}{m_2} \frac{\eta_1}{R\eta_{12}} \tag{C.20}$$

$$\mu_2 = \frac{m_{cc}}{m_1} \frac{\eta_1}{T\eta_{12}} \tag{C.21}$$

The parameters measured in the experiment as well as the parameters necessary for calculating the device loss are displayed in Table C.2.

Table C.2: Power Scaling Parameters. Uncertainties of the photon count rates are obtained from standard error of a linear fit. Beamsplitter and detector uncertainties are obtained from the manufacturers. Derived parameter (E, μ_1, μ_2) uncertainties are obtained through standard uncertainty propagation.

Parameter	Value	Description
m_1	$(1.670 \pm 0.005) \times 10^{10}$ photons/s/mW	Detector 1 Singles Rate
m_2	$(1.521 \pm 0.007) \times 10^{10}$ photons/s/mW	Detector 2 Singles Rate
m_{cc}	$(5.5 \pm 0.1) \times 10^{8}$ pairs/s/mW	Coincidence Rate
R	$47 \pm 10\%$	Beamsplitter Reflectance
T	$47 \pm 10\%$	Beamsplitter Transmittance
η_1	$52 \pm 5\%$	Average Quantum Efficiency
η_{12}	$27 \pm 4\%$	Average Joint Quantum Efficiency
E	$(2.3 \pm 0.5) \times 10^{11}$ pairs/s/mW	Device Efficiency
μ_1	$15 \pm 4\%$	Transmission to Detector 1
μ_2	$14 \pm 4\%$	Transmission to Detector 2

C.6 Pump linewidth comparison

The measured SPDC efficiency of the device ($(2.3 \pm 0.5) \times 10^{11}$ pairs/s/mW) is on par with the efficiencies of telecom regime TFLN sources and an order of magnitude or greater than the efficiencies of other visible SPDC sources, as shown in Figure 6 of the main text. However, this efficiency is significantly lowered by the bandwidth of the pump laser used in this work, which was experimentally measured to be 0.8 nm FWHM.

As shown in Figure C.4a, the calculated SPDC efficiency for a single frequency pump demonstrates a strong peak at the degenerate wavelength. The SPDC from a multimode pump can be understood as a convolution of the pump lineshape with Figure C.4a. For the same total input power, the spread in the spectral density of a multimode pump results in only a fraction of the total power overlapping with this peak in the efficiency, while a single frequency pump can be tuned to the maximum efficiency. Therefore, as shown in Figure C.4b, the maximum brightness of the SPDC spectrum from a single frequency pump is an order of magnitude higher than the spectrum for a multimode pump for the same input power.

To further quantify the enhanced device performance with a single frequency pump, the theoretical efficiencies of SPDC from single frequency pump and a multimode pump can be calculated. Approximating the pump as a Gaussian distribution with a

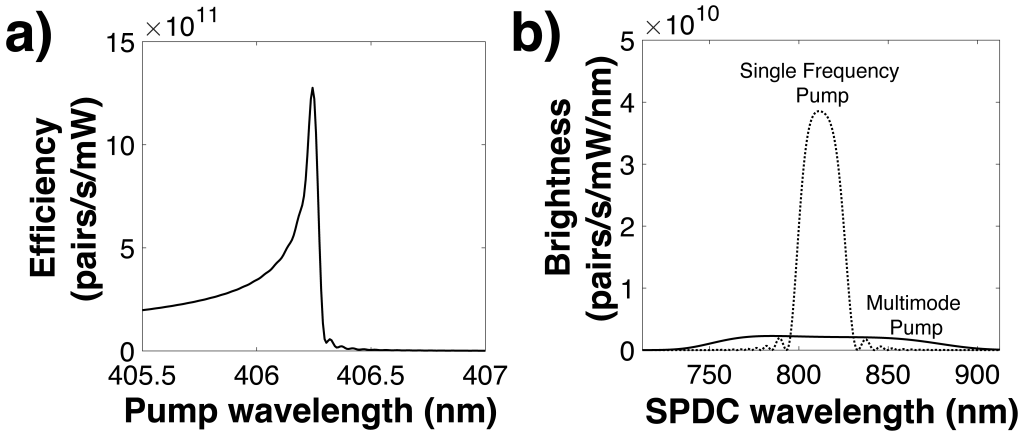

Figure C.4: Comparison of pump linewidths. (a) Theoretical single-frequency SPDC efficiency while varying the pump wavelength. The lack of symmetry in the efficiency can be explained by non-degenerate phase-matching at wavelengths shorter than the degenerate wavelength (here designed to be 406.25 nm), as shown by Figure 4.3. (b) Theoretical SPDC spectra for a single frequency pump and a broadband pump, both with 1 mW of power.

FWHM of 0.8 nm (Equation C.7), theoretical efficiency of 2.66×10^{11} pairs/s/mW is obtained using Equation C.6. However, using Equation 2.52, the theoretical efficiency using a single frequency pump is calculated to be 1.28×10^{12} pairs/s/mW. Therefore, approximately an order of magnitude of enhancement is expected by using a single frequency pump over a multimode pump.

C.7 Michelson interferogram

Two-photon interference in a Michelson interferometer has been demonstrated in several previous works. Ref. [7] is used to predict the shape of the experimentally measured interferogram shown in Figure 4.5a:

$$R_{cc}(\tau) = \iint d\omega_s d\omega_p \, \mathrm{JSI}(\omega_s, \omega_p - \omega_s)[1 + \cos(\omega_s \tau)][1 + \cos((\omega_p - \omega_s)\tau)]. \tag{C.22}$$

Here τ is the path-length difference of the interferometer, which is twice the physical difference in the path lengths due to the reflection at the translating mirror. The cosine terms in Equation C.22 can be expanded as:

$$\begin{aligned}[1 + \cos(\omega_s \tau)][1 + \cos((\omega_p - \omega_s)\tau)] = \\ 1 + \cos(\omega_s \tau) + \cos((\omega_p - \omega_s)\tau) + \frac{1}{2}\cos(\omega_p \tau) + \frac{1}{2}\cos((\omega_p - 2\omega_s)\tau).\end{aligned} \tag{C.23}$$

At large delays, the cosine terms dependent on ω_s average to zero, and the interference is dominated by $1 + \cos(\omega_p \tau)$, explaining the oscillation at the pump frequency with a theoretical 50% visibility. The predicted inteferogram from Equation C.22 can be seen in Figure 4.5b.

To assess the visibility at large delays, a subset of the interferogram (Figure 4.5d) was selected. A sinusoid of the following form was fit to the data with a nonlinear least squares algorithm:

$$A + B\cos(\omega\tau) + C\sin(\omega\tau). \tag{C.24}$$

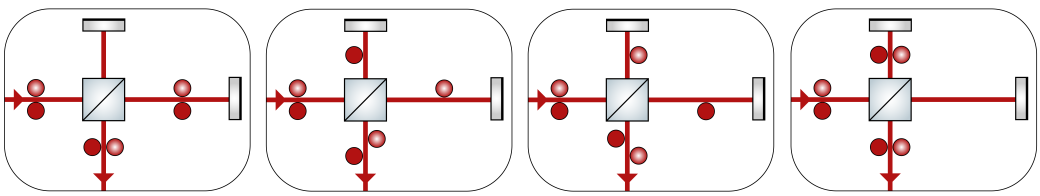

Figure C.5: Schematic of the four unique paths a photon pair can take through the Michelson interferometer.

The parameters derived from the fit are $A = 665 \pm 5$ cps, $B = 186 \pm 7$ cps, $C = 219 \pm 7$ cps, and $\omega = 4.13 \pm 0.02$ rad/fs. The visibility of the signal, which is defined as $\frac{[\max(R_{cc}(\tau)) - \min(R_c c(\tau))]}{\max(R_{cc}(\tau))}$, is given in terms of the fit parameters as:

$$V = \frac{\sqrt{B^2 + C^2}}{A}. \tag{C.25}$$

The uncertainty of the visibility was given by uncertainty propagation of the standard errors of each of the fit parameters. Reporting the visibility through the fit gives a more conservative estimate of the visibility compared to the raw data.

References

[1] M. Fiorentino, S. M. Spillane, R. G. Beausoleil, T. D. Roberts, P. Battle, M. W. Munro, *Optics Express* **2007**, *15*, 7479.

[2] I. Shoji, T. Kondo, A. Kitamoto, M. Shirane, R. Ito, *Journal of the Optical Society of America B* **1997**, *14*, 2268.

[3] M. Jankowski, C. Langrock, B. Desiatov, A. Marandi, C. Wang, M. Zhang, C. R. Phillips, M. Lončar, M. M. Fejer, *Optica* **2020**, *7*, 40.

[4] Y. Hu, M. Yu, B. Buscaino, N. Sinclair, D. Zhu, R. Cheng, A. Shams-Ansari, L. Shao, M. Zhang, J. M. Kahn, M. Lončar, *Nature Photonics* **2022**, *16*, 679–685.

[5] L. Components, Single Photon Counting Module COUNT-Series Datasheet.

[6] S. Tanzilli, H. De Riedmatten, W. Tittel, H. Zbinden, P. Baldi, M. De Micheli, D. Ostrowsky, N. Gisin, *Electronics Letters* **2001**, *37*, 26.

[7] D. Lopez-Mago, L. Novotny, *Physical Review A* **2012**, *86*, 023820.

Appendix D

SUPPLEMENTARY INFORMATION FOR ON-CHIP SAMPLE INTERACTIONS FOR EVANESCENT WAVE SENSING

D.1 Electric field simulations

All simulations were performed in Lumerical MODE. The confinement factor provides a measure of the modal confinement in the PMMA/C153 sample layer and can be expressed as [1]:

$$\Gamma = \frac{n_g}{\mathrm{Re}\{n_{clad}\}} \frac{\iint_{clad} \varepsilon |\mathbf{E}|^2 \, dx \, dy}{\iint_{-\infty}^{+\infty} \varepsilon . |\mathbf{E}|^2 \, dx \, dy}. \tag{D.1}$$

The confinement factor varies with the waveguide geometry, particularly the thin film thickness (Figure D.1a).

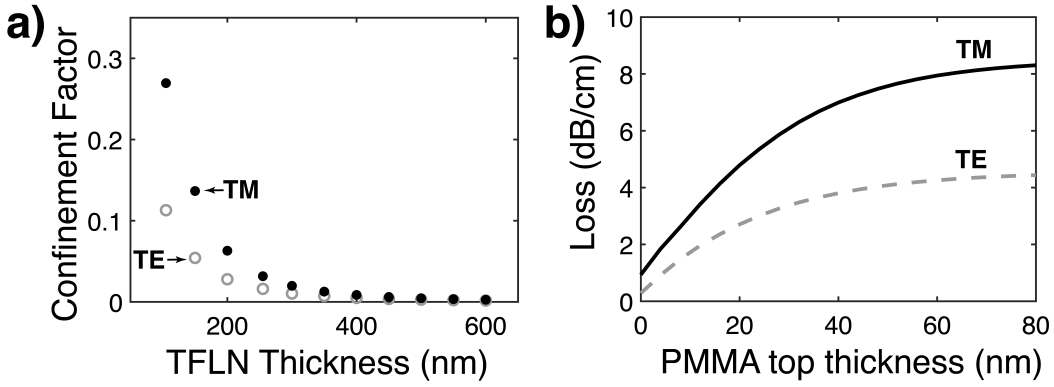

Figure D.1: Simulated mode confinement and loss of the fundamental modes. a) Confinement factor Γ with varying TFLN thickness for a fixed waveguide aspect ratio and conformal 60 nm PMMA/C153 layer. b) Theoretically predicted loss of the TE and TM modes with varying PMMA thickness with the waveguide profile in Figure 5.3b.

To simulate the absorption of Coumarin-153, the dye loss can be incorporated into the simulated material parameters, where the refractive index of the PMMA/C153 is represented as $n' = n + i\kappa$. The real component of the refractive index is the index of bulk PMMA at the excitation wavelength, or $n = 1.5$. The imaginary index κ incorporates the properties and concentration of Coumarin-153:

$$\kappa = \frac{\alpha \lambda_0}{4\pi} = 2.303 \frac{\varepsilon c \lambda_0}{4\pi} = 0.000743 \tag{D.2}$$

where the cross section ε is 20,000 $cm^{-1}M^{-1}$ for Coumarin-153 in toluene, the predicted dye concentration c is 5 mM based on the solution concentrations, the excitation wavelength λ_0 is 406 nm, and the factor of 2.303 comes from the change of base. Incorporating the dye loss κ in the simulation material parameters, the theoretical propagation loss due to the presence of the dye molecules is 4.4 dB/cm for the TE mode and 7.2 dB/cm for the TM mode with a 60 nm conformal PMMA/C153 film thickness. As discussed in Chapter 5, these predicted losses do not match with the experimentally measured losses of 0.67 dB/cm for TE and 0.95 dB/cm for TM. The discrepancy in the predicted and measured losses likely arises from the unknown PMMA/C153 film quality, particularly the film profile near the waveguides. Consistent with this uncertainty, confocal fluorescence microscopy indicates that the PMMA/C153 layer is not uniform over the waveguide profile (Appendix D.3), particularly the top surface of the waveguides. Varying the PMMA/C153 thickness on top of the waveguides but maintaining 60 nm thickness elsewhere (Figure D.1b), the predicted losses decrease to 1.1 dB/cm for TE and 1.6 dB/cm for TM, much closer to the measured values. The losses can be further decreased by incorporating a lower C153 quantum yield, which could be the case due to the PMMA microstructure around the dye, quenching of the dye (such as self-quenching by homo-Förster resonance energy transfer), or degradation of the dye. Decreasing the quantum yield to 50% produces theoretical losses of 0.80 dB/cm for TM and 0.55 dB/cm for TE, much closer to the experimentally measured losses of 0.95 dB/cm for TM and 0.67 dB/cm for TE. The remainder of the discrepancy can be attributed to uncertainties in the dye cross section, uncertainties in the dye concentration, and potential dye aggregation.

D.2 Dye properties

UV-vis absorption spectra were recorded with a Varian Cary 500 spectrophotometer (Agilent). Fluorescence emission spectra were recorded with an RF-6000 fluorimeter (Shimadzu). Spectra were acquired with a 10 μM stock solution of C153 in dimethyl sulfoxide (DMSO), and are shown in Figure D.2.

To estimate the percentage of the fluorescence that is able to transmit through the 500 nm longpass filter $T_{\text{fluorescence}}$, the following integrals over the emission intensity $I(\lambda)$ are numerically evaluated. The limits to these integrals are determined by the wavelength range of the instrument and the filter cutoff.

$$T_{\text{fluorescence}} = \frac{\int_{500\text{ nm}}^{928\text{ nm}} I(\lambda)d\lambda}{\int_{405\text{ nm}}^{928\text{ nm}} I(\lambda)d\lambda} = 0.90 \tag{D.3}$$

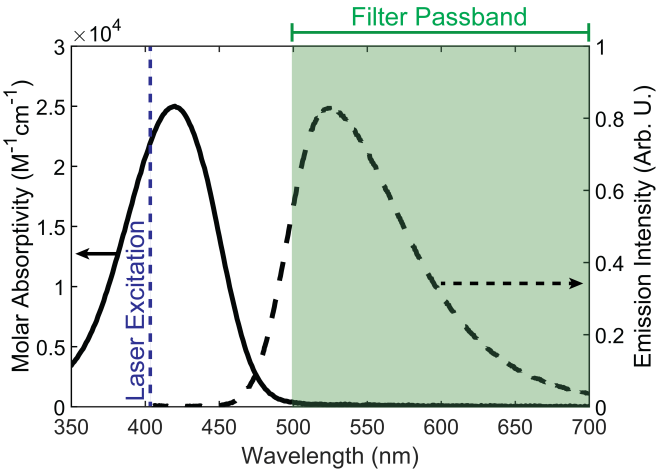

Figure D.2: Absorption and emission spectra of Coumarin-153 in DMSO with the laser excitation and filter passband wavelengths marked.

D.3 Fluorescence microscopy

Fluorescence images of the device were recorded with a scanning confocal microscope (Zeiss LSM 880). The sample was excited with a 405 nm laser diode in an epifluorescence scheme with a 20× dry objective. An image of the PMMA/C153 cladded device is shown in Figure D.3a. The top-most straight waveguide is of the same dimensions as the waveguide investigated in Chapter 5, though it is not the same waveguide due to concerns about photobleaching. A lineout of the intensity collected across the waveguide is shown in Figure D.3b. Each data point is the mean count value at each vertical pixel acquired by integrating the image in the horizontal direction, and the error bars represent one standard error of the mean, calculated from the variance in the counts at each vertical pixel. From Figure D.3b, it appears that the thickness of the PMMA film is not constant across the waveguide profile due to the strong variance in fluorescence as a function of position. Notably, the fluorescence is strongest near the etched areas of the waveguide, and lowest at the top surface of the waveguide. While the fluorescence profile could be explained by variations in the PMMA/C153 thickness, it could also be the result of differences in excitation and collection efficiencies from thin-film interference effects. We therefore suggest that the PMMA thickness might be spatially varying, but do not attempt to make any quantitative claims.

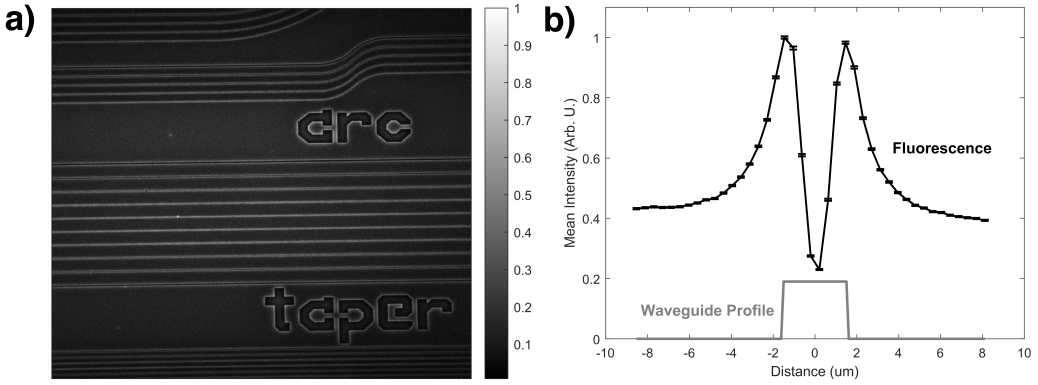

Figure D.3: Imaging of the TFLN waveguide and PMMA/C153 film. a) Fluorescence microscope image of the PMMA/C153 film on the waveguides. b) Lineout of the fluorescence intensity across a waveguide.

D.4 Raw data figures with error bars

The raw data from the imaging experiments in Section 5.3 are displayed in Figure D.4. Uncertainties are given as one standard error of the mean. The uncertainties from each figure are directly comparable as each experiment has the same total integration time of 5 minutes, and all images are acquired with the same digitizer gain (30 dB). The fluorescence datasets are acquired at 1 FPS with an integration time of 1 s, while the scatter datasets are acquired at 10 FPS with a 100 ms integration time to avoid saturating the camera. The uncertainty of the fluorescence data is larger than the scatter data due to the low light intensity, and is especially apparent at the end of the waveguide where the pump is most attenuated.

As discussed in Chapter 5, the propagation loss measured from the fluorescence and the scatter shows good agreement for the TE mode (23.0 ± 0.2 dB/cm and 23.4 ± 0.9 dB/cm, respectively) but show some disagreement for the TM mode (32.5 ± 0.3 dB/cm and 37 ± 1 dB/cm, respectively), most likely due to the higher sensitivity of the TM mode to sidewall scattering and PMMA film variations. Potential reasons for the disagreement in the loss measurements of the TM mode are underestimations in the fit error or the presence of higher-order modes in the waveguide. The spatial variance in the scattering data of Figure D.4 and Figure 5.3 is larger than that of the fluorescence data, most likely due to uneven distribution of scattering sites or speckle interference from the narrow laser bandwidth.

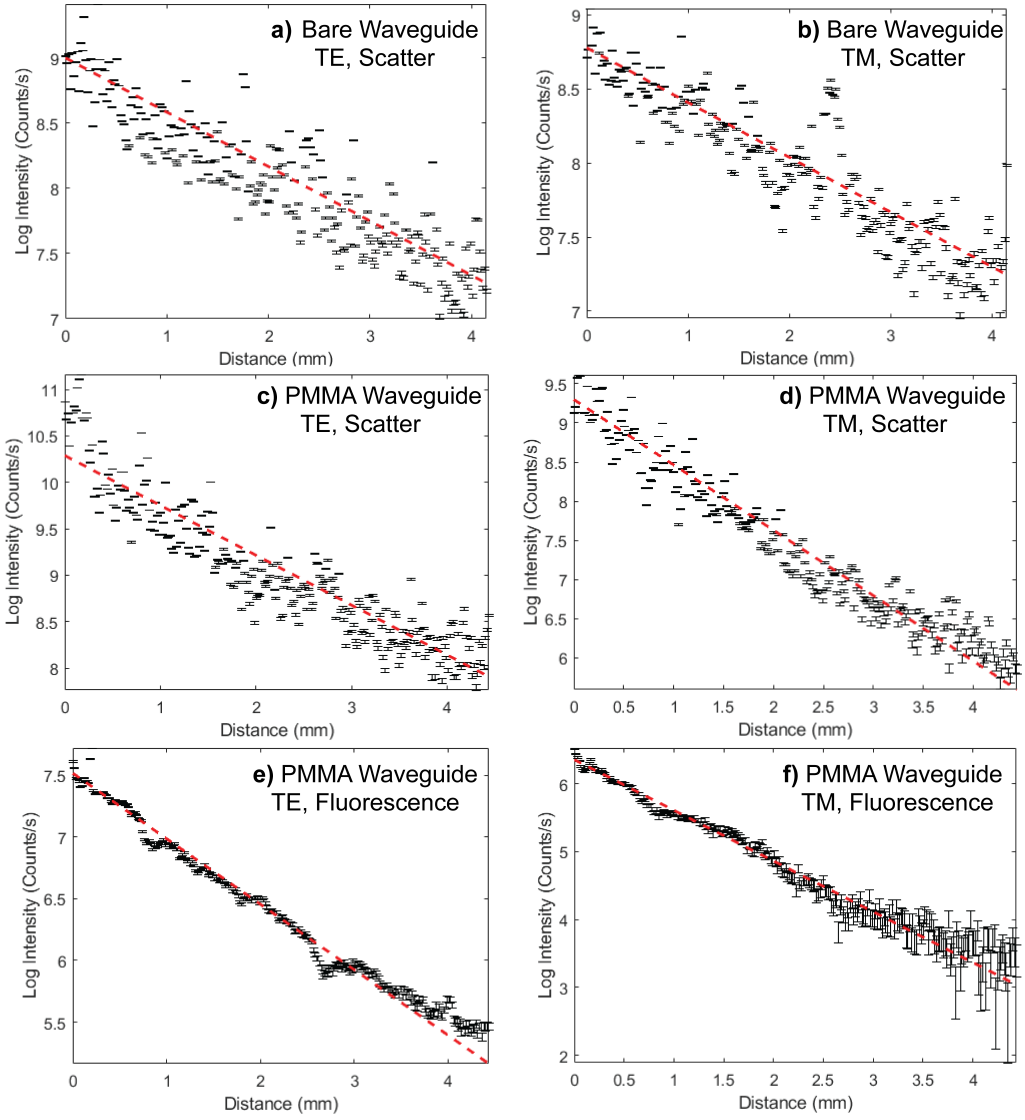

Figure D.4: Raw intensities for a-b) pump scatter from the bare waveguide, c-d) pump scatter from the waveguide with PMMA cladding, and e-f) fluorescence from the waveguide with PMMA cladding. Each data point represents a 17 µm section of waveguide. The red dashed line is a linear fit to the logarithmic data.

D.5 Photobleaching analysis

The incident free space power into a waveguide was increased to determine the appropriate measurement settings with minimal photobleaching. Note that a different waveguide with identical dimensions to the one presented in Chapter 5 was tested here to avoid photobleaching the dye in the main device of interest. After coupling to the TM mode of the waveguide using 5 nW of incident power, the laser was set to the desired power, and fluorescence data were recorded for 100 s, followed by a 100 s background with the laser blocked. This process was repeated a total of five times, with the power level increasing by a factor of 10 for each measurement. A time series of the total amount of fluorescence collected over a 4 mm section of the waveguide are displayed in Figure D.5. While it is difficult to determine if any photobleaching occurs at 10 nW or 100 nW due to the signal-to-noise of the measurement, photobleaching is apparent at 1 µW, and increases in strength at 10 µW and 100 µW. A power of 100 nW was chosen for the experiments in this work to maximize signal while keeping photobleaching to a relatively low level.

D.6 Raw data of aggregate counts

The total count rate over the entire device is summarized in Table D.1. Uncertainties are given as standard errors of the mean. These total counts are proportional to the amount of pump power in the region of interest (ROI), in addition to the scattering and fluorescence loss rates. Since the pump power in the ROI is dependent on the chip coupling efficiency and any losses in the edge beam region of the device, these numbers cannot be directly compared to each other.

Experiment	Total Count Rate in ROI (kcps)
Bare Waveguide, TE, Scatter	799.8 ± 0.3
Bare Waveguide, TM, Scatter	890.5 ± 0.3
PMMA/C153, TE, Scatter	3091 ± 1
PMMA/C153, TM, Scatter	735.9 ± 0.3
PMMA/C153, TE, Fluorescence	185.3 ± 0.1
PMMA/C153, TM, Fluorescence	43.7 ± 0.1

Table D.1: Summary of the total signal recorded for each experiment, integrated over a 4.3 mm section of the waveguide.

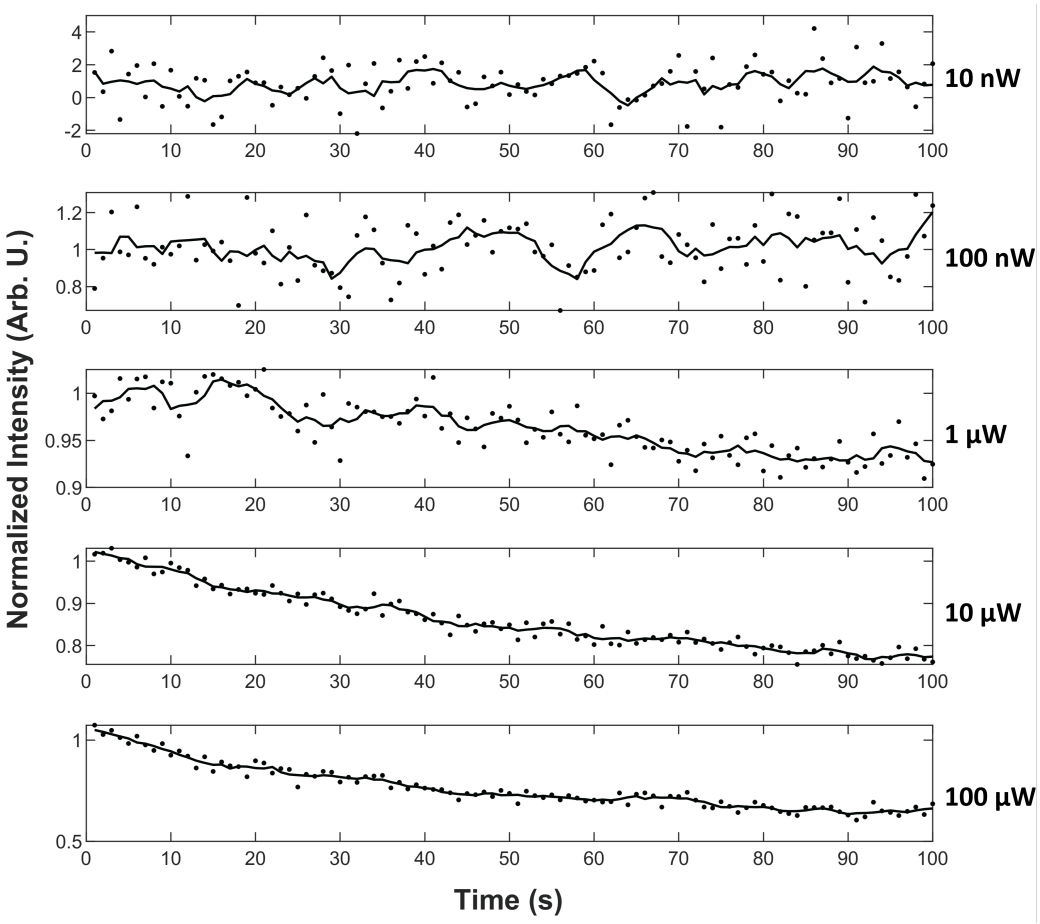

Figure D.5: Integrated fluorescence intensity over time for increasing values of free-space power. Data points show the raw intensity at each time point, and lines are a 5 s moving average. Intensities have been normalized relative to the mean intensity of the first 10 data points.

References

[1] M. Vlk, A. Datta, S. Alberti, H. D. Yallew, V. Mittal, G. S. Murugan, J. Jágerská, *Light: Science & Applications* **2021**, *10*, 26.

Appendix E

SUPPLEMENTARY INFORMATION FOR CASCADED SPONTANEOUS PARAMETRIC DOWNCONVERSION ON THIN-FILM LITHIUM NIOBATE

The spectrum from the dispersion engineered waveguide geometry compared to the spectrum from the non-dispersion engineered waveguide geometry is shown in Figure E.1. Both spectra were measured using the setup shown in Figure 6.5b. The brightness axis was calibrated in the same manner as described in Section 6.3, using the average brightness in a 30 nm bandwidth centered at 1556 nm to scale the spectra measured with the OSA.

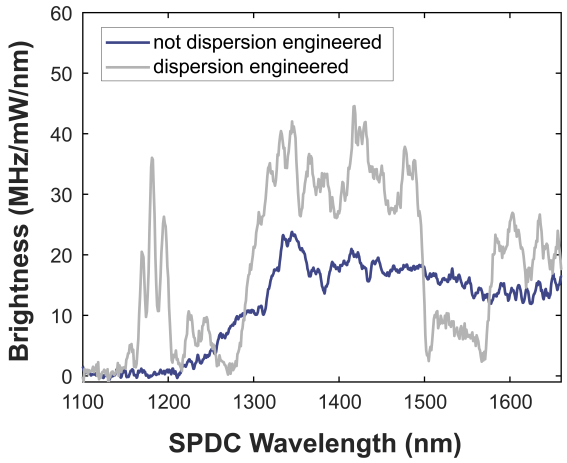

Figure E.1: Comparison of spectra from the dispersion engineered and non-dispersion engineered waveguide geometries. Brightnesses were calibrated using the measured efficiencies and brightnesses with a 30 nm band-pass filter centered at 1556 nm.

As shown in Figure E.1, the spectrum of the dispersion engineered waveguides has a dip around 1500 to 1600 nm, resulting in the overall lower brightness of the dispersion engineered waveguides (5.8×10^6 pairs/s/mW) compared to the non-dispersion engineered waveguides (1.5×10^7 pairs/s/mW) with the band-pass filter. Future work will be done to explore the source of this dip in the spectrum, which could potentially be due to absorption or poling defects. Due to the IR SPAD efficiencies, which are only reported at 1550 nm, and the low likelihood of detecting a threefold coincidence count for the entangled photon triplets, the brightness and

loss of the source at 1550 nm were prioritized. Thus, due to the lowered 1550 nm brightness and increased loss of the dispersion engineered waveguides, the non-dispersion engineered waveguides were chosen for further triplet measurements over the dispersion engineered waveguides.

Despite the lowered brightness of the dispersion engineered waveguides around 1550 nm, the peak brightnesses of the dispersion engineered waveguides is noticeably higher than that of the non-dispersion engineered waveguides in Figure E.1. The dispersion engineered waveguides have a peak brightness of 45 MHz/mW/nm, which is almost double the peak brightness of the non-dispersion engineered waveguides of 24 MHz/mW/nm. This overall increased peak brightness demonstrates the potential of the dispersion engineered waveguides if further work is done to address the increased losses from the small top widths and the decreased brightness at 1550 nm.